MECHATRONIC DESIGN AND OPTIMISATION OF A LOW-COST PROSTHETIC HAND

by

Gregory Kyle Jones

Dissertation presented in partial fulfillment of the requirements for the degree of Master of Science in Bio-Mechatronic Engineering at the University of KwaZulu-Natal
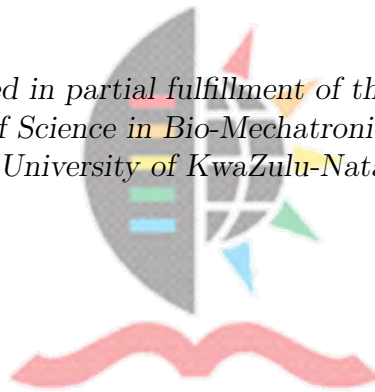
Discipline of Mechanical Engineering,
Mechatronics and Robotics Research Group (MR2G),
Bio-Engineering Unit,
University of KwaZulu-Natal,
Science Drive, Durban, 4001, South Africa.

Supervisor: Dr. R. Stopforth

July 2015

COLLEGE OF AGRICULTURE, ENGINEERING AND SCIENCE

DECLARATION 1 - PLAGIARISM

I, Gregory Kyle Jones, declare that

1. The research reported in this dissertation, except where otherwise indicated, is my original research.

2. This dissertation has not been submitted for any degree or examination at any other university.

3. This dissertation does not contain other persons' data, pictures, graphs or other information, unless specifically acknowledged as being sourced from other persons.

4. This dissertation does not contain other persons' writing, unless specifically acknowledged as being sourced from other researchers. Where other written sources have been quoted, then:

    a Their words have been re-written but the general information attributed to them has been referenced

    b Where their exact words have been used, then their writing has been placed in italics and inside quotation marks, and referenced.

5. This dissertation does not contain text, graphics or tables copied and pasted from the Internet, unless specifically acknowledged, and the source being detailed in the dissertation and in the References sections.

Signature: ....

Supervisor's Agreement

As the candidate's Supervisor I agree/do not agree to the submission of this dissertation.

Signature: ....

COLLEGE OF AGRICULTURE, ENGINEERING AND SCIENCE

DECLARATION 2 - PUBLICATIONS

DETAILS OF CONTRIBUTION TO PUBLICATIONS that form part and/or include research presented in this dissertation:

- Jones, G. K., Stopforth, R., "Improvements on a Prosthetic Hand: The UKZN Touch Hand"

    ○ Jones, G. K. (1st author)

    ○ Stopforth, R. (supervisor)

Signature: ....

ACKNOWLEDGEMENTS

ABSTRACT

The Touch Hand II was developed to improve on the first version, addressing the lack of low cost myoelectric controlled hand prostheses. The improvements included a lower materials cost of \$ 635.14, an aesthetically appealing human–like form factor, a reduced total mass of 486 g (including the wrist and electronics), a 211 % increase in grip strength, and a 3.83 times higher allowable palm load with a 1.7 factor of safety. Costs were reduced predominantly due to 3D printing and using sensorless technology, based on speed and torque estimation through brushed dc motor back-emf and current measurements. The compact design was accomplished by using a unique finger actuation and trajectory concept, and integrating a custom PCB. An intuitive command selection protocol was developed with the aid of a GUI. A finite state machine was used to successfully switch between speed and grip force control depending on whether an object was in contact with the fingers during a close/open command. The design has accommodated the future addition of myoelectric control, sensors, and sensory feedback.

DEDICATIONS

I dedicate this dissertation to my mother, Amanda Louise Jones, late father, Sean Gregory Jones, and brothers, Lee Kelby Jones and Dean Jones. Also to Hillary Gaertner who supported me through my work to make it possible.

CONTENTS

LIST OF FIGURES

LIST OF TABLES

NOMENCLATURE

Constants

$g = 9.81$	Gravitational Acceleration	$[\,\mathrm{m/s^2}\,]$
$\pi = 3.14$	Pi	$[\,\mathrm{rad}\,]$
K	Motor Flux Constant	$[\,\mathrm{N.m/A.Wb}\,]$
ϕ	Motor Magnetic Flux	$[\,\mathrm{Wb}\,]$

Variables

a	Link Length	$[\,\mathrm{m}\,]$
d	Diameter or Joint Distance	$[\,\mathrm{m}\,]$
e	Control Error	$[\,\mathrm{N.mm, rpm}\,]$
f	Frequency	$[\,\mathrm{Hz}\,]$
i	Transient Current	$[\,\mathrm{N}\,]$
k	Control Constant	$[\,\mathrm{V/N.mm, V/rpm}\,]$
l	Length	$[\,\mathrm{m}\,]$
m	Mass	$[\,\mathrm{kg}\,]$
n	Number of Joints	$[\,-\,]$
r	Control Reference/Setpoint	$[\,\mathrm{N.mm, rpm}\,]$
t	Time	$[\,\mathrm{s}\,]$
u	Control Variable	$[\,\mathrm{V}\,]$
v	Transient Voltage	$[\,\mathrm{V}\,]$
x	Coordinate Axis	$[\,\mathrm{m}\,]$
y	Coordinate Context: Axis	$[\,\mathrm{m}\,]$
y	Control Context: Process Variable	$[\,\mathrm{N.mm, rpm, V, A}\,]$
z	Coordinate Axis	$[\,\mathrm{m}\,]$
A	Coordinate Transformation Matrix	$[\,\mathrm{A}\,]$
C	Material Cost	$[\,\$\,]$
D	PWM Duty Cycle	$[\,\%\,]$
E	Steady State Back-Emf Voltage	$[\,\mathrm{V}\,]$

F	Force	$[\,\mathrm{N}\,]$
G	Gear Ratio	$[\,-\,]$
I	Steady State Current	$[\,\mathrm{A}\,]$
L	Inductance	$[\,\mathrm{H}\,]$
M	Mass	$[\,\mathrm{kg}\,]$
P	Power	$[\,\mathrm{W}\,]$
R	Resistance	$[\,\Omega\,]$
S	Safety Factor	$[\,-\,]$
T	Torque	$[\,\mathrm{N.m}\,]$
V	Voltage or Steady State Voltage	$[\,\mathrm{V}\,]$
W	Weight Load	$[\,\mathrm{kg}\,]$
α	Link Twist	$[\,\mathrm{rad}\,]$
β	Control Integral Error	$[\,\mathrm{N.mm, rpm}\,]$
η	Efficiency	$[\,\%\,]$
θ	Rotation or Joint Angle	$[\,\mathrm{rad}\,]$
ω	Rotational Speed	$[\,\mathrm{rad/s}\,]$

Subscripts

avg	Effective average PWM
c	Motor Current
e	Electrical
emf	Electromagnetic-Force
emf_offset	Electromagnetic-Force Offset
end	End Region
g	Gearhead/Gearbox
g_in_max	Gearbox Maximum Input
$g\_in\_max\_cont$	Gearbox Maximum Continuous Input
$g\_in\_max\_int$	Gearbox Maximum Intermittent Input
g_out_max	Gearbox Maximum Output
$g\_out\_max\_cont$	Gearbox Maximum Continuous Output
$g\_out\_max\_cont\_1$	Gearbox Maximum Continuous Output for Load Case 1
$g\_out\_max\_int$	Gearbox Maximum Intermittent Output
$g\_out\_max\_int\_1$	Gearbox Maximum Intermittent Output for Load Case 1
$g\_out\_max\_1$	Gearbox Maximum Output for Load Case 1
$g\_out\_max\_2$	Gearbox Maximum Output for Load Case 2

g_select	Selected Gearhead Option
h	Hand Hook Grasp
h_cont	Hand Hook Grasp Continuous Load
h_f_cont	Finger Continuous Load in Hook Grasp
h_f_int	Finger Intermittent Load in Hook Grasp
h_int	Hand Hook Grasp Intermittent Load
i	Link Number
it	Integral Torque
iv	Integral Speed
$loss\_comb$	Combinational Losses
$loss\_elect$	Electrical Losses
$loss\_mech$	Mechanical Losses
m	Motor
mid	Middle Region
m_cont	Motor Continuous
m_int	Motor Intermittent
m_load	Motor Load
m_max	Motor Maximum
m_nom	Motor Nominal
m_o	Motor No-Load
m_out	Mechanical Output
m_stall	Motor Stall
o	No-Load
p	Pulley
$peak$	PWM Peak
pt	Proportional Torque
pv	Proportional Speed
pw	PWM Pulse Width
p_s_mid	Midway of Small Proximal Phalangeal
s	Start Region
$supply\_nom$	Nominal Supply
t	Time Context: Maximum Finger Closing Cycle
t	Control Context: Torque
v	Speed
H	Hand

L	Load
MCP	Metacarpal-Phalangeal Joint
MCP_max	Metacarpal-Phalangeal Joint Maximum
PWM	Pulse–Width–Modulation
0	Base Frame Axis

Supercripts

i	Inner
n	Control Sample Number
o	Outer
R	Rated Value

1   INTRODUCTION & LITERATURE REVIEW

The human hand is an integration of complex systems of tendons, nerves, muscles, and bones. Losing a hand limits the ability of a person to explore and communicate in their surroundings. An amputee has a reduced dexterity, having difficulties with manipulating and sensing objects. Physical differences from others can lead to psychological issues (Micera *et al.*, 2010). Estimates for persons living in the United States have been made, where more than 900,000 people have minor limb loss, and 664,000 people have major limb loss. "Minor" limb loss includes amputation of digits (toes or fingers) or the hand, and is most common. "Major" limb loss includes amputation below the elbow (transradial), below the knee, above the elbow (transhumeral), above the knee, or the foot (Kurichi *et al.*, 2010).

Prosthetics are used in an attempt to restore the previous function and aesthetics of a lost limb. The first known prosthetics were found to date back to approximately 1500 B.C, where the Egyptians produced them from fibre. These are believed to have been worn more for visual appeal rather than functionality. It was not until after World War II when major advancements began in prosthetic technology (Norton, 2007). Currently, commercial prosthetic hands have the ability of moving individual fingers to grasp differently shaped objects, and are predominantly controlled using myoelectric signals (MES) detected during muscle contraction (Micera *et al.*, 2010). These hands can cost in the $ (US) 30, 000 to $ (US) 50, 000 range (van der Riet, 2014), creating financial barriers to amputees interested in using these hands.

The primary focus of this research is to contribute to low-cost and simplified mechanical and electronic design alternatives in hand prosthetics, by designing a hand that is aesthetically pleasing, functional, upgradeable and cost effective. The focal point of this introductory chapter is outlining the scope of the achievements made in the commercial and research sectors related to prosthetic hands, followed by the problems and improvements of the first prosthetic hand developed at UKZN, the Touch Hand I.

The research covered in this document is laid out into seven chapters. Following the introductory chapter, the mechanics, electronics, and control design are dealt with as separated topics. All the testing is compiled together before discussing the results, how the objectives were satisfied, problems, and future work.

1.1   COMMERCIAL PROSTHETIC HAND TECHNOLOGY

The most competitive commercial prosthetic hands include the i-limb Ultra Revolution by Touch Bionics, the Michelangelo by Ottobock, and the Bebionic3 by RSLSteeper (Ottobock, 2014). Each of these prostheses have similar but also different features to one another. These three hands have been designed for transradial amputees (amputated between the elbow and wrist). An image of the Bebionic3 prosthetic hand can be seen in Figure 1.1 (RSLSteeper, 2013*a*).

Figure 1.1: Bebionic3

These prosthetic hands have been designed with a number of features. Motors are commonly used to give individual finger position control, however passive movement is also used, such as with the Michelangelo. The thumb, index and middle finger are actively driven, while the ring and little finger passively follow the others (Ottobock, 2014). The thumb of the Bebionic 3 is not completely electronically controlled, but is rather moved into different positions manually (RSLSteeper, 2013*b*).

All designs have a number of grip types. The Michelangelo gives a set choice of pre-defined grip patterns (Ottobock, 2014). In the case of the Bebionic 3, grip patterns can be customised in mobile and computer compatible software. User training is also done via the provided software packages. Wireless connections between the prostheses and user software is made possible either through bluetooth or radio signals (Touch Bionics, 2013*c*). Other grip modes have also been integrated into these devices. The i-limb Ultra Revolution has a "compliant grip" that lets the fingers of the hand move until they are holding an object (Touch Bionics, 2013*c*). The "Auto-grasp" gives the hand the ability to detect false open signals whereby it automatically tightens to stop held objects from falling (Touch Bionics, 2013*a*).

Wrist modules have also been designed, with some being optional and others already integrated. The two wrist attachments for the i-limb Ultra Revolution are: the Flex Wrist, and the Multi-flex Wrist (Touch Bionics, 2013*c*). The former option allows three manually

selected wrist positions, which are locked in place, making an improvement on the natural feel and comfort (Touch Bionics, 2013*a*). The latter option enables load compensation by using a passive spring-loaded design, and can be adjusted within a 60° range (Touch Bionics, 2013*c*). The Michelangelo has its wrist design already integrated into the hand, with similar capabilities (Ottobock, 2014).

In terms of control, two myoelectric signal (MES) channels are commonly used for communication between the users muscles and the prosthesis (RSLSteeper, 2013*b*). MESs are detected using surface mounted electrodes in these devices (RSLSteeper, 2013*b*). A drawback of these commercial prostheses is that none of them give sensory feedback, depriving the user of any idea on grip force, position, or other senses commonly felt by an unimpaired human-being.

The mechanical design of these prostheses accommodate easy replacement of fingers. The i-limb Ultra Revolution can use four different finger sizes. These sizes are split into two strength categories, small and medium, with the latter category using a larger motor. The palm section of the hand also comes in two different sizes (Touch Bionics, 2013*b*). Aesthetic and grip improvements are achieved using various cosmetic gloves that fit over the prostheses.

An overall comparison of the main features in these devices can be found in Table 1.1. The best value for each feature is highlighted in bold.

1.2 RECENT PROSTHETIC TECHNOLOGY

There have been recent advances in research and development technology for prosthetics. To give a brief insight into these advances, two projects, namely the Deka Arm System and the LifeHand2, are highlighted.

The DEKA Arm System or 'Luke Arm' has been in development for the past eight years, and has officially been approved for commercialisation by the Food and Drug Administration (FDA). The advanced arm uses non-invasive control techniques, and provides haptic feedback to the user by transmitting signals to a tactor (vibrating motor). Control by the amputee is via surface electromyogram (sEMG) signals (Guizzo, 2014). These signals are measured by electrodes attached to the surface of the skin, which are then processed by a micro-controller-unit (MCU). The MCU then sends appropriate signals to the motors of the fingers for them to move. Pressure sensors integrated into the hand, measure grasping forces, which is used to feedback force signals to the user through the tactor. Different vibrations of the tactor correspond to different grasping forces, giving the user force control (Adee, 2008). This arm is unique by using additional inputs switches on the users feet to perform complex tasks (Guizzo, 2014).

The second aforementioned project, LifeHand 2, aims to develop an implantable prosthesis system via the users nervous system. An amputee recently allowed researchers to connect electrodes to his peripheral nervous system, within his arm - an invasive method of retrieving myoelectric signals. He was able to control the gripping force of a prosthetic hand,

Table 1.1: Comparison of Commercial Prostheses

Feature	i-limb Ultra Revolution (Touch Bionics, 2013a)	Michelangelo (Ottobock, 2014)	Bebionic3 (RSLSteeper, 2013b)
Power Grip Srength[1] (N)	136	70	**140.1**
Lateral (Lateral Pinch) Grip Strength[2] (N)	35	**60**	26.5
Hook (Medium Wrap) Grip Load[3] (kg)	**90**	n/a	45
Finger Hook Load[4] (kg)	**32**	n/a	25
Closing Time (s) - Power Grip	1.2	n/a	**1.0**
Grip Patterns	**24**	7	14
Control	2 MES channels	2 MES channels	2 MES channels
Weight with Wrist (g)	**515**	600	698

1. Thumb opposing other four fingers, closing into the palm; 2. Thumb closes onto the side of the index finger; 3. Partially closed power grip position; 4. Partially closed individual finger.

distinguish different object shapes, and even their stiffness. The experiments were performed while the amputee wore a blindfold and earphones to block out additional senses (Laursen, 2014). The amputee can be seen in Figure 1.2 (Tocci, 2014) performing one of the tests.

1.3 IMPROVEMENTS ON COMMERCIAL TECHNOLOGY

There are a number of characteristics of commercial prosthetics that are lacking, or do not even exist. These, as well as possibilities in prosthetic research, are discussed in order to understand some of the gaps in the technology.

1.3.1 Cost

The high costs of commercial prostheses, usually in the range $ (US) 30,000 to $ (US) 50,000 (van der Riet, 2014), restrict the technology to those who can afford it. Minimizing the

Figure 1.2: Life Hand 2 Amputee Testing

cost of a prosthetic hand would generate more opportunities for amputees with financial restrictions. Considering low-cost manufacturing methods, materials, and components will aid cost reduction. Designs which require less medical and technical assistance would reduce rehabilitation and maintenance costs, respectively.

1.3.2   Sensory Feedback

Without sensory feedback, most commercial prostheses cause their users more difficulties in detecting the state of their prosthesis in the environment, forcing them to use a significant amount of mental effort (Jiang *et al.*, 2012). Haptic feedback is a non-invasive approach (van der Riet, 2014), which uses the sense of touch. Pressure, vibration, and neuromuscular electrical stimulation (NMES) are possible methods that can be used in this approach. Targeted sensory reinnervation (TSR) is an invasive approach that uses sensory receptors within the skin to transmit sensory information to the brain (Jiang *et al.*, 2012). Invasive methods require the user to approve of a medical procedure.

1.3.3   Control

Simple myoelectric controller algorithms were developed approximately 50 years ago that used an electromygram (EMG) amplitude threshold value. The same technology is still used in advanced commercial prosthetic hands to date. The technique limits the number of hand functions, but can be selected in minimal time (Jiang *et al.*, 2012). The characteristics of these EMG signals can change due to prolonged usage; normally due to fatigue, movement of electrodes, and sweat (Jiang *et al.*, 2012). This contributes to the difficulties in creating a very adaptable and robust control system using only EMG signals. Highly developed EMG pattern classification methods have not found practical implementations in commercial prosthetics, due to their unnatural control scheme. A natural control strategy that could adapt to EMG signal changes would be more valuable.

Another observation made by the author, is that commercial prostheses do not integrate adaptable grip force control with the aid of slip detection. The basic principal operation is that when slip is detected, the grip force is predicted and increased to stop the object from falling (Pasluosta *et al.*, 2009).

A design using a rich multi-modal input could motivate the development of autonomous controllers (Jiang *et al.*, 2012). An example would be using movement and orientation measurements of the prosthesis, and other parts of the body, to complement the EMG signals in predicting the desired hand configuration.

1.3.4 Modularity

As previously mentioned, the i-limb Ultra Revolution was designed to have the fingers easily removed and replaced. There is also the option of attaching two types of wrists. To the authors knowledge, there are no designs that can progressively change from pure mechanical actuation to electronic actuation. Alternatively, changing the number of active and passively controlled digits could be modulated. This would give an amputee, with a budget restriction, an opportunity to purchase an initial prosthesis with functionality comparable to a purely mechanical prosthesis. Once more funds are available, additional actively controlled digits could be added for improved functionality.

1.4 THE TOUCH HAND I

In the years 2013 and 2014, a prototype prosthetic arm was developed at the University of KwaZulu-Natal. The most prominent result of the research was the composition of the Touch Hand, consisting of three major segments; the hand, wrist, and forearm (van der Riet, 2014).

1.4.1 Objectives

Implementing a new approach to EMG control of a prosthetic hand was a primary goal. This was to be supported by a novel sensory feedback system, with the capability of relaying multi-sensory information to the user. An additional research goal was to establish an inexpensive, modular prosthetic arm that was able to give human-like functionality and performance, which would facilitate the primary goals.

1.4.2 Mechanical Design

Figure 1.3 gives a visual comparison between the CAD and physical model of the final hand. The total number of degrees of freedom (DOF) that exist in the hand are 16. Seven motors were used in the hand, six for the fingers and one for the wrist. Acrylonitrile butadiene styrene (ABS) plastic was used to 3D print all the custom designed components. The total production cost of the hand was less than $ (US) 1000, much less than commercial options.
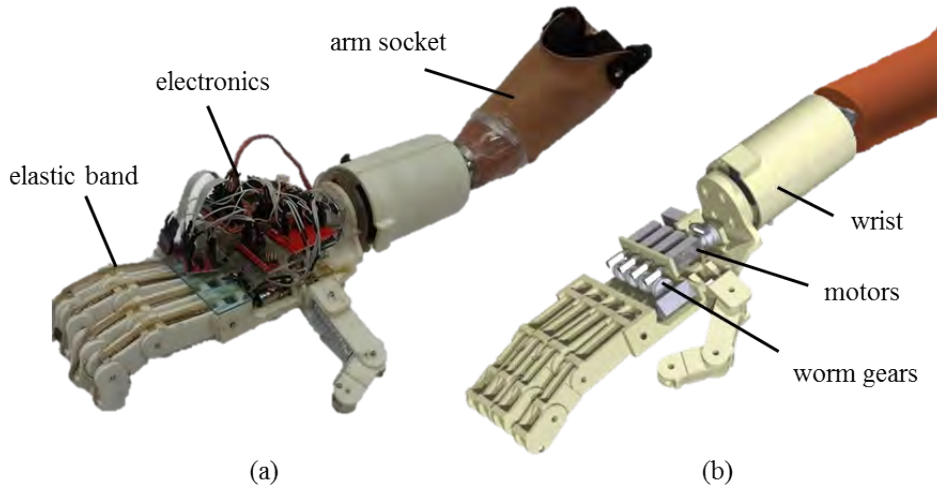
Figure 1.3: Touch Hand I: (a) physical hand, (b) CAD modeled hand

Finger actuation was possible using a separate wire for the index, middle, ring, and small finger, while the thumb used two wires. Each wire was attached to a pulley, driven by a motor through a worm gear. Hence, the motor could wind or un-wind the wire, pulling or releasing the wire. When the wires were un-wound by the motors, elastic bands would pull the fingers back toward full extension. The hand was attached to an amputee through a custom fit socket, and an arm strap.

The finger open/close kinematics were graphically compared to a single human hand example, through spatial joint trajectories and velocities. Analytical errors were not determined, but the results showed approximately a minimum velocity error of 15 %, and the maximum joint trajectories error was approximately 4 cm, or 100 %.

The major mechanical performance measures of the prosthetic hand have some significant discrepancies to human measurements. The power, hook and lateral grip forces of 19.5 N, 8.25 kg and 3.7 N, respectively, are 28 %, 18 % and 14 % of the lowest value of the commercial products previously discussed, respectively. The closing time of the prosthetic hand was measured to be 2 seconds, 25 % off of the measured human hand time.

1.4.3 Electronics

The electronics was broken up into four primary sections: EMG sensors, tactile sensors, Haptic User Interface (HUI) and haptic feedback, and finally the motor actuation and position feedback circuitry. Figure 1.4 represents the flow diagram of electronic communication between these areas.

A Seeeduino Mega development board, based on an Atmega 1280 microcontroller (MCU), was used to integrate all of the sensors, external circuitry, and control software. EMG electrodes were strategically placed on muscles to pick up contractions. Brushed DC motors were used for actuation. Motor positions were controlled with PWM signals, through dual h-bridge breakout boards. Flex sensors, positioned along the length of each
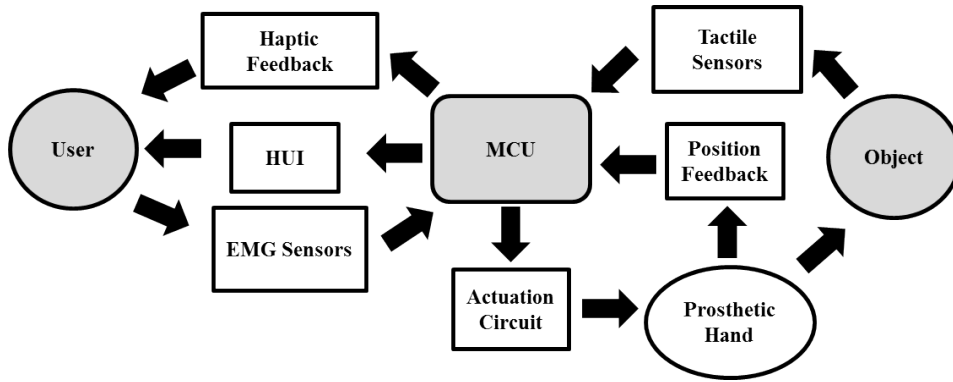
Figure 1.4: Touch Hand I: Electronics Flow Diagram

finger, were used for motor positional feedback.

The user was fed information via haptic (sense of touch) feedback, through a vibrotactile display (array of vibration motors). Force, temperature, and vibration sensors were incorporated in order to measure grip force, object slip, texture, and temperature.

1.4.4 Control

The Haptic User Interface (HUI) was designed to create a communication link between the user and the control of the prosthetic hand. A two channel EMG electrode setup was used, where each channel measured a specific muscle contraction. The user sends information to the MCU through the EMG electrodes, after processing this information, the MCU responds through the vibrotactile array, and moves the hand fingers as necessary.

Different grip patterns are selected through the HUI menu. The user can navigate through a list of grip patterns categorised into different groups: opposed grips, non-opposed grips, gestures, wrist and elbow. Each of these categories then have a number of grip options. The menu initialises in the home position, followed by up and down navigation by the user individually contracting specific muscles. Selecting an option is done by simultaneously contracting two specific muscles.

The hand has 7 different grip types to select from, as well as 12 different hand positions and gestures. More grips could be added to the HUI menu, however this would increase the maximum time to select an option. A maximum time of 5 seconds was measured for selecting a grip type.

Using the vibrotactile array, a feedback investigation was done using information of grip force, slip detection, object texture and temperature. Force and temperature information were easily integrated, however algorithms for slip and texture detection were not implemented. Instead, slip and texture detection data was simulated when performing tests with volunteers. The results showed that increasing the number of sensory feedback channels decreased the ability of the test subjects to discriminate the information.

1.4.5 Problems and Possible Improvements

Following the previous description of the Touch Hand, there are some clear areas of improvement. These include, but are not limited to, aesthetics, grip adaptability, kinematics, grip forces, electronic hardware, motor control, user interface.

1.4.5.1 Aesthetics

It is clear from Figure 1.3 that the final hand does not have a close visual representation of the human hand. There are many corners, edges, flat surfaces, and exposed sections that cause this. It could have a cosmetic glove (a glove that has the aesthetics of the human skin), to give a more realistic appeal. However, the glove could experience tears from the sharp edges.

1.4.5.2 Grip Adaptability

A problem not previously described, is that the fingers are not able to adaptively grasp every type of object shape. An example is shown in Figure 1.5, where the hand is attempting to grasp a round surface. The distal phalangeal (end finger bone) and middle phalangeal (middle finger bone) do not sit flush against the surface. This is due to the wire inducing torques about each joint of the finger.

Figure 1.5: Touch Hand I Gripping a Ball

1.4.5.3 Kinematics & Grip Forces

The kinematic and grip force results, previously described, show a large gap of improvement. More emphasis on improving spatial joint trajectories will yield more realistic finger movements. Reducing the closing time of the hand will have a similar affect. Grip forces

were described as being between 14 % and 28 % of commercial product values. These values should be increased closer to human abilities.

1.4.5.4   Electronics

Improvements on the electronics include the aesthetics and motor control. Looking at the electronics of Figure 1.3, it is obvious that the mess of wires and boards give an unpleasant visual appeal. Compacting the electronics in an enclosed area would result in more realistic hand-like aesthetics. Wireless technology for programming and self-contained batteries for power could assist with this goal. Using flex sensors for motor position control requires a large amount of space in the finger. There are other positional feedback options, such as encoders, that would most likely give a higher positional resolution, whilst using less space. This would support a fast responding, high accuracy control system.

1.4.5.5   Control

In terms of control, there are four subjects of improvement and future work. The first is reducing the maximum grip type selection time. Any human can make hand movement decisions in fractions of a second. The second would be to develop software that would assist with selecting the optimal position of the EMG electrodes on the available muscles. The third is that the strategy of using pulse length to discriminate various sensory intensities, was difficult for test subjects because they did not have a clear reference point. Using an alternative strategy may resolve this. The fourth and final possible improvement is to design and implement control for grip force. This could also include automatic grip force control through slip detection - the grip force on an arbitrarily shaped object would change such that it does not slip out of the grasp.

1.5   RESEARCH OBJECTIVES & CONTRIBUTIONS

This research is aimed at designing and developing a prosthetic hand for transradial amputees, implementing specific improvements on the Touch Hand. The hand shall be named the Touch Hand II. The objectives for this design are extracted from possible improvements on commercial prosthetic hands, the Touch Hand, and considering qualities desired by amputees using prostheses (Kyberd *et al.*, 2007). These objectives should assist with answering the question, "Can further improvements be made on the Touch Hand I to create a low cost alternative to commercially available prosthetic hands?".

Most objectives for the Touch Hand II are listed as improvements on the Touch Hand, and are as follows:

1. improving aesthetics; by creating a compact mechanical hand design with self-contained electronics with a human form-factor.

2. a left and right hand design should be manufacturable with one electronic board design that is interchangeable between the two.

3. the electronics should be able to support future sensory and control upgrades/additions; specifically temperature and vibration sensing, two vibration motors for haptic feedback, and two channel myoelectric control.

4. implementing intuitive grip force, speed, and hand grasp selection control through simulated amputee commands from a computer.

5. improved functional performance; by reducing the hand closing time, increasing the maximum gripping force, decreasing the mass, and increasing the maximum allowable loads.

6. maintaining the materials cost below $ (US) 1000 (R 12 225,25).

1.6   DESIGN SPECIFICATIONS

Specifications were listed as design guidelines and for evaluation purposes. During the design process, further limitations were realised and the specifications altered to accommodate these. The final specifications consist of the maximum mass loads to be held in the hook grip, the closing time from a flat hand to a fist, the mass of the hand including the electronics, and the manufacturing cost. These values are listed in Table 1.2.

Table 1.2: Touch Hand II Design Specification Goals

Variable	Description	Value
M_{h_cont} [kg]	hook grasp continuous mass load	3.4
M_{h_int} [kg]	hook grasp intermittent mass load	4.6
t_t [s]	maximum finger closing cycle time	1.0
m_H [g]	mass of the hand (incl. electronics)	< 500
C	materials cost	< $ (US) 1000 (R 12 225)

These values were selected as improved specifications in comparison to the first version of the hand, shown in Table 1.3. You can see that the first version had a materials cost value the same as the second because it is a major constraint, already at a low amount. The previous hand also did not have an intermittent mass load option because the motors were not designed to be driven with an over rated current.

Table 1.3: Touch Hand I Specifications

Variable	Value
M_{h_cont} [kg]	0.5
M_{h_int} [kg]	n/a
t_t [s]	2.0
m_H [g]	540
materials cost	$(US) 1000

1.7 CHAPTER SUMMARY

Amputations of the hand cause a person to struggle with interacting with their environment. This is because the hand is such a complex part of the body. Prosthetic hands have been around for centuries, however it has only been in the past few decades that electronically controlled commercial prosthetic hands have become available. These are able to form a number of grip patterns, controlling the position of each finger. Recent technological advances have been able to give amputees the ability to have sensations of the prosthesis, such as grip force, object shape, texture, and stiffness. However, in the case of the Life Hand 2 project, invasive methods are required. Improvement areas of commercial hand prostheses include cost, modularity, control, and sensory feedback. The Touch Hand I was developed to attend to some of these issues, although a number of improvements on the Touch Hand I have been identified. A set of design objectives for a new prosthetic hand, the Touch Hand II, were listed, which addressed specific improvements.

2   MECHANICS

Attempting to mechanically replicate the human hand involved a deep understanding of the anatomy, possible solutions to the mechanical design problems, and a detailed design process. Each of these areas were followed through methodically and are described in this chapter.

2.1   THE HUMAN HAND

Attempting to replicate the hand with a functional design for an amputee should start, logically, by understanding what makes up the hand, how it functions, and its limitations. This can be investigated by considering some important topics, such as the anatomy, osteokinematics, and grasp taxonomy of the hand.

2.1.1   Anatomy

It is generally known that the human hand is part of a natural design as a result of many years of evolution. It is, therefore, the ideal design, since this is what hand prostheses are attempting to replace. In order to replicate a hand, the internal structure, mechanisms, and functional capabilities should be well understood.

2.1.1.1   Bones

The human wrist and hand contains a total of 27 bones. These are encompassed by three subcategories, namely, the phalanges, metacarpals, and carpals. The wrist joint is formed by the radius and ulna bones attached to the carpals (eOrthopod, n.d.). A detailed annotated figure of these bones is depicted in Figure 2.1, a modification of (MMG, 2003). The anatomy of four of the digits — index, middle, ring, and small — are basically the same, except for the thumb. The former fingers begin with the metacarpals, which are attached to the proximal phalanges via the proximal interphalangeal joints (PIP), followed by the distal phalanges, attached through the distal interphalangeal joints (DIP) (eOrthopod, n.d.). However, the thumb is different in that it does not contain a second phalangeal, and, secondly, there is more freedom of movement in the carpometacarpal articulation (Taylor and Schwarz, 1955).
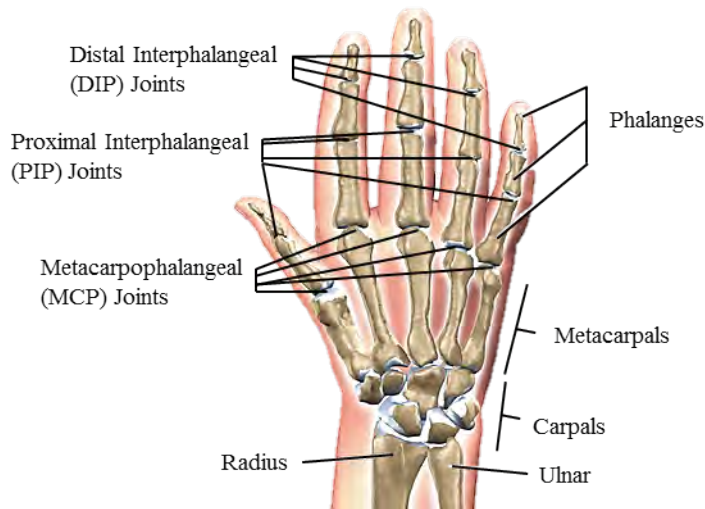
Figure 2.1: Bones of the Hand

2.1.1.2   Tendons and Ligaments

Tendons of the hand are predominantly controlled by muscles that exist in the forearm. Flexor tendons are guided in–between the carpal bones by a system of tube–like pathways. Furthermore, the extensor tendons are guided by the dorsal carpal ligament. In addition, sheaths act as guides for tendons of the fingers (Taylor and Schwarz, 1955). Since the fingers are responsible for such high functional ability, their tendon arrangement is most important.

The function of ligaments in a finger is to prevent abnormal joint movements, as well as hold the two bones of a joint together. Collateral ligaments exist on both sides of finger and thumb joints, and prevent excess lateral movements. Another ligament, the volar plate, is in the proximal interphalangeal (PIP) joint, and prevents hypherextension (over extending the joint) (eOrthopod, n.d.).

On the other hand, tendons give movement functionality, and are categorised into flexor and extensor groups. The extensor tendons enable each finger to straighten out, whereas the flexor tendons close the fingers. The extensor tendons are attached to the fingers by the extensor hood. The central slip is the area in which the extensor tendon attaches to the middle phalangeal (eOrthopod, n.d.). The extensor tendon arrangement on an index finger can be seen in Figure 2.2 (MMG, 2001*a*,*b*).

The flexor category consist of the flexor digitorum profundus (FDP) and flexor digitorum superficialis (FDS) tendons. These are situated on the palm side of the fingers, and are enclosed by the digital flexor sheath. The sheath facilitates with tendon sliding, nutrition, and acting as a fulcrum during flexion (Bates *et al.*, 2013).

The digital flexor sheath is made up of a membranous and retinacular portion, shown in Figure 2.3 (a) (Turpen, n.d.*a*) and (b) (Turpen, n.d.*b*), respectively. The membranous portion holds the tendons within the retinacular portion. The retinacular portion is desribed as a pulley system, thought to consist of the palmar aponeurosis (PA) pulley, 3
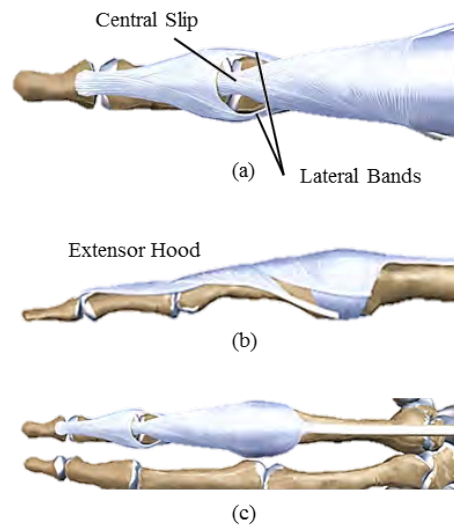
Figure 2.2: Extensor Tendons of a Finger: (a) Partial top view of extensor tendons, (b) Full side view of extensor tendons, (c) Full top view of index finger with extensor tendons, alongside middle finger.

cruciform pulleys, and 5 annular pulleys. These assist with keeping the tendons close to the joint rotational axes, for mechanical advantage (Bates *et al.*, 2013).
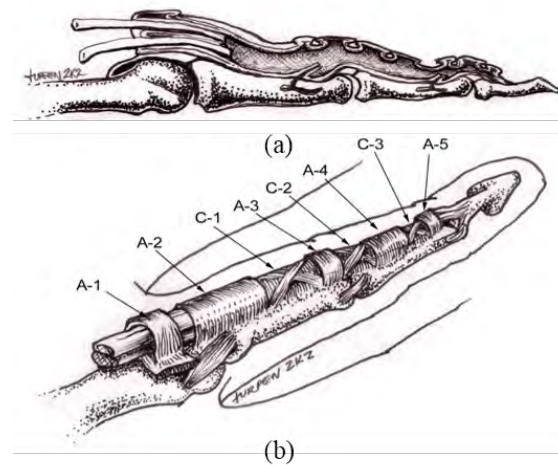
Figure 2.3: Digit Flexor Sheath: (a) membranous portion, (b) retinacular portion with pulleys A-1 to A-5 (annular), and C-1 to C-3 (cruciform)

2.1.2 Osteokinematics

Osteokinematics in the hand concerns the gross movement of joints, whereas arthrokinematics concerns motion at joint surfaces (Lippert, 2011). The osteokinematics of the hand can be described through the motions of the forearm, wrist, fingers, and thumb.

Rotational movements are described relative to a plane. These planes are shown in Figure 2.4 (American Society for Surgery of the Hand, 2006*a*) by a dotted line for each movement illustration. Rotation of the forearm is termed supination or pronation. Rotation of the wrist, from a side view, is described by extension and flexion, and from a top view by ulnar deviation and radial deviation. The side view of the fingers show flexion, extension, and hyper-extension (over extension). From the top view of the fingers, the middle finger is used for the reference plane. Moving either the index, ring, or small finger away from the middle is abduction, whereas moving the fingers toward the middle finger is known as adduction.
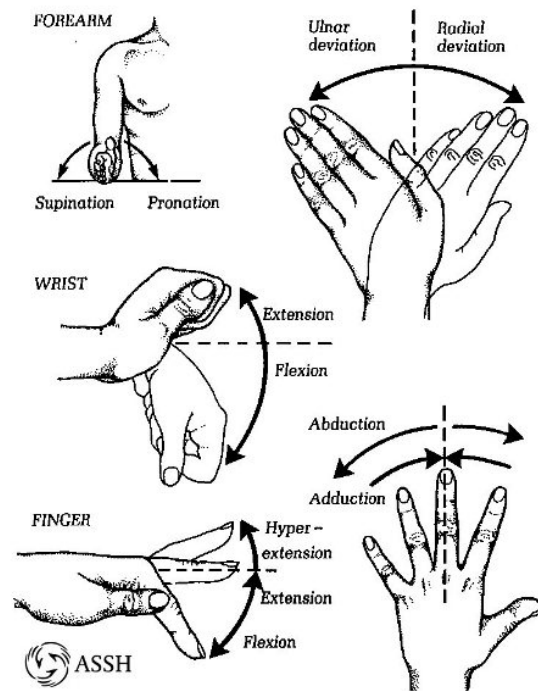
Figure 2.4: Motion of the Hand: Forearm, Wrist, and Fingers

Movement of the thumb requires a separate description due to its complexity, as can be seen in Figure 2.5 (American Society for Surgery of the Hand, 2006*b*). Extension and flexion describes the thumb IP joint rotating along the plane of the palm. The CMC joint allows the thumb to move away from the palm by palmar and radial abduction, in planes perpendicular and parallel to the palm, respectively. More complex movements are retroposition and anteposition, which describe how the thumb can rotate about the palm.

2.1.3 Grasp Taxonomy

A grip (or grasp) taxonomy categorises the different types of grasps used by a human hand. This helps to understand how the hand is used to grasps differently shaped objects. Identifying which grasps are most frequently used can assist the design of a more dextorous
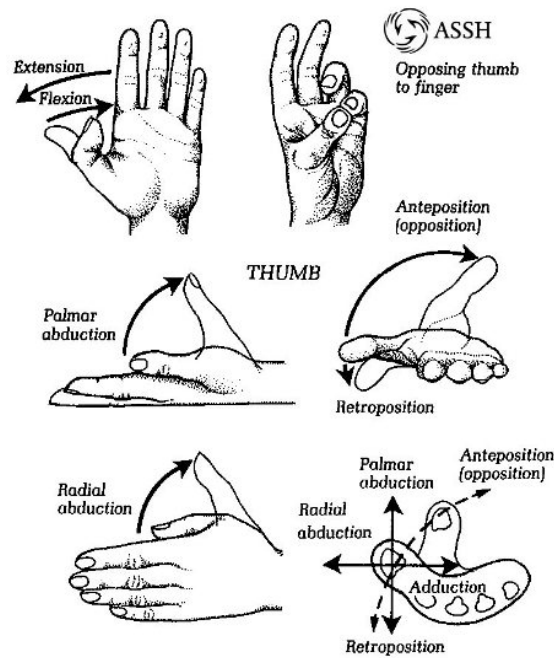
Figure 2.5: Motion of the Thumb

prosthetic hand, while minimising the complexity. Studies relating to this subject are reviewed here in order to achieve the aforementioned goal.

Napier (1956) categorised the movements of the hand within two main groups: 1) prehensile movements — movements during which the hand is grasping or about to grasp a desired object; and 2) non–prehensile movements — the hand is used to manipulate objects without grasping them. Napier (1956) further categorised prehensile movements into: 1) Power grip — an object is held between partially closed fingers and the palm, with the thumb pushing on the object close to the plane of the palm; and 2) Precision grip — an object is pinched between the distal ends of the fingers and thumb.

Napier's grasps taxonomy lacked detail, which is attended to by the taxonomy resulting from a study by Cutkosky (1989). The grasps are separated into two main types: power and precision. The sub-type grasps become more detailed moving down the tree, whereas power, dexterity, and object size separate the grasp types horizontally. Although it is more detailed, it focuses on tasks used by manufacturing machinists. Cutkosky (1989) describes a major limitation of the taxonomy as being incomplete because it does not consider everyday grasps such as with writing with a pen or pencil.

A more comprehensive grasp taxonomy was presented by Feix *et al.* (2009), which takes grasps of daily living into consideration. 33 different grasps were included, and could be arranged into 17 types for less accurate classification.

This comprehensive taxonomy was consider by Bullock *et al.* (2013) in a study to identify the most frequently used grasps by a machinist and a house maid during work and daily activities. The taxonomy was slightly modified (See Table 2.1, given by Bullock *et al.* (2013)), by rather using grasp type names given by Cutkosky (1989), as well as including

the platform grasp. Gravity dependent grasps such as the hook grasp and flat hand grasp were not included in the taxonomy, however the hook grasp can be similarly compared to the medium wrap grasp in the table.

Table 2.1: Grasp Taxonomy

		Power					Intermediate			Precision				
Opp	Palm		Pad				Side			Pad				Side
VF2	3-5	2-5	2	2-3	2-4	2-5	2	3	3-4	2	2-3	2-4	2-5	3
Thumb Abduction	Large Diameter / Small Diameter / Medium Wrap / Power Disk / Power Sphere		Ring	Sphere-3 Finger	Extension Type / Sphere-4 Finger	Distal Type	Adduction		Tripod Variation	Thumb-Index Finger / Tip Pinch / Inferior Pincer	Thumb-2 Finger / Tripod	Thumb-3 Finger / Quadpod	Thumb-4 Finger / Precision Disk / Precision Sphere	Writing Tripod
Thumb Adduction	Index Finger Extension	Adducted Thumb / Light Tool / Fixed Hook / Palmar / Platform (No VF2)					Lateral Pinch / Stick / Ventral	Lateral Tripod					Parallel Extension	

Bullock *et al.* (2013) ordered the grasp types from most to least frequent. The top 10 of these, in order of most to least frequent, are: medium wrap, precision disk, lateral pinch, tripod, lateral tripod, power sphere, thumb-2 finger, index finger extension, light tool, and thumb-3 finger. These account for approximately 80% of the total observed grasp duration.

2.2   DESIGN CONSIDERATIONS

Finger joint mechanisms, actuation methods, and materials were three important areas of consideration for the mechanical design. Much effort particularly went into the first

two areas, as they were the most challenging. Understanding the success and failure of previous work in these areas helped conceptualise an improved design. Each of these are discussed in this section.

2.2.1 Underactuated Joint Mechanisms

There are commonly between 8 and 16 joints or degrees of freedom (DOF) in prosthetic hand designs in literature (Dalley *et al.*, 2009). The DOFs are all less than the degrees of motion (DOM), known as underactuation, with the DOM depending on the number of actuators. Up to 6 actuators can be found in prosthetic hand designs, typically driving one of four methods of underactuation; differential drives, compliance couplings, kinematic linkages, or a combination of these (Dalley *et al.*, 2009).

These underactuation methods are used to passively move a number of joints within a digit, while actively driving one joint. They are generally applied to minimise used space (Carozza *et al.*, 2004). This can be seen in the designs of Zollo *et al.* (2007); Dalley *et al.* (2009); Carozza *et al.* (2004). Differential drives are used to simultaneously distribute driving forces between two joints. In other words, two fingers could be driven by one actuator, but they would move together. Alternatively, joint compliance enables joint positions to change relative to one another, with an external load, without a change in the driving joint position. This has given mechanical fingers the ability to adaptively wrap around the surface of objects, distributing surface forces more evenly along the finger.

As another option, rotational motion between joints can be related using a design of kinematic linkages. The relative motion between these joints are predetermined, and fixed (Kyberd *et al.*, 2001). This method is generally best for achieving larger grip forces (Carozza *et al.*, 2004). A combinational method would attempt to balance the simplicity and complexity of all the aforementioned methods.

Carozza *et al.* (2004) designed a novel adaptive finger grip using pulleys and springs, driven by a sliding actuation mechanism in the SPRING Hand. There are three tendon cables (distal, interphalangeal, and proximal), each connected to one of the three joints in a finger. The distal and proximal cable are connected to a linear spring to accommodate for cable displacements with fixed joint positions. When the proximal phalangeal comes into contact with an object, the metacarpophalangeal (MP) joint positions becomes fixed, but the spring proximal phalangeal begins to compress, allowing the middle phalangeal to come in contact with the object. This continues until the distal phalangeal is in contact with the object. The principal operating sequence of this design can be followed in Figure 2.6 (Carozza *et al.*, 2004).

The actuation drives commonly adopt one of two driveable techniques. Firstly, and most frequently used, are non-backdriveable (self-locking) drives. These can be driven by an internal actuation input, but cannot be driven by external loads (van der Riet, 2014). Zollo *et al.* (2007) and Carozza *et al.* (2004) both used a slider mechanism that is driven by a motor through a lead screw, pulling the tendon wire/s for each digit. The prominant
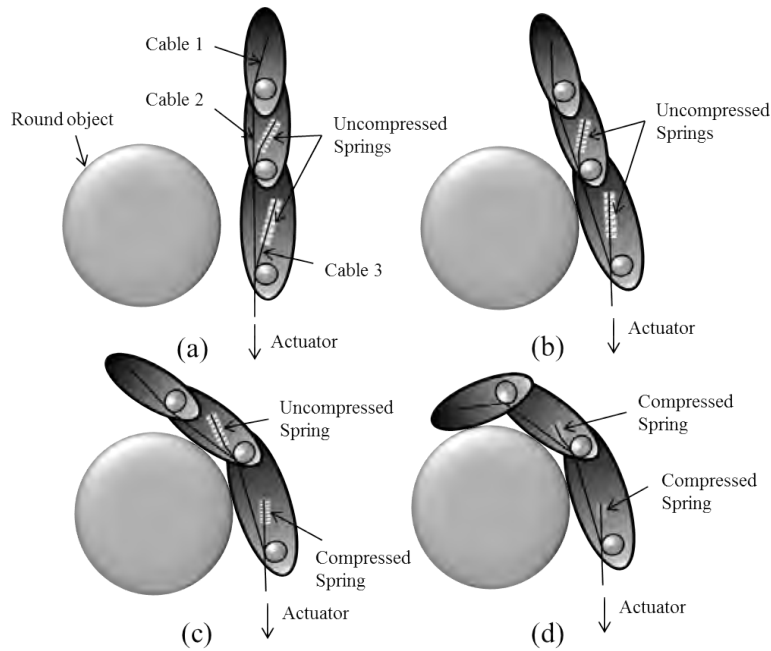
Figure 2.6: Adaptive Grip Example: (a) intial full extension position (b) proximal phalangeal in contact (c) middle phalangeal in contact (d) distal phalangeal in contact

advantage of this is that energy required for actuation is conserved when an external load is present.

The other approach is using a backdriveable configuration that will operate by either an internal or external force/torque. Dalley *et al.* (2009) used this in an attempt to replicate natural force feedback by visual examination. The positions of the fingers would move depending on external forces. This was because of its implicit force control via positional control, inherent in the spring design and configuration. One major disadvantage of this design was that the springs would constantly induce a load on the motors, even when the fingers had no other external loads, implying the use of larger motors that would be consistently draining power. An increase in battery power capacity and motor size are results that should be avoided to minimise the size and weight of the design.

2.2.2 Methods of Actuation

Selecting a specific actuation technology can change the design on the hand holistically. Actuation and power generation components will affect size, cost, and complexity requirements. Most prosthetic hand designs attempt to fit actuation systems within the palm of the hand. This accommodates transradial amputees up to the wrist. A description and discussion on various actuation technologies used in literature are presented to aid with selection.

2.2.2.1   Motors

In previous prosthetic hand designs the most common actuation sources are motors, predominantly brushed dc–motors, but there are some designs using brushless technology. This is clear from the review done by Belter and Dollar (2011). Additionally, a third type of motor was used by Kamikawa and Maeno (2008), and is called an ultrasonic motor.

There are a number of pros and cons to consider when selecting a motor. Brushed dc-motors have the advantage of being very low cost and easy to control. Their main disadvantages are due to the brushes limiting the speed, generating electromagnetic interference (EMI), and requiring regular maintenance.

Comparing brushless dc-motors to brushed technology, the advantages are: wide speed range, high efficiency, high power to weight ratio, low EMI, and reduced size. The major disadvantages of these motors include high cost, complex control, more lead wires, and additional circuitry.

Ultrasonic motors are based on technology that use piezoelectric material and vibrations to produce rotation. These motors have high torque and low speed characteristics, thus do not require external gearing. They are extremely compact, have high power to weight ratios, efficiency, and low noise generation. Although the motors themselves do not generate EMI the high frequency power supply does (Uchino, 1997). This technology is still quite new, and not easily available.

2.2.2.2   Body Powered

Body powered prosthetics, as the name suggests, use the movement of the body to induce movement in the prosthetic device. An example can be seen in the development of a body powered prosthetic hand by Doshi *et al.* (1998). The design uses a cable to open and close the fingers for grasping. This cable could be strapped around the shoulder of the opposite arm. The hand will then open and close depending on the pulling action due to the movement of the shoulder. Prostheses using this actuation are quite simple in design as well as low in cost, due to the simplicity and not requiring any electronics.

2.2.2.3   Hydraulic

In 2009, Gaiser *et al.* (2009) published the developments of the Fluidic Hand III, shown in Figure 2.7 (Gaiser *et al.*, 2009). This hand improved on the previous design, the Heidelberg Hand, with its actuation dependent on a hydraulic system. Pressure on a fluid (water) was generated using a small pump. This pressure could be distributed to each of the fingers using customised miniature valves. These valves controlled the flow of fluid into flexible fluid actuators — flexible bellows in this case — situated at selected finger joints. This in turn provided torque and position control at these finger joints.

The hand is capable of grasping a cyclindrical 60 mm diameter object with a force of 65 N, and an individual finger force of 45 N. The total mass of the hand is 400 g. Thus, the

Actuator   Pump   Valves

Figure 2.7: Fluidic Hand III

hand exhibits a good power to weight ratio. One drawback is that if there are any fluid leaks, the pressure losses will cause the hand to be useless. A second drawback is that it requires customised valves, which would result in high manufacturing costs.

2.2.2.4   Pnuematic

Pnuematics uses pressurised air to produce motion through a mechanism. Takeda *et al.* (2009) applied this technology to create a unique artificial muscle, placed at each finger joint to be controlled. The actuators consist of a rubber balloon covered by a net, and a feeding channel. When compressed air is injected into the actuator through the feeding channel, the rubber balloon expands, the surface of the net deforms and pulls the attached line, producing a tension force.

The actuators fitted well into the hand, as shown in Figure 2.8 (Takeda *et al.*, 2009), and enabled position and force control of the majority of the digit joints. It is able to grasp objects up to 500 g, or approximately 5 N, which is only 7.7 % of the grasp force produced by the Fluidic Hand III. Although the design is described as simple, the components used to generate the compressed air are situated in an extended arm design, and not within the palm of the hand.

2.2.2.5   Shape Memory Alloys

A novel design by Andrianesis and Tzes (2008) used shape memory alloys (SMAs) as artificial tendon actuators. When heated, these SMAs begin to contract at specific transition temperatures. This contraction would be used to open/close the fingers individually via intricate locking mechanisms, within the palm of the prosthesis, fixing the fingers in position when actuation forces were not present.

Figure 2.8: Pnuematically actuated hand without cosmetic glove

The hand, illustrated in Figure 2.9 (Andrianesis and Tzes, 2008), uses SMAs in the form of wires, which can be heated via an electric current — Joule heating. With about 3–5 % strain, the displacement characteristics of these alloys are quite low. Hence, a space consuming actuation system was used, extending into the wrist, in order to produce a sufficient amount of force to the fingers. A second drawback is that these alloys require a cooling time to extend back to their original positions, prolonging the closing time of the fingers. An optimised design time of 2.2 s was established — approximately twice the ideal time of 1 s. Although there are a number of cons, the advantages include silent actuation and ultra–light weight (250 g without electronics).
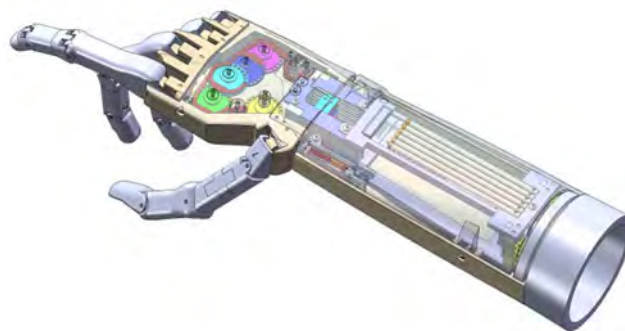
Figure 2.9: Shape memory alloy actuated hand

2.2.3   Materials

The combination of materials used in prosthetic limbs, providing physical stiffness and strength, need to balance cost, mechanical performance, and weight. There are a variety of traditional (metals) and modern (polymer matrix composites (PMCs) and plastics) materials being used in prosthetics. The mechanical properties, manufactureability, and cost of these materials are important in evaluating the most approriate materials for a

low–cost design. Table 2.2 presents a list of distinct materials used in prosthetic hand research, followed by a description of each.

Table 2.2: Major Materials in Prosthetics

Material Type	Material Name	Research Reference
Metal	Aluminium	(Zhao *et al.*, 2006), (Kargov *et al.*, 2007)
Metal	Titanium	(Schulz *et al.*, 2005)
PMC	Carbon Fibre	(Zollo *et al.*, 2007), (Light and Chappell, 2000)
Thermoplastic	un–named	(Dalley *et al.*, 2009), (Light and Chappell, 2000)
Thermoplastic	ABS	(Pasluosta *et al.*, 2009), (Xu *et al.*, 2011)

2.2.3.1   Metals

Aluminium(Al) and Titanium(Ti) occur most often in recent prosthetic hand designs, with the majority using aluminium. Aluminium is a lightweight, abundant nonferrous metal, which is most commonly used. Although its stiffness and strength is lesser in comparison to Titanium, the cost is generally much less. A special feature of Titanium is described by Wang (1996) as having exceptional tissue compatibility, and so the human body does not reject the metal. This could possibly allow future prosthetics to be attached directly to bone.

2.2.3.2   Polymer Matrix Composites

Polymer Matrix Composites consist of fibres, flakes, or particles used to reinforce a polymer. Fibre–reinforced polymers use high–strength fibres for reinforcement, embedded in a thermosetting plastic. These composites have comparable strength and stiffness to steels, yet they are usually one fifth of the weight. A major disadvantage is that the manufacturing process is quite tedious, requiring custom moulds and combining the polymer resin with the fibre.

2.2.3.3   Thermoplastic Polymers

Thermoplastic polymers have the primary characteristic of maintaining their properties after being heated into a liquid state and cooled back into a solid, multiple times. Acrylonitrile Butadiene Styrene (ABS) has become a popular thermoplastic used in rapid prototyping technology, namely Fused Deposition Modelling (FDM). FDM is an additive process, whereby a 3D CAD model is created by multiple polymer layers, extruded through a heated nozzle. Other related techniques include selective laser sintering (SLS),

and stereolithography (SLA), but are more expensive. FDM can be achieved using devices commonly termed 3d printers that fall within the affordable $ 500 –$ 20,000 price range. Low material cost and almost unrestricted part shapes are the major advantages for these materials.

2.3 MECHANICAL DESIGN

The following section describes the process of the implemented mechanical design details, beginning with the initial concepts of the fundamental subsystems, then going into further detail on the physical design of the primary parts, and then moving through to the selection of dc motors for actuation. Single body, static finite element analysis is shown to describe how some dimensions were optimised. The section ends with a presentation of the final assembly, followed by a kinematic model and analysis of the fingers.

2.3.1 Method of Actuation

From the discussions made in section 2.2.2, and specifically section 2.2.2.1, the benefits of using brushed–dc motors outweight the other options of actuation. Low–cost, simple voltage control, reliable operation, and high mechanical power density make them highly desireable, and are the reasons for selecting this method of actuation. This was an important first step made in the design process, since initial concept shapes and mechanisms depended greatly on the method of actuation.

2.3.2 Finger Concepts

A number of concepts were generated for the fingers, however only a selected few are described here that show some of the major differences in the options. The human finger naturally has three joints (MCP, PIP, DIP) and so it felt necessary to reflect this in the fingers to re–create a more natural movement and appearance, assisting the amputee in accepting the prostheses.

A simple baseline or reference concept of the fingers was used to assist with further concept generation, as can be seen in Figure 2.10. This illustrates only the major parts of the fingers and where the palm would be situated. A new concept would only require the internal mechanisims to be added to the image. T_{MCP} represents a torque applied on the proximal phalangeal at the MCP joint to provide finger motion.
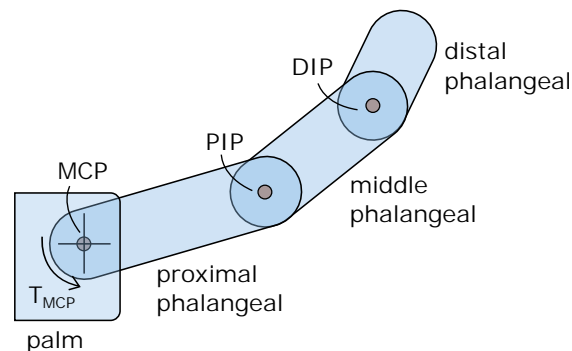
Figure 2.10: Finger Concept Reference

2.3.2.1 Bar Linkage

The first concept, illustrated in Figure 2.11, was one that is commonly used in research and commercial designs. It uses bars or beams to link adjacent phalangeals such that when the proximal phalangeal is rotated about the MCP, the other joints will rotate with a relative profile. In this image, bar a is attached to the palm and middle phalangeal at rotation points 1 and 2, respectively. Bar b is attached to the proximal and distal phalangeals at rotation points 3 and 4, respectively.

The attractive characteristics of this concept are that it is simple to understand and can generate high forces. Determining the linkage lengths and positions to give desired relative joint positions and torques throughout the motion profile requires complex linkage design theory.
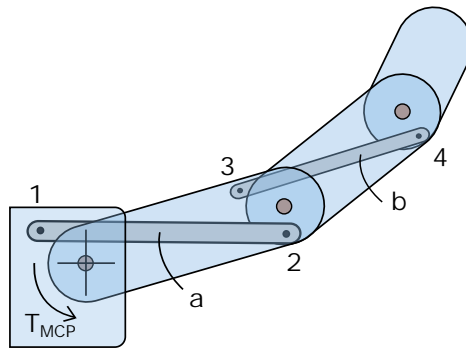
Figure 2.11: Bar Linkage Concept

2.3.2.2 Cable Linkage

The following novel concept achieves similar linkage characteristics to the bar linkage concept, but it is based on using cables instead or bars. Ropes a, b, c, d in Figure 2.12 are attached to specific virtual pulleys 1, 2, 3, 4 at each of the joints, such that each adjacent joint rotates a defined relative ratio with respect to one another. This ratio is determined by the virtual pulley diametres. Virtual pulley 1 is fixed to the palm, virtual pulley 2 is fixed to the proximal phalangeal, virtual pulley 3 is fixed to the middle phalangeal, and virtual pulley 4 is fixed to the distal phalangeal. Cables a and b are connected to virtual pulleys 1 and 3, and cables c and d are connected to virtual pulleys 2 and 4.

The relationship of relative motion and torques between joints are simplified by using the virtual pulley ratio, allowing simplified kinematic design. Cables are lighter in weight and have smaller dimensions in comparison to bars, but can still have similar strength properties depending on the materials. Four cables and eight connection points would make the design more intricate in comparison to the bar linkage concept, using two bars and four connection points.
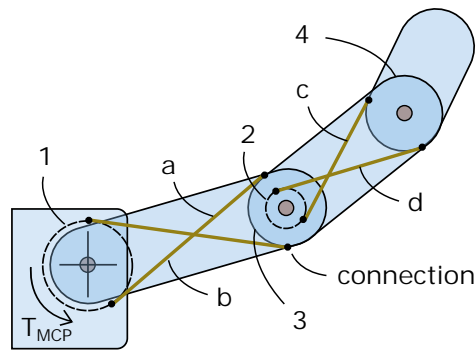
Figure 2.12: Cable Linkage Concept

2.3.2.3   Two–Cables and Pulleys

While the cable linkage concept links the relative motion of joints, the concept depicted in Figure 2.13 allows the joint motion to rather depend on when a phalangeal comes in contact with an object. Here there are two cables a and b attached to a virtual pulley on the distal phalangeal. Pulleys 1 and 2 are placed at the MCP and PIP joints, respectively, on which the cables are wrapped and run along. Cable forces F_1 and F_2 are used to either close or open the finger. During closing, if the proximal phalangeal comes in contact with an object, that phalangeal will stop moving while the cables continue to run along the internal pulleys, closing the middle and distal phalangeals onto the object.

The prominent feature of this concept is the ability to adapt to the shape of an object to be gripped, continuing to close onto it until all the phalangeals are in contact with the object. This would not give the fingers a natural finger motion and they may be in awakward positions while gripping an object in certain ways. This is because the cables are only attached to the distal phalange, while they slide over the other joints during motion. An example would be pinching a pen; the distal phalangeal would only be in contact with the pen, and the entire finger would be straight because the cable would not fix the MCP and PIP joint positions, while naturally the finger would have a slight curve.
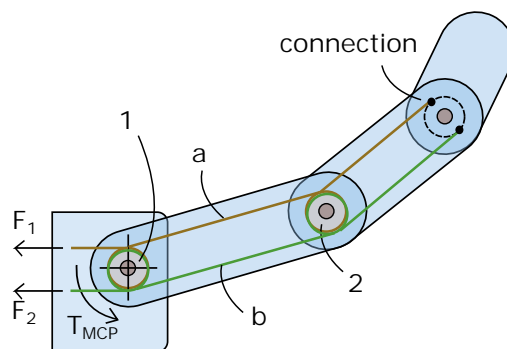
Figure 2.13: Two–Cables and Pulleys Concept

2.3.2.4 Six–Cables and Pulleys

The two–cables and pulleys concept can be modified into a concept using six cables instead of two, shown in Figure 2.14. Keeping the pulleys and the cables connected to the distal phalangeal as before, two more cables (brown and yellow in Figure 2.14) are connected to the middle phalangeal at the PIP joint and an additional two (purple and red in Figure 2.14) connected to the proximal phalangeal at the MCP joint. Forces $F_{1,2,3,4,5,6}$ are individually applied to the cables to open and close the finger, controlling the net joint torque, T_{MCP}, applied on the proximal phalangeal at the MCP joint. This concept addresses the lack of joint position control in the two–cables and pulleys concept, but adds the complexity of additional cables, connections, and controlled forces.
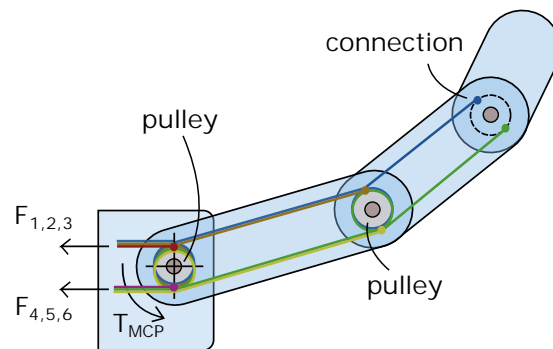
Figure 2.14: Six–Cables and Pulleys Concept

2.3.2.5 Cables and Springs

The complexities of the six–cables and pulleys concept can be avoided by adding in two springs, resulting in the concept of Figure 2.15. This mechanism allows the finger to be actuated through only two forces, F_1 and F_2, while still maintaining joint position control via the springs. When in contact with an object, the finger will wrap around it while the springs are compressed, giving it an adaptable characterisitc. Spring a is attached between the pulley at the MCP joint and the proximal phalangeal, while spring b is attached between the pulley at the PIP joint and the middle phalangeal. The cables in this concept are connected directly to these pulleys.

This concept seems to have all the desireable characteristics, though mechanical power will be used as long as the springs are in compression, exchanging energy loss for an adaptable grip. A complexity would be selecting the size and stiffness of the springs to give a desireable motion. Too low a stiffness would result in lower enegry losses, but slower motion responses and higher joint oscillations. Too high a stiffness would result in larger energy losses during adaptable gripping (spring compressions).
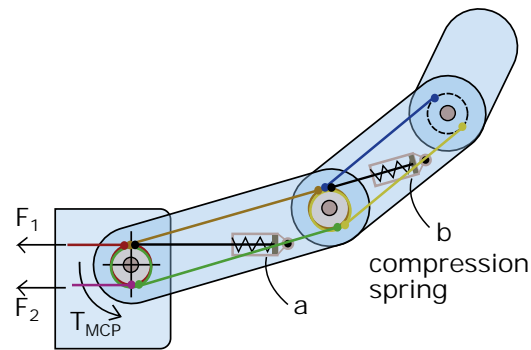
Figure 2.15: Cables and Springs Concept

2.3.2.6   Concept Selection

When selecting the finger concept for implementation, the important criteria that were considered were:

1. ease of assembly

2. costs

3. ease of design

4. natural joint position control

5. adaptable gripping

6. energy conservation

After using these as a first evaluation, two concepts stood out as satisfying the criteria the most; the cables and springs concept and the cable linkage concept. A comparison between these concepts is worth noting to support the final selection. They are both similar with their ease of assembly, and natural joint position control. The former option has more adaptable grip, however less energy conserving, whilst the latter has a lower cost and is more simple to design due to not requiring springs. From this comparison it was decided that the best option would be the cable linkage concept.

2.3.3   Finger Actuation Mechanism Concepts

Once the finger concept had been finalised, the next challenge was generating concepts for the mechanism that would assist the actuation of all the fingers, excluding the thumb. The mechanical power would originate from a dc–brushed motor, as discussed in section 2.3.1. Four concepts were considered, using combinations of gears, nuts, bar linkages and pulleys. The major difficulty was coupling the motors in a position and orientation, such that space was used optimally, to the proximal phalangeal of the fingers.

2.3.3.1 Nut–Screw Bar Linkage Concept

Combining a screw with a bar–linkage generated the concept of 2.16. A nut mates to a screw driven by a motor. The nut has a pivot pin slotted just above it to allow an attached bar link to rotate during movement. The same bar is attached via a pivot pin to the MCP joint of the proximal phalangeal. When the screw is turned by the motor, the nut is translated along the rotational axis of the screw. In turn the bar link is pushed, turning the MCP joint.
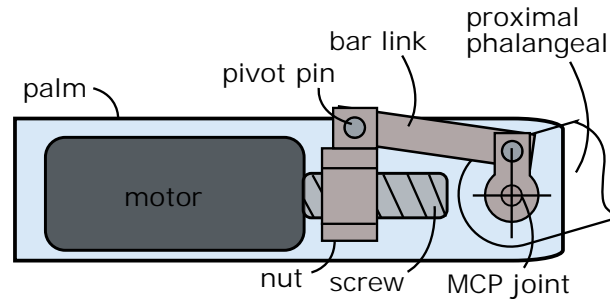
Figure 2.16: Nut–Screw Bar Linkage Finger Mechanism Concept

2.3.3.2 Worm–Gear Concept

The worm–gear mechanism illustrated in Figure 2.17 situates the motor closer to the MCP joint, but requires the motor axis to be offset. The worm mounted to the motor shaft drives a gear mounted to the proximal phalangeal. Turning the worm one way or the other will control the finger motion direction.
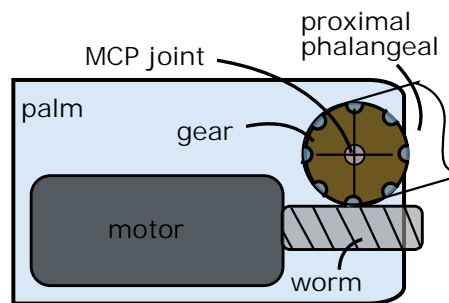
Figure 2.17: Worm–Gear Finger Mechanism Concept

2.3.3.3 Worm–Gear Pulley Concept

Continuing with the worm–gear idea, a modification can be made such that the gear rotates on a separate axis from the MCP joint. The gear is linked to the MCP joint by a cable. The pulleys labelled 1 and 2 are fixed to the gear and MCP of the proximal

phalangeal, respectively. The motor is in a similar position to the concept using the bar linkage.
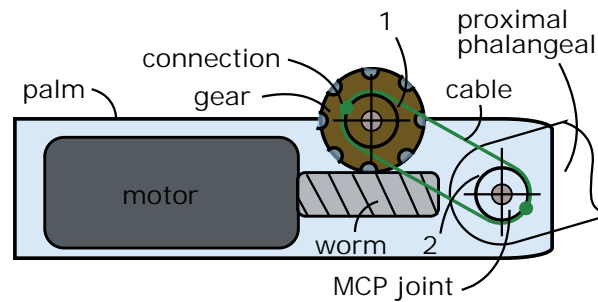
Figure 2.18: Worm–Gear Pulley Finger Mechanism Concept

2.3.3.4 Pulley Concept

Replacing the worm or screw in the previous concepts with a pulley, and using a passive pulley in place of the gear in the worm–gear pulley concept, forms the concept shown in Figure 2.19. Pulley 1 is passive and pulley 2 is fixed to the proximal phalangeal at the MCP joint. A cable is fixed and wrapped around the motor pulley, fed over pulley 1, wrapped around and attached to pulley 2 before following a similar path back to the motor pulley. When the motor pulley is turned, the cable is pulled over pulley 1, rotating it, and rotating the MCP joint.
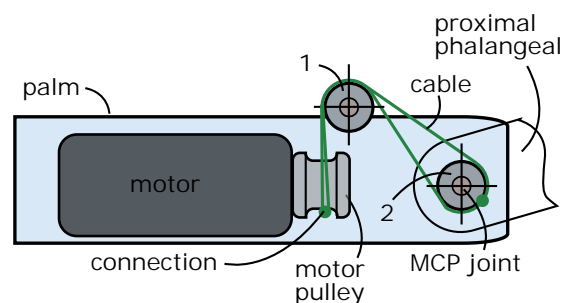
Figure 2.19: Pulley Finger Mechanism Concept

2.3.3.5 Concept Selection

The advantages of each mechanism concept were considered before making a selection. A common disadvantage of the concepts using a worm–screw is that space is taken up by it. The length of the worm–screw is determined by the range of motion desired for the MCP joint. During a conceptual CAD phase, this length resulted in requiring about double the space of the pulley mechanism. This would then result in using a smaller motor. Self–locking is an advantage for all the concepts with a worm–screw.

The nut–screw bar linkage concept would be able to produce a high torque ratio, but friction will become an issue between the mating thread, wasting mechanical power. The dimensions of the bar linkage would be complex to select such that the torque produced throughout the range of motion of the MCP joint is optimised.

The worm–gear concept is the most simple, but the offset necessary between the motor shaft and the MCP joint creates space issues, because the palm thickness is required to increase. Although the worm–gear pulley concept attempts to solve this problem, space was found to still be an issue after making estimations in 3D CAD.

The pulley concept solves the space problem by using a compact arrangement of pulleys. Further space optimisation can be made by moving pulley 1 closer to pulley 2, simultaneously moving the motor closer to the MCP joint. This then gives maximum space to be used up by the motor. Additionally, as in some of the other concepts, the motor axis is in line with the MCP joint, minimising the thickness of the palm. One main disadvantage of this concept is that it is not self–locking. Space usage optimisation was the deciding factor for these concepts, resulting in the pulley concept being selected.

2.3.4   Concepts of the Palm

Following the decision of the finger motion mechanism, the next important concept was that of the palm. The palm should hold all the actuation devices for the fingers and the thumb, allow for them to be connected, but still have a shape that maintains rigidity and a natural aesthetic appeal. Two concepts are described that fulfill these objectives, but are different in the way the fingers, excluding the thumb, are attached.

The slanted palm concept of Figure 2.20, shows the fingers connected by an individual MCP joint rod for each finger. The rods of adjacent fingers are slightly offset to give a more natural looking hand shape.

Comparing this to the straight palm concept shown in Figure 2.21, it is clear that they differ with the MCP joint design. The fingers of the slanted palm concept share the same single MCP joint rod. Although this may not give a more natural look, it not only simplifies the mechanical assembly but it reduces manufacturing time by requiring six less measured cuts. For these reasons, the latter concept was selected.

2.3.5   Concepts of the Thumb

Although the human thumb has five degrees of freedom, re–creating the same number of degrees of freedom (DOFs) using mechanisms and motors is extremely challenging. The problem can be simplified by removing the less important degrees–of–freedom. What is left are two DOFs, both actuated, namely one DOF in the CMC joint and one DOF in the MCP joint. Concepts for the actuation of these DOFs were generated, and are described in the follwing subsections. Firstly, the concepts for CMC joint actuation are described, followed by the concepts for MCP joint actuation.
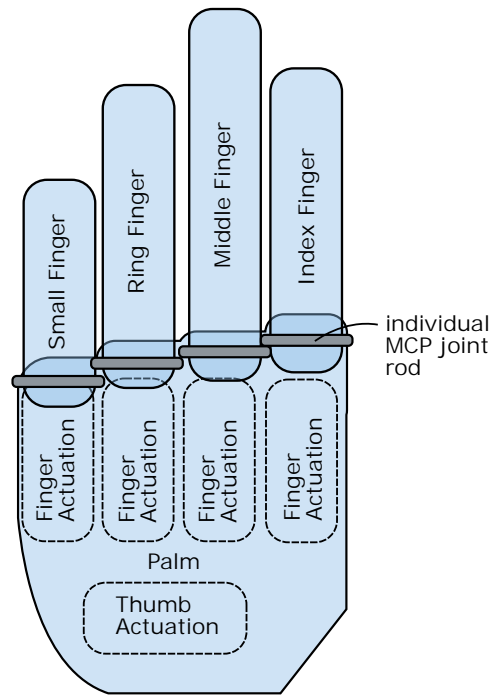
Figure 2.20: Slanted Palm Concept
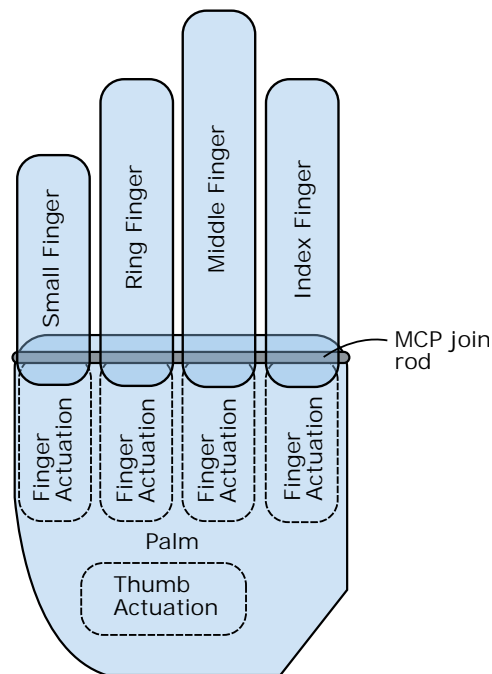
Figure 2.21: Straight Palm Concept

2.3.5.1   Worm–Geared CMC Joint Concept

The concept of Figure 2.22 is used in the i–limb–ultra commercial hand, and is based on a motor driving a worm–gear mechanism. As shown, the CMC joint rotates about the labelled x–axis. The orientation of this axis constrains the thumb to move perpendicularly

to the palm, giving it a slightly unnatural motion. A benefit is that the worm–gear can be selected to give a high torque output and it is self–locking (with no applied motor voltage, an externally applied torque will not rotate the motor).
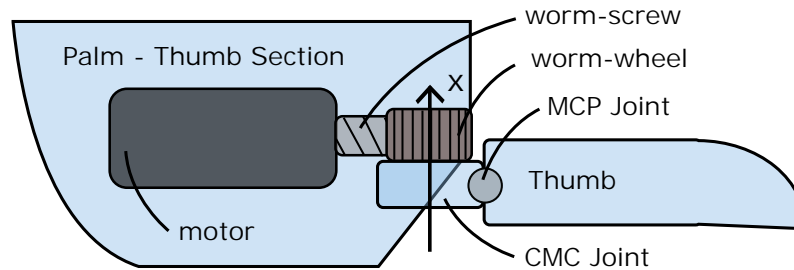
Figure 2.22: Thumb Worm–Geared CMC Joint

2.3.5.2 Pulley CMC Joint Concept

A more natural looking thumb motion can be achieved using the concept of Figure 2.23. This is because the rotational axis of the CMC joint has been tilted toward the centre of the palm, contraining the thumb motion to be at the same relative angle to the palm. A pulley on the motor has a cable attached to it, which is driven along a passive pulley to accomodate the angled joint. The following section of cable runs around the diametre of the CMC joint, attached to it, and back along a similar path to the motor pulley. The disadvantage is that the drive is not self–locking.
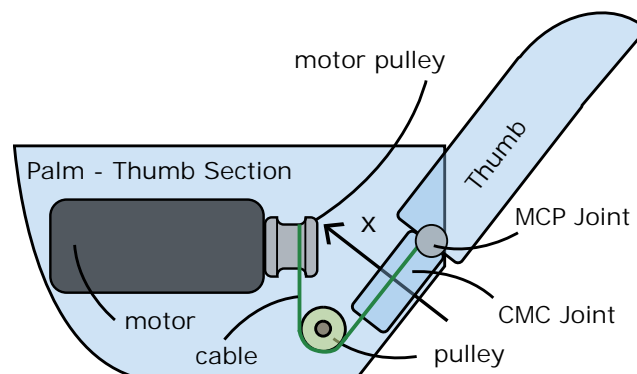
Figure 2.23: Thumb Pulley CMC Joint

2.3.5.3 Nut–Screw Cable MCP Joint Concept

To provide actuation to the MCP joint of the thumb, space within the thumb had to be used as there was none available in the palm. A nut–screw mechanism is attached to two separate cables (red and green) in the concept of Figure 2.24. The figure shows a cross–section of the concept in 3D CAD. When the nut is moved along the axis of the screw by the rotation of the motor shaft, the tension in one cable increases whilst the

other is given more slack, pulling the thumb around the MCP joint. The green cable runs through the inside casing of the thumb and around a circular diametre of the dashed circle labelled 1. Friction due to the cable sliding along the circular surface through the end–cap would cause power losses. Sufficient space for the nut to move, such that the thumb is able to rotate at least ninety degrees, proved to be a major problem with this concept.
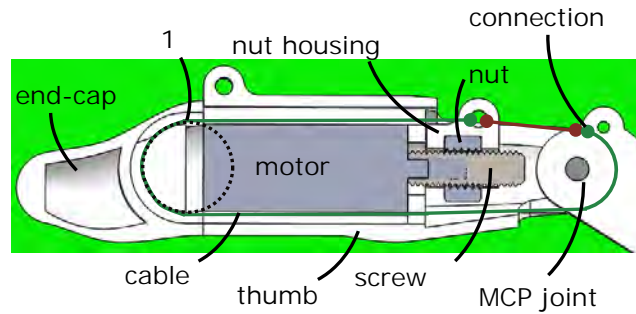
Figure 2.24: Thumb Nut–Screw MCP Joint

2.3.5.4 Pulley MCP Joint Concept

The second MCP joint concept, shown in the 3D CAD cross–section of Figure 2.25, similarily has the motor placed within the thumb. Here a pulley is driven by the motor shaft. A cable is wrapped around and attached to the motor pulley, as well as around and attached to a virtual pulley fixed to the metacarpal phalangeal part. When the motor turns, one section of the cable on the pulley is wrapped further while the other section is unwrapped. The same can be said for the cable wrapped around the MCP joiint.
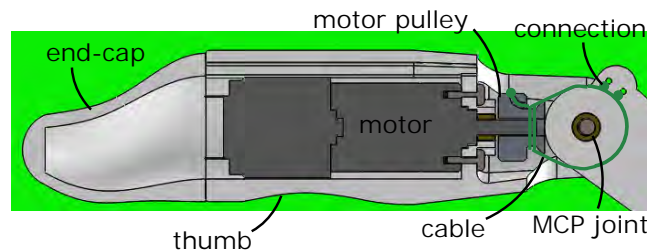
Figure 2.25: Thumb Pulley MCP Joint

2.3.5.5 Concept Selection

For the CMC joint, the worm–geared concept has the appeal of a higher torques ratio and it can self–lock, but it does not replicate a natural thumb orientation and motion. The worm lies underneath the gear, requiring and offset between their rotating axes. Because the motor is already offset from the lower surface of the palm, the mechanism will require more space than the CMC pulley concept.

On the other hand, the latter concept is not self–locking, but creates a more natural thumb orientation and motion. The CMC pulley concept was chosen to avoid space problems, and allow for a larger motor to be used. The natural characterisitics would please amputees to a larger degree.

One problem of the nut–screw concept for the MCP joint are the frictional effects, caused by the cable sliding against internal surfaces of the thumb, and between the thread of the nut and screw; this will reduce the transmission efficiency. The second problem was that of minimal space, as described in section 2.3.5.3.

The pulley concept for the MCP joint is more compact and avoids frictional issues, which were the reasons for selecting this option.

2.3.6 Detailed 3D Design

Using the selected concepts of the important sections of the hand, a detailed 3D design was created and is illustrated in Figure 2.26. The image includes the final motors of the design, of which the selection process is described later in section 3.2. The top cover and electronics have been excluded to show the internal components. The main features of this design are described here in further detail.
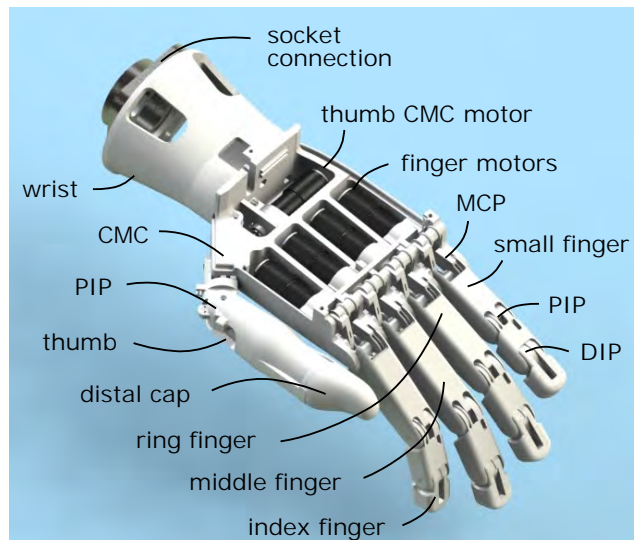
Figure 2.26: Detailed 3D Hand Design (no cover or electronics)

2.3.6.1 Material

Primary materials generally used in prosthetic hands were discussed in section 2.2.3. In section 2.2.3.3 the thermo plastic material named Acrylonitrile Butadiene Styrene (ABS) was said to be popular in FDM technology. This material was selected as the primary material for the hand design. Due to its popularity, the plastic costs around R 300 (approximately $ 25) for 1 kg, supporting low–cost manufacturing of parts with many curved

surfaces. The small UP! desktop 3d printer that costs about R 13,000 was easily accessible for part manufacturing. Using this technology would facilitate the use of additional 3d printers as high production rates are required.

2.3.6.2   Shape & Dimensions

Determining the size and shape of the hand, such that it can look proportionally correct on a large number of people, was important. Different sized versions of the hand could be made, but having one version reduces the total amount of documentation and versions of parts. Anthromorphic databases are made up of measurements of human dimensions that can be used as reference populations when creating designs.

The 1988 US Army Anthropometry Survey (ANSUR) is a commonly used database that was done on 1774 males and 2208 females (The Open Design Lab at Penn State, 2014a) . This data was used as a guideline for the hand dimensions, and where dimensions were unavailable, a specific human hand was used as a reference. These include dimensions such as finger widths and joint positions.

Measurements made on the hand in the ANSUR database are shown in Figure 2.27. The hand length is measure from the wrist to the end of the middle finger. The wrist–finger length is measured from the wrist to the end of the index finger. The hand circumference is measured around the knuckles.

© mpr, 2009   © mpr, 2009   © mpr, 2009

(a)   (b)   (c)
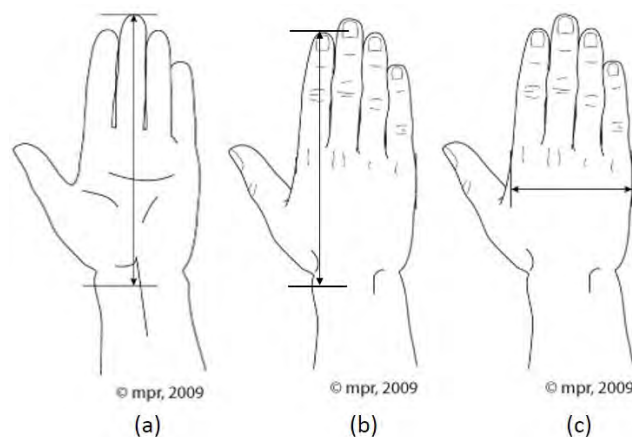
Figure 2.27: Hand Measurements in ANSUR Anthropometric Database: (a) Hand Length, (b) Wrist–Finger Length, (c) Hand Circumference

The percentile distributions of the data for females and males are listed in Table 2.3 and Table 2.4, respectively (The Open Design Lab at Penn State, 2014b) . The 50th percentiles represent values of which 50 % of the observations are found to be less than, or alternatively greater than. A more common termed used for this type of value is the median. Using the median values as initial dimensions assisted with designing for the average sized hand. Comparing the medians of the males and females shows that the male dimensions are

larger. In an attempt to accommodate males and females, medians of the genders were averaged to give initial design dimensions.

Table 2.3: Measurement Percentile Distributions for Females [mm]

Measure	1st	2.5^{th}	5th	10th	25th	$\mathbf{50^{th}}$	75th	90th	95th	97.5^{th}	99th
(a)	159	162	165	168	174	**180**	187	193	197	200	205
(b)	149	152	155	158	163	**169**	175	180	184	188	192
(c)	71	72	73	75	77	**79**	82	84	86	87	89

Table 2.4: Measurement Percentile Distributions for Males (mm)

Measure	1th	2.5^{th}	5th	10th	25th	$\mathbf{50^{th}}$	75th	90th	95th	97.5^{th}	99th
(a)	172	176	179	182	187	**193**	200	207	210	213	219
(b)	161	165	167	170	175	**180**	187	193	196	200	203
(c)	81	82	84	85	88	**90**	93	96	97	99	100

During the detailed design process adjustments were made to the initial dimensions to accommodate the mechanisms required for actuation, the motors, fastening points etc. The measurements used initially could be re–measured from the model and compared to the anthropometric data once the design was finalised.

The final design measurements are listed in Table 2.5, which includes the percentile range they exist in for the male and female measurements. These show that the final dimensions are in the maximum range of the female measurements, and in the high range for the male measurements. This comparison gives the impression that the dimensions are far from their target, so a second comparison was made using the difference from the medians as a percentage using the formula

$$difference[\%] = (measurement - median)/median * 100 \qquad (2.3.1)$$

and is shown in Table 2.6. Differences for the a and b measurements compared to male the data remain less than 10 %, but differences of the same measurements in the female data are less than 18 %. Measurement c shows much larger differences of 64.3 % and 87.2 % for the male and female data, respectively.

Table 2.5: Percentile Ranges of 3D Design Measurements

Measurement	Value [mm]	Male Percentile Range	Female Percentile Range
(a)	209	90–95th	99–100th
(b)	197.9	95–97.5^{th}	99–100th
(c)	147.9	99–100th	99–100th

Table 2.6: Percentage Difference between Final 3D Measurements and Median Data

Measurement	Value [mm]	Male Difference (%)	Female Difference (%)
(a)	209	8.29	16.1
(b)	197.9	9.94	17.1
(c)	147.9	64.3	87.2

2.3.6.3   Palm

The palm was split into two parts, namely the back/top cover and the front/base, as can be seen in Figure 2.28. The top cover fits over the base, and is used to protect internal components as well as maintain an anthropomorphic aesthetic appeal. Space has been provided between the palm base and the cover to hold a custom electronics board. The cover is located into place by grooves along the outer edges. There are three fastening points for M3 screws, and positions for nuts to be placed for tight fits.

2.3.6.4   Fingers

A close–up top view of the small finger is presented in Figure 2.29. Parts of the pulley mechanism are labelled. The cable linkage design in the fingers proximal, middle, and distal parts required a number of cable guides and connection points, of which only a few can be seen in the image. Connections are placed within these components too, which all have hollow interiors. Most of these connections are made by creating a knot at one side of the cable, with the other end having a crimped metal ferrule.

2.3.6.5   Thumb

To allow a motor to be housed within the thumb, the end–cap had to be designed to be easily fastened or removed for maintenance purposes. An intricate configuration of dimples and grooves was conceptualised so that the cap could first be pushed on, then twisted and snapped into place. The process can be reversed to remove the cap. An alternative tested
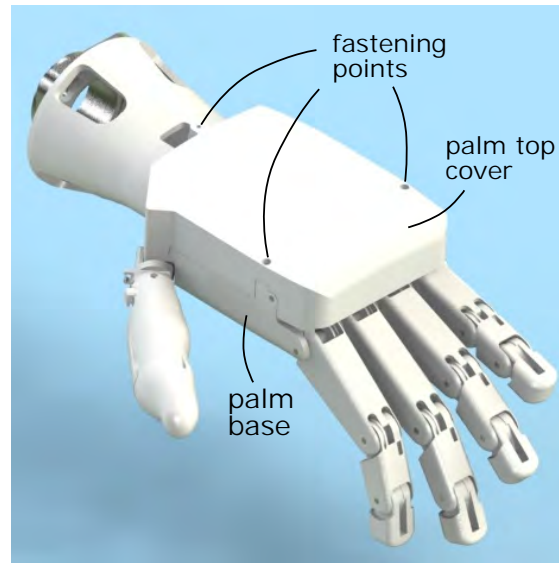
Figure 2.28: Detailed 3D Hand Design (with cover)
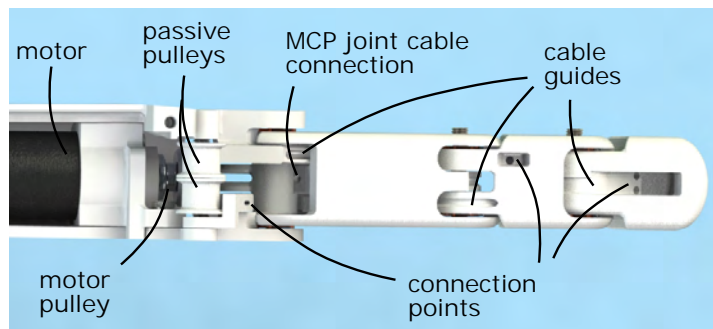
Figure 2.29: Top View of Small Finger

design was one that only required the cap to be pushed on or pulled off. This design used flaps at the edges that would hook onto dimples, but this proved to damage the plastic flaps quite easily.

2.3.6.6 Joint Design

A total of 18 joints, enabling 18 DOF, are present in the fingers and thumb. These joints needed to be strong and promote smooth rotations with minimal friction. A standard design was made for all the joints. Figure 2.30 shows a cross–sectional view of one of the finger DIP joints.

The joint consists of a stainless steel threaded rod, a brass bush, and two brass washers. The rod acts as the joint pin and the thread self–taps itself into the walls of the middle phalangeal to fix itself into position. Only a small protruding length on one end is required to grip the rod with pliers for removal. Its material avoids corrosion problems, and keeps the joint stiff.

A bush fits tightly into a hole through the distal phalangeal, and has an internal diametre

larger than the outer diametre of the rod. The brass bush can then easily rotate on the rod due to clearances and the low frictional properties of brass.

Brass washers are placed between the distal phalangeal and middle phalangeal surfaces. This helps with spacing parts to avoid large surface area contact and friction. They are made from brass to minimise friction. Since the brass washers have better strength properties than the plastic, they help support the parts.
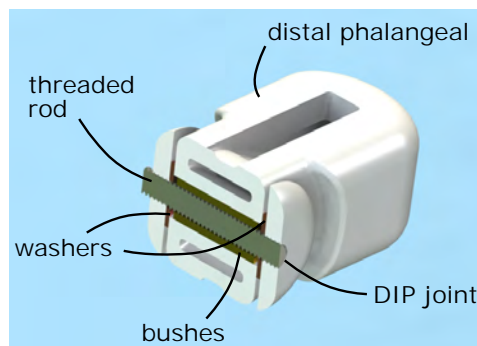
Figure 2.30: Sectional 3D View of Finger DIP Joint

2.3.6.7   Motors

During the motor selection process, it was found that the net radial force exerted by the pulley cables on the motor shaft was larger than the ratings of the shaft bearings. To minimise the radial force on the shaft, bushes were placed over the section closest to the internal bearings to act as an additional bearing support.
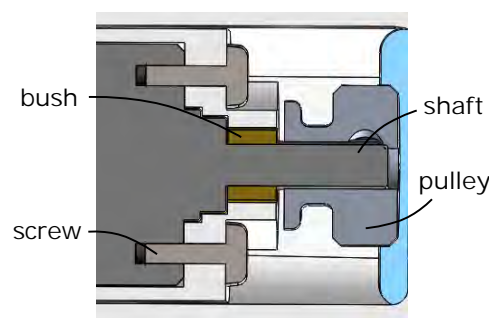
Figure 2.31: Sectional 3D View of Finger Motor

2.3.6.8   Wrist

The wrist used in the design was made to fit a specific socket of a amputee. An actuated version was considered to be future work, since this wrist created a static connection. Slots were present to allow for manual wrist rotation up to approximately 90° before fastening.

2.3.6.9   Left and Right Hand Design

The detailed design of the hand was initially completed for the left hand. To create a right hand version, parts were mirror across specific planes; all parts except some of the thumb and fingers. It was not necessary to assemble a complete 3–D right hand model because it would just be a mirrored version. Some of the parts were assembled in 3–D for the right hand only to check that the same electronics board design would fit in both versions. This was verified by printing and creating a physical right hand assembly.

2.3.7   Load Cases

The first step toward selecting motors that not only fit in the hand, but also give it sufficient strength and speeds, is to consider the worst case load conditions. The first case assumes a maximum strength condition, while the second is for the maximum speed.

2.3.7.1   Load Case 1 — Hook Grip

The hook grip loading case of Figure 2.32 was considered to find the maximum continuous and intermittent torques required by the motors. The continuous torque can be applied constantly over time whereas the intermittent torque can only be applied of a short period of time to avoid overheating (Faulhaber, 2015).

Figure 2.32: Hook Grip Loading

It was assumed that a strap or handle would be held across all four fingers and that it would create a load, W_h, over the fingers, with each finger holding the same load, $\frac{W_h}{4}$. Knowing the continuous and intermittent mass loads, the associated loads on each finger were determined by

$$W_{h\_f\_cont} = \frac{W_{h\_cont}}{4} = \frac{S_L M_{h\_cont} g}{4} \tag{2.3.2}$$

$$W_{h\_f\_int} = \frac{W_{h\_int}}{4} = \frac{S_L M_{h\_int} g}{4} \tag{2.3.3}$$

where,

$W_{h\_f\_cont}, W_{h\_f\_int}$ = finger continuous and intermittent loads in hook grasp [N]

W_{h_cont}, W_{h_int} = hand hook grasp continuous and intermittent loads [N]

M_{h_cont}, M_{h_int} = hand hook grasp continuous and intermittent mass loads [kg]

g = gravitational acceleration [m/s^2]

S_L = load safety factor

Gravitational forces on the fingers due to their own masses were neglected. The load on each finger was assumed to act at the same perpendicular distance $l_{p\_s\_mid}$ from the MCP joint. This was taken as half the joint–to–joint distance of the small proximal phalangeal. The torque on each motor–gearbox combination was then determined by dividing the MCP joint torque by the pulley ratio between the MCP joint and the motor pulley. The associated speeds would be zero as the fingers are stationary. Using the specified load masses listed in the specifications of Table 1.2, the motor–gearbox requirements for this case were determined and are listed in Table 2.7. The safety factor was used to accommodate for frictional losses not taken into account.

Table 2.7: Load Case 1 Requirements

Variable	Description	Value
S_L	safety factor	2.5
M_{h_cont} [kg]	hand hook grasp continuous mass load	3.4
M_{h_int} [kg]	hand hook grasp intermittent mass load	4.6
$T_{g\_out\_max\_cont\_1}$ [mN.m]	gearbox maximum continuous output torque for load case 1	150
$T_{g\_out\_max\_int\_1}$ [mN.m]	gearbox maximum intermittent output torque for load case 1	203
$\omega_{g\_out\_max\_1}$ [rpm]	gearbox maximum output speed	0.0

2.3.7.2 Load Case 2 — Closing Finger

The action of closing a finger of the hand without any external loads, as illustrated in Figure 2.33, has an associated MCP joint torque profile due to gravitational, frictional,

mass and inertia loads. Mass and inertia loads are a result of translational and rotational accelerations, and are dependent on the motion profile of the MCP joint. The applied MCP joint motion profile was modelled to assist with minimising the closing time and the required driving torques. The corresponding torque profile was generated to check the associated peak torques.
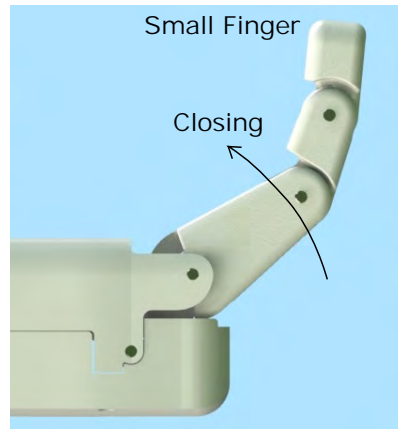
Figure 2.33: Closing Finger

The speed motion profile was based on a trapezoidal shape shown in Figure 2.34. The joint accelerates at a constant value during the start time, t_s, when it then reaches its maximum rotational speed, ω_{MCP}. This speed is maintained during the middle time, t_{mid}, before decelerating at a constant value during the end time, t_{end}. For simplification, the acceleration and decceleration values were made equal by making the start and end times equal.

The acceleration and decceleration values are inversely proportional to the length of time they exist. Higher accelerations would mean higher torque requirements of the motor–gearbox combination. On the contrary, shorter acceleration times would reduce the overall closing time. Iterations were performed to make the required torque values close to the rated contiuous values in order to balance the trade–offs. Continuous rated torque was a safer reference as it could be applied for any length of time without heating problems, which is not true for the intermittent torques. The final profile data are listed in Table 2.8.

The torque profile required a combination of kinematic and force dynamic calculations, and depended directly on the motion profile. To handle this complex computation, a multi–body dynamic simulation was created using MSc Adams. The model of the hand was exported from Solidworks into MScAdams. The wire linkage system was added into each of the fingers using default parameters, which included zero pre–tension on the cables and zero cable mass. Each part of the finger was assigned a material property as close to the final design as possible. Frictional loads were incorporated by using the Coulomb friction model and estimated static and dynamic friction coefficients. Gravity was added
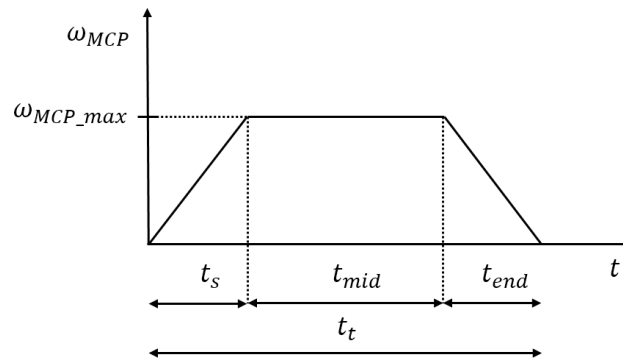
Figure 2.34: Closing Motion Profile of MCP Joint

Table 2.8: Final Motion Profile Data

Variable	Description	Value
t_s [s]	start time of finger closing cycle	0.0360
t_{mid} [s]	middle time of finger closing cycle	0.928
t_{end} [s]	end time of finger closing cycle	0.0360
t_t [s]	maximum time of finger closing cycle	1.00
θ_{MCP} [rad]	metacarpal–phalangeal joint angle	$\pi/2$

to the simulation with it acting downward onto the bottom palm face. Finally, the joint motion profile was programmed into the simulation. The results of the simulation are shown in Figure 2.35 for a closing and opening motion profile, which is why it ran for 2.0 s and not 1.0 s.
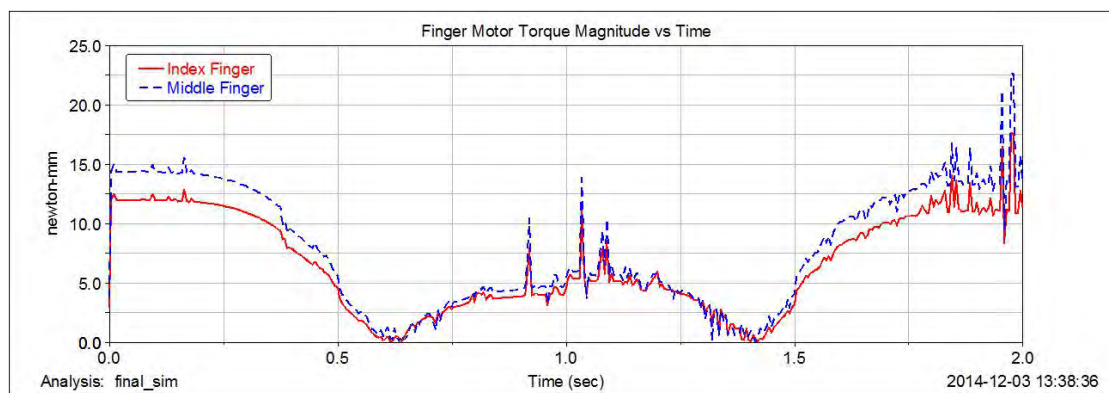
Figure 2.35: Simulated MCP Joint Torque Profiles for a Close and Open Sequence

Two of the largest fingers are considered, the middle and index fingers, because they will have the largest torques. The middle finger profile is clearly larger over time. Throughout

the simulation there are torque spikes, which are generated by the friction model and last for fractions of a second. High torques are present at the start, accelerating the finger against gravity. The torque rapidly decreases as the centre of gravity of the finger moves over the joint. At approximately 0.62 s the torque changes sign. Only the torque magnitude is considered here for comparison purposes and so the sign stays positive. The largest steady torque value was taken from the start of the simulation. The resulting load case requirements are listed in Table 2.9.

Table 2.9: Load Case 2 Requirements

Variable	Description	Value
$T_{g\_out\_max\_2}$ [mN.m]	gearbox maximum output torque for load case 2	9.37
$\omega_{g\_out\_max\_2}$ [rpm]	gearbox maximum output speed for load case 2	30.4

2.3.8   Finite Element Analysis

A finite element analysis (FEA) was performed on the most critical parts to check for possible load failures. If so the design was adjusted to be able to handle the estimated maximum loads. The load case with the highest load is load case 1 in section 2.3.7.1 with a total static hook weight load, W_h, of 112.8 N; taking the load safety factor into consideration. This value was used as a reference when applying loads to critical parts. The yield strength of ABS plastic was not available in the Solidworks material library, but the ultimate tensile strength was. This value, 30 MPa, was assumed as the yield strength for factor of safety calculations. Safety factors of at least 1.5 were accepted. Applied loads are represented by pink arrows, and fixed points are represented by green arrows.

During the hook load, the bottom palm section would take all the load. The internal shape was inspired by the arrangement of bones in the hand. This produced the multiple ribs that separate the motors. The shape of each rib contributes greatly to the second moment area for the hook load case, improving the stiffness, and stress resistance.

For the FEA on the bottom palm part, shown in Figure 2.36, the wrist face was assumed to be fixed, while the load W_h was evenly distributed between each MCP joint connection point. A maximum stress of 17.5 MPa was computed, given a factor of safety equal to 1.7. Figure 2.37 shows the FEA of the middle finger proximal phalangeal. Here it is assumed the worst case condition would be the load $W_h/4$ distributed across the indicated face. A maximum stress of 6.41 MPa gives a factor of safety of 4.68.

The middle and distal phalangeals do not experience any direct load in the considered load case 1. They were assumed to have a maximum load of 49.0 N (5 kg). This was applied at the DIP joint for the middle phalangeal, shown in Figure 2.38, and on the indicated face
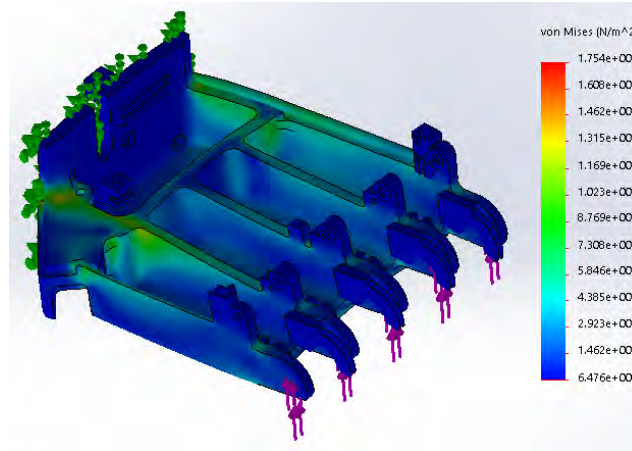
Figure 2.36: Finite Element Analysis of Palm
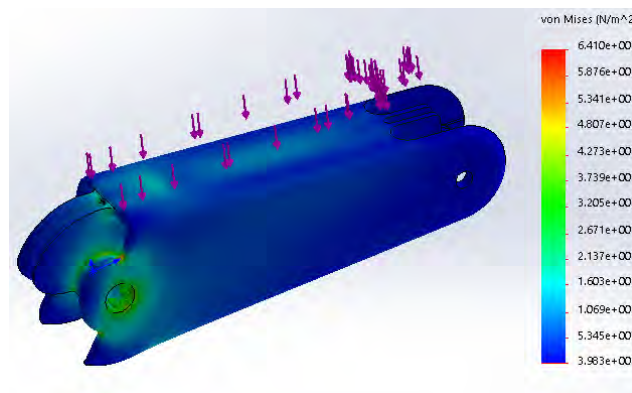
Figure 2.37: Finite Element Analysis of the Middle Finger Proximal Phalangeal

of the distal phalangeal in Figure 2.39. Stresses of 19.3 MPa and 9.67 MPa were computed for the middle and distal phalangeals, corresponding to factors of safety equal to 1.55 and 3.1, respectively.
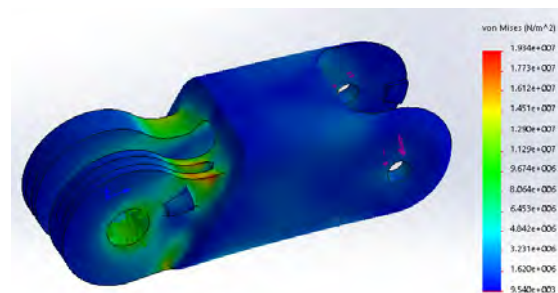
Figure 2.38: Finite Element Analysis of the Middle Finger Middle Phalanx
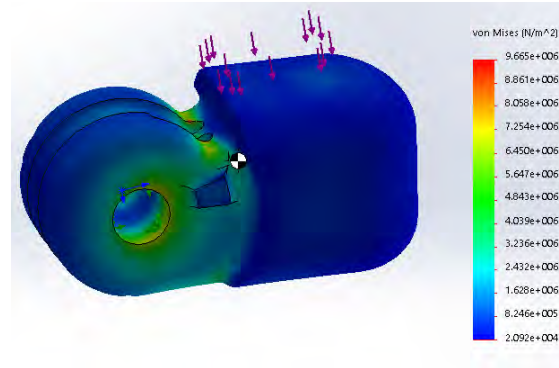
Figure 2.39: Finite Element Analysis of the Distal Phalanx

2.3.9 Physical Assembly

Once the final dimensions of the design were completed, parts were printed and assembled together to physically verify the operation of the fingers and the types of fits. Although the design was based from a left hand model, a right–hand version, shown in Figure 2.40, was made by printing out the mirrored parts. The selected motors are included to show how they fit, however the motor selection process is discussed later in section 3.2. The prosthetic hand was also attached to an amputee's socket, who tested it. This is discussed later in the testing chapter.

(a)   (b)
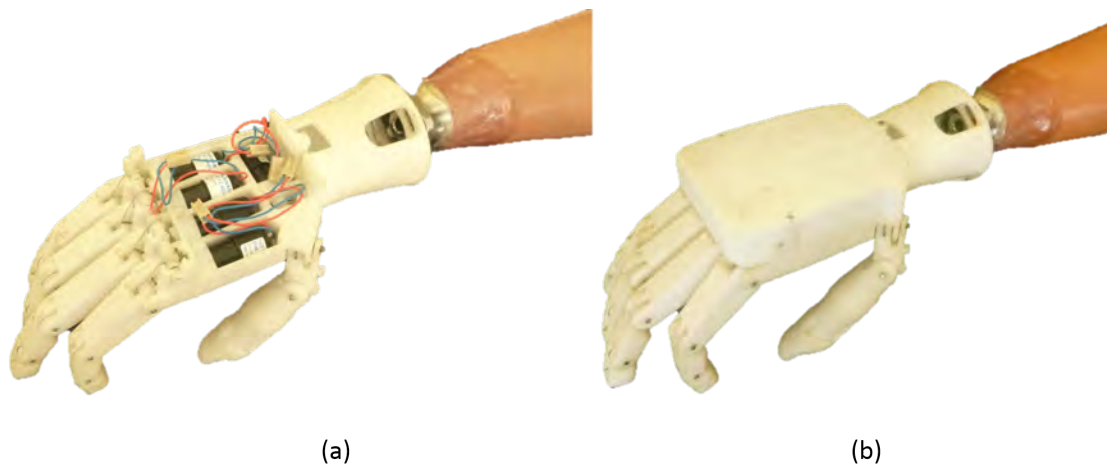
Figure 2.40: Constructed Hand: (a) without top cover or electronics, (b) with top cover, but without electronics

In some cases part dimensions had to change to acquire the correct fits because the orientation of the parts during 3D printing would affect the dimensional resolution. The printers horizontal layer resolution was better than the vertical resolution. Where necessary, part dimensions were filed down to achieve tighter tolerances, such as on some of the finger joints.

2.3.10 Kinematics

Kinematic models of the fingers and thumb were derived to generate motion analyses and allow future model comparisons. The Denavit–Hartenberg (DH) notation was used to determine the joint and link parameters, which then led to the determination of the DH transformation matrices, one for each link. These matrices were used to determine the position of each link in 3–D space for specific joint angles.

2.3.10.1 Denavit–Hartenberg Tables

Denavit–Hartenberg notation characterises the position and orientation of each robots link, i, into link and joint parameters. These include the link length, a_i, link twist, α_i, joint distance, d_i, and joint angle, θ_i, for each link (Jazar, 2010). The parameters are then summarised for all n links, as shown in Table 2.10.

Table 2.10: General Denavit–Hartenberg Table

Frame No.	a_i	α_i	d_i	θ_i
1	a_1	α_1	d_1	θ_1
2	a_2	α_2	d_2	θ_2
3	a_3	α_3	d_3	θ_3
...	...	...	...	...
n	a_n	α_n	d_n	θ_n

The DH parameters for the fingers were determined by considering the defined coordinate systems, lengths and angles in Figure 2.41. The base frame is defined by x_0 and y_0. The resulting DH parameters are summarised in Table 2.11.

Table 2.11: Finger Denavit–Hartenberg Table

Frame No.	a_i	α_i	d_i	θ_i
1	l_1	0	0	θ_1
2	l_2	0	0	θ_2
3	l_3	0	0	θ_3
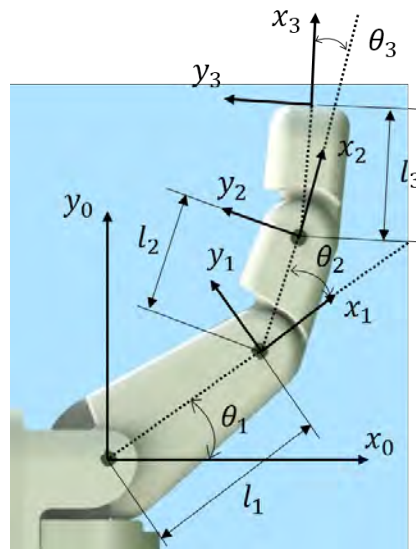
Figure 2.41: Coordinate Frames of Finger

The DH parameters for the thumb were determined by considering the defined coordinate systems, lengths and angles in Figure 2.42. The base frame is defined by x_0 and z_0. The resulting DH parameters are summarised in Table 2.12.
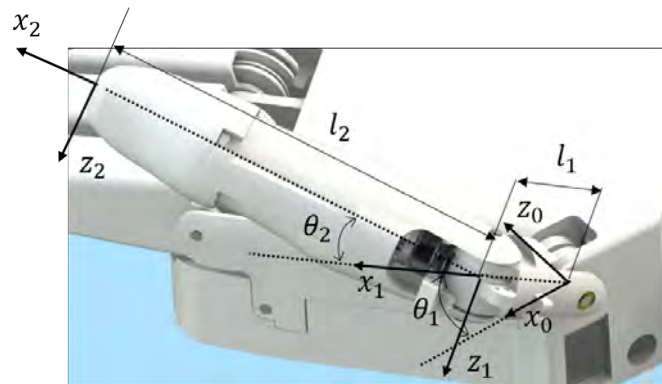
Figure 2.42: Coordinate Frames of Thumb

Table 2.12: Thumb Denavit–Hartenberg Table

Frame No.	a_i	α_i	d_i	θ_i
1	l_1	$\pi/2$	0	θ_1
2	l_2	0	0	θ_2

2.3.10.2   Transformation Matrices

Transformation matrices are used to transform a coordinate frame of a link, i, to the coordinate frame of an adjacent link, $i - 1$. The general transformation matrix for this, based on DH notation, is (Jazar, 2010)

$$A_{i-1,i} = \begin{bmatrix} \cos\theta_i & -\sin\theta_i\cos\alpha_i & \sin\theta_i\sin\alpha_i & a_i\cos\theta_i \\ \sin\theta_i & \cos\theta_i\cos\alpha_i & -\cos\theta_i\sin\alpha_i & a_i\sin\theta_i \\ 0 & \sin\alpha_i & \cos\alpha_i & d_i \\ 0 & 0 & 0 & 1 \end{bmatrix} \tag{2.3.4}$$

Substituting parameters $\alpha_i, d_i = 0$ of Table 2.11 into Equation (2.3.4) gives the transformation matrix to be used between the coordinate frames within each finger.

$$A_{i-1,i} = \begin{bmatrix} \cos\theta_i & -\sin\theta_i & 0 & l_i\cos\theta_i \\ \sin\theta_i & \cos\theta_i & 0 & l_i\sin\theta_i \\ 0 & 0 & 1 & 0 \\ 0 & 0 & 0 & 1 \end{bmatrix} \tag{2.3.5}$$

Therefore, substituting all the parameters for each link of Table 2.11 into Equation (2.3.5), the transformation equations between each of the coordinate frames of Figure 2.41 are determined as follows:

$$A_{2,3} = \begin{bmatrix} \cos\theta_3 & -\sin\theta_3 & 0 & l_3\cos\theta_3 \\ \sin\theta_3 & \cos\theta_3 & 0 & l_3\sin\theta_3 \\ 0 & 0 & 1 & 0 \\ 0 & 0 & 0 & 1 \end{bmatrix} \tag{2.3.6}$$

$$A_{1,2} = \begin{bmatrix} \cos\theta_2 & -\sin\theta_2 & 0 & l_2\cos\theta_2 \\ \sin\theta_2 & \cos\theta_2 & 0 & l_2\sin\theta_2 \\ 0 & 0 & 1 & 0 \\ 0 & 0 & 0 & 1 \end{bmatrix} \tag{2.3.7}$$

$$A_{0,1} = \begin{bmatrix} \cos\theta_1 & -\sin\theta_1 & 0 & l_1\cos\theta_1 \\ \sin\theta_1 & \cos\theta_1 & 0 & l_1\sin\theta_1 \\ 0 & 0 & 1 & 0 \\ 0 & 0 & 0 & 1 \end{bmatrix} \tag{2.3.8}$$

For the thumb, the values of Table 2.12 were substituted into Equation (2.3.5) to give:

$$A_{1,2} = \begin{bmatrix} \cos\theta_2 & -\sin\theta_2 & 0 & l_2\cos\theta_2 \\ \sin\theta_2 & \cos\theta_2 & 0 & l_2\sin\theta_2 \\ 0 & 0 & 1 & 0 \\ 0 & 0 & 0 & 1 \end{bmatrix} \tag{2.3.9}$$

$$A_{0,1} = \begin{bmatrix} \cos\theta_1 & 0 & \sin\theta_1 & l_1\cos\theta_1 \\ \sin\theta_1 & 0 & -\cos\theta_1 & l_1\sin\theta_1 \\ 0 & 1 & 0 & 0 \\ 0 & 0 & 0 & 1 \end{bmatrix} \tag{2.3.10}$$

2.3.10.3   Motion Profiles

Motion profiles were generated for the fingers and the thumb by plotting link positions for corresponding joint angles. For the fingers, the first joint angle was increment between the full range of motion, from 0° to 110°. The second and third joint angles depended directly on the first joint angle because of the cable linkage design. These relationships use the virtual pulley diametres at each joint, as follows:

$$\theta_2 = \frac{d_{p1}}{d_{p2}^o}\theta_1 \tag{2.3.11}$$

$$\theta_3 = \frac{d_{p2}^i}{d_{p3}}\theta_1 \tag{2.3.12}$$

where,

$\theta_1, \theta_2, \theta_3 =$ first, second and third joint angles [rad]

$d_{p1} =$ virtual pulley diameter at MCP joint [m]

$d_{p2}^o, d_{p2}^i =$ outer and inner virtual pulley diameters at the PIP joint [m]

$d_{p3} =$ virtual pulley diameter at DIP joint [m]

Equation (2.3.11) was used with Equation (2.3.7), and Equation (2.3.12) was used with Equation (2.3.6) to find the second and third finger link positions, respectively, for the corresponding first joint angle. The latter angle used with Equation (2.3.8) was used to determine the first link position.

The graph of Figure 2.43 shows a 2–D plot of each finger motion for the changing first joint angle. An angle difference of 2° was used between the first joint angle of each finger to avoid overlapping. The small and middle fingers are represented by black and red, respectively, while the ring and index fingers are represented by blue.
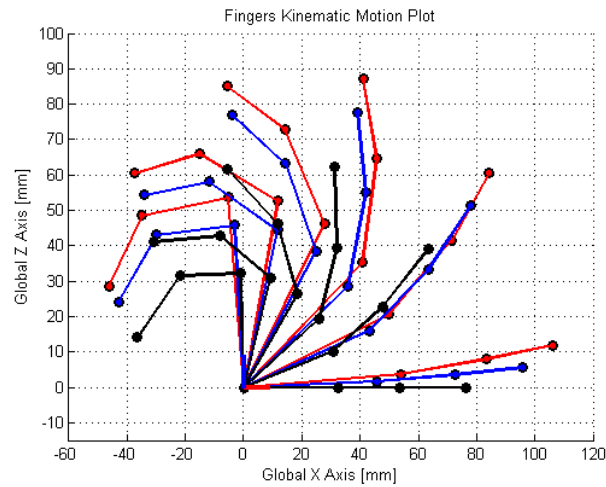
Figure 2.43: 2–D Fingers Kinematic Motion Profiles

The plot of Figure 2.44 gives a 3–D perspective of the fingers kinematic motion with the same incremented first joint angle. Here the small, ring, middle and index finger are represented by black, blue, red and green, respectively.
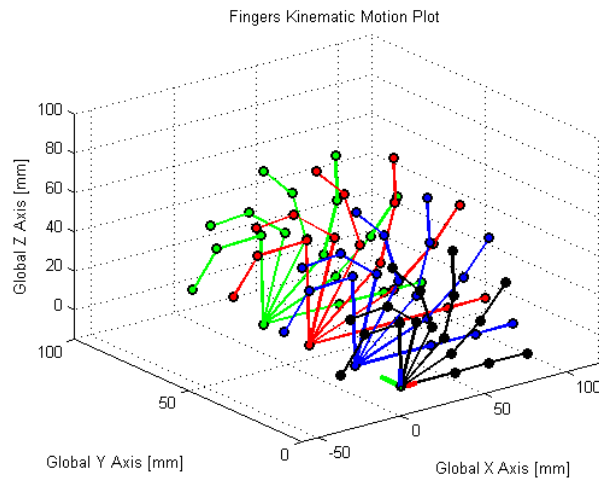
Figure 2.44: 3–D Fingers Kinematic Motion Profiles

For the thumb, the first joint angle and the second joint angle are independent. These angles were incremented throughout their range of motion, 0° to 90°. This motion is more visually understandable in 3–D, as shown in Figure 2.45. For each incremented angle θ_1 the angle θ_2 was incremented throughout its motion range. Each colour represents a different θ_1 value.
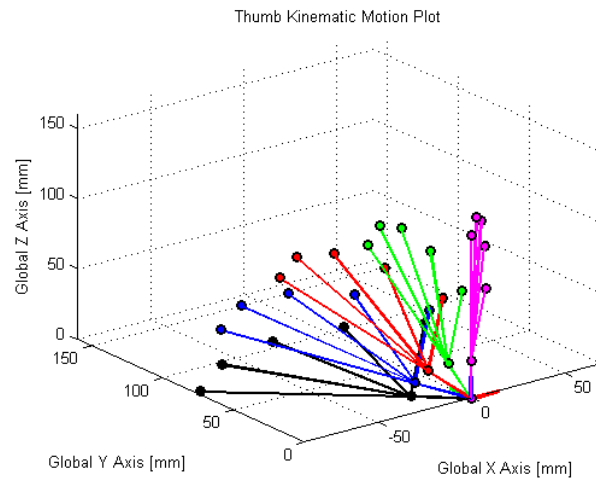
Figure 2.45: 3–D Thumb Kinematic Motion Profile

2.4 CHAPTER SUMMARY

The biological complexity of the human hand does not only include the physical bones, tendons and muscles, but also how they work together to create motion. A grasp taxonomy was considered in an attempt to simplify the most common and useful grasps that could be performed by a prosthetic hand.

Previous designs made by researchers were evaluated to extract information on the mechanisms and actuators used for prosthetic fingers. The prominent pros and cons of metallic, plastic, and composite materials were considered.

The mechanical design required a thorough concept selection for the fingers, actuation mechanism, palm shape, and thumb. Further intricated details of the final dimensions and mechanicsl components were 3–D modelled and completed. Load cases were modeled to estimated the maximum torques and speeds required by the motors. These loads were used to ensure the structure did not fail by doing an FEA analysis. Finally the hand was 3–D printed and assembled with the motors and cabling. The motion profile of all links in the hand was simulated using a kinematic model. mechanical design

3   ELECTRONICS

The electronics were divided into two main subsystems, as shown in Figure 3.1, labelled external and embedded. The figure shows the command and feedback flow paths within and between the sub–systems, with the initial commands applied by an amputee. The scope of the electronic design encompassed the embedded subsystem, but general comments are made about each sub–system before discussing related literature and the detailed design.
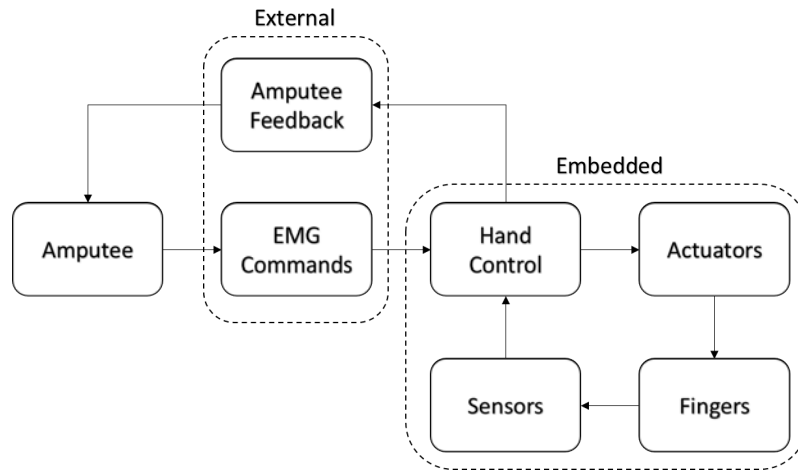
Figure 3.1: Functional Overview of the Hand with an Amputee

If an amputee is to use the hand, the external electronics will be housed within the custom prosthetic socket. Electromyography (EMG) signals are measured from the surface of the amputee's skin over selected muscle groups using padded electrodes (van der Riet, 2014). These are filtered and amplified before being transferred to the hand control function block.

The embedded electronics will already be fixed into the hand. Depending on the EMG commands, the hand control function block will change the state of the fingers via the actuators and verify the changes with sensors. Sensed values will determine the required feedback to the amputee, possibly altering the intensity and frequency of the stimulation. Types of tactile stimulations could be pressure, vibration and NMES (van der Riet, 2014). A vibrotactile method was used in the first Touch Hand (van der Riet, 2014).

The electronic detailed design only included the embedded subsystem previously mentioned, and shown in Figure 3.1. This section presents the concepts, comparisons, and

selections made for the components and circuits of the sub–system. A custom electronics board was made that sat in the palm of the hand, over the motors and covered by the top half of the palm.

3.1 Hardware Architecture

The architecture of the embedded electronics is represented in Figure 3.2. Hand control is achieved with a microcontroller (MCU), motor h–bridges, and a power supply. The actuators are made up of the motors for the fingers. Torque, speed and position measurements are supplied as feedback to the MCU. The finger function block has been removed in the diagram because measurements were made directly from the motors and processed to estimate the finger states.
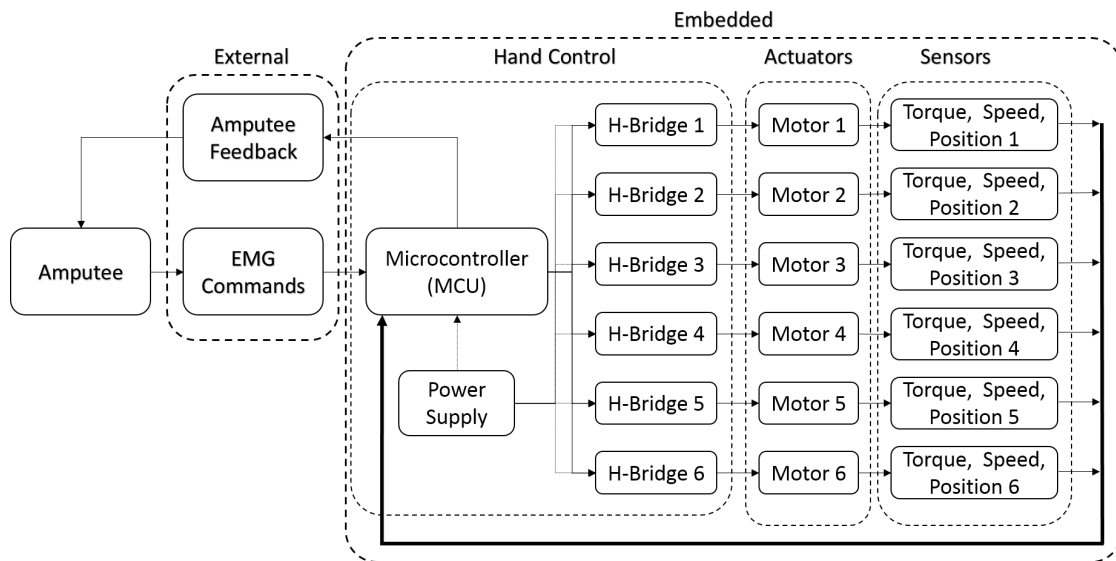
Figure 3.2: Functional Diagram of the Embedded Hand Electronics

The MCU performs all the logic calculations and makes programmed decisions based on the EMG commands and sensor data. The h–bridges are used to output a specific average voltage by switching the peak voltage over the motor terminals on and off at a defined frequency and duty cycle. These properties are controlled by a pulse–width–modulation (PWM) signal from the MCU to the h–bridge enable pin. The frequency changes the period of a voltage switching cycle, whereas the duty cycle changes the average voltage.

The peak applied motor voltage is determined by the voltage provided by the power supply. Batteries are used as the power source, but their voltage level changes over time. For better motor voltage control, the battery voltage is monitored.

The torque of the motors are estimated by first measuring the current, followed by a substitution into Equation (3.2.5). Two methods of position and speed measurement were considered and compared in more detail, and are described in section 3.6. One option uses

the back–emf of the motor, while the other monitors the resistance of a flex sensor placed in a finger.

An important aspect of this architecture is that either the external or embedded electronics can be modified independently. Upgrades/additions, for example with more sensors, would require a separate attachable circuit onto this design. This would be represented by an additional functional block within the embedded sub–system.

3.2   Motor Selection

Motors were selected as the best actuation method for reasons previously described in section 2.2.2. The selected motors would directly affect the allowable grip force and closing speed of the fingers. If the motors did not produce the desired torque and speed requirements, then the hands functionality would be less desirable. An amputee would not have much use for a hand that did not perform to a desired functional level. For these reasons a detailed motor selection process was carried out.

To simplify the selection process and for standardisation purposes, the same motor model was selected to drive each of the actuated joints. The principal operation of brushed dc motors are first described, followed by their useful equations. Specific load cases were considered that would simulate the motors in worst case conditions. The required torques and speeds extracted from these cases were then mathematically manipulated to give values that could be compared to the data of possible motors. Three motors were evaluated and compared against one another.

3.2.1   Brushed DC Motor Theory

The principal operation of a brushed dc motor is the motion of looped wired in a permanent magnetic field; the current flowing through it induces a force against it when a voltage is applied across its ends (Chapman, 2005). Figure 3.3 shows a sectional view of a brushed dc motor perpendicular to the shaft axis (front view) (Helms, 2011). A permanent magnetic field is produced by the north (N) and south (S) poles fixed to the stator (case), with the field directed from north to south. A rotor (also known as an armature) rotates on an axis in–between the permanent magnets with windings or wire. The windings are connected to a commutator which is in contact with a pair of brushes. This is used to synchronise the directional change of the current so that the torque on the rotor remains in one direction (Chapman, 2005).

Figure 3.4 shows a sectional view of a motor from the side (2 Brothers Hobby, LLC, n.d.). Shaft bearings are commonly placed at the ends of the motor shaft within the casing. The image shows how the armature is a part of the shaft and how the terminals are connected directly to the brushes.

An equivalent electrical circuit of a brushed dc motor is illustrated in Figure 3.5 (Chapman, 2005). It consists of an internal resistance ,R_m, inductance ,L_m, and back–emf ,v_{emf}. The
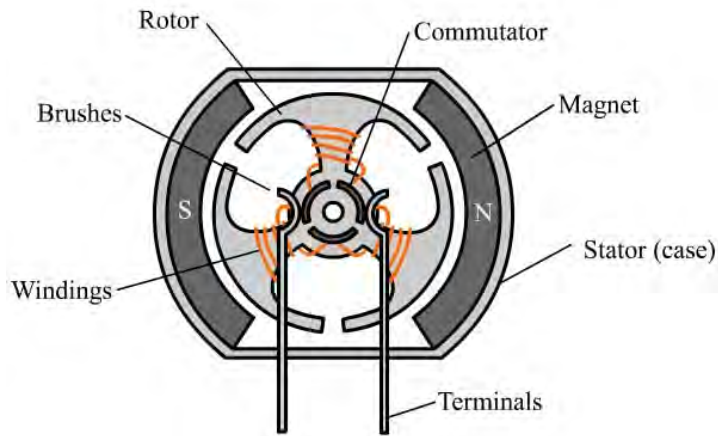
Figure 3.3: Brushed DC Motor Sectional Front View
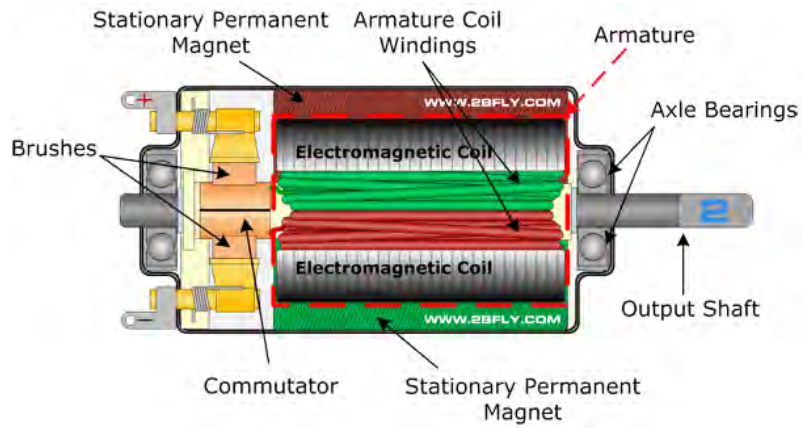
Figure 3.4: Brushed DC Motor Sectional Side View

equations described next use this circuit as a reference, and were used to find important characteristics of the motor behaviour under various voltages, speeds and loads.
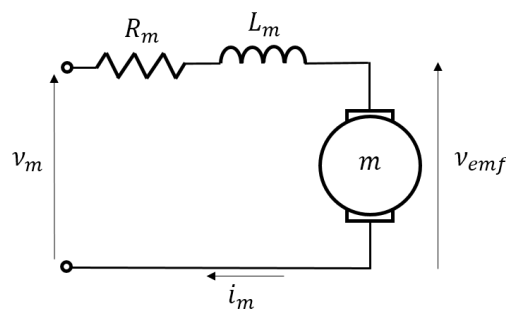
Figure 3.5: Brushed DC Motor Equivalent Circuit

Considering the transient voltages of the circuit and using Kirchoff's Voltage Law, the terminal voltage is:

$$v_m = i_m R_m + L_m \frac{di_m}{dt} + v_{emf} \tag{3.2.1}$$

where,

v_m = transient motor terminal voltage [V]

i_m = transient motor current [A]

R_m = internal motor resistance [Ω]

L_m = internal motor inductance [H]

v_{emf} = transient motor back–emf [V]

The magnetic flux can be used to define the motor constant as:

$$K_m = K\phi \tag{3.2.2}$$

where,

K_m = motor constant [N.m/A or V/rad.s^{-1}]

K = motor flux constant [N.m/A.Wb]

ϕ = motor magnetic flux [Wb]

The back–emf voltage is proportional to the rotor speed through the equation:

$$v_{emf} = K_m \omega_m \tag{3.2.3}$$

where,

v_{emf} = motor back–emf voltage [V]

ω_m = motor rotational speed [rad/s]

The torque generated on the shaft is proportional to the motor current through the relationship:

$$T_m = K_m i_m \tag{3.2.4}$$

where,

T_m = motor torque [N.m]

With no external load on the output shaft the motor will draw a no load current due to friction. Externally applied torque then follows the equation:

$$T_{m\_load} = K_m(i_m - I_o) \tag{3.2.5}$$

where,

T_{m_load} = motor load torque [N.m]

I_o = motor steady–state no load current [A]

During steady state $L_m \frac{di_m}{dt} = 0$ and Equation (3.2.1) reduces to:

$$v_m = i_m R_m + v_{emf} \tag{3.2.6}$$

Substituting Equation (3.2.4) and (3.2.3) into Equation (3.2.6) and rearranging, to show the steady–state relationship between the motor torque and speed, gives the motor characteristic equation as:

$$\omega_m = \frac{V_m}{K_m} - \frac{T_m}{K_m^2} R_m \tag{3.2.7}$$

where,

V_m = motor steady–state terminal voltage [V]

The electrical input power to the motor is given by:

$$P_e = V_m I_m \tag{3.2.8}$$

where,

P_e = motor electrical input power [W]

I_m = motor steady–state current [A]

Electrical heat losses are given by:

$$P_{loss\_elect} = I_m^2 R_m \tag{3.2.9}$$

where,

P_{loss_elect} = motor electrical power losses [W]

The mechanical power produced by the motor is given by:

$$P_m = T_m \omega_m \tag{3.2.10}$$

where,

$$P_m = \text{motor mechanical power [W]}$$

Mechanical losses are due to friction and can be determined using the no–load current by:

$$P_{loss\_mech} = K_m I_o \omega_m \tag{3.2.11}$$

where,

$$P_{loss\_mech} = \text{motor mechanical power losses [W]}$$

Mechanical power output after frictional losses drive the external load and can be determined by:

$$P_{m\_out} = P_m - P_{loss\_mech} = T_m \omega_m - K_m I_o \omega_m \tag{3.2.12}$$

where,

$$P_{m\_out} = \text{motor mechanical output power [W]}$$

Electrical and mechanical losses can be the combinational losses:

$$P_{loss\_comb} = P_{loss\_elect} + P_{loss\_mech} = I_m^2 R_m + K_m I_o \omega_m \tag{3.2.13}$$

where,

$$P_{loss\_comb} = \text{motor combinational power losses [W]}$$
$$P_{loss\_elect} = \text{motor electrical power losses [W]}$$
$$P_{loss\_mech} = \text{motor mechanical power losses [W]}$$

The motor efficiency can be defined as the useful mechanical output over the electrical input as:

$$\eta_m = \frac{P_m - P_{loss\_mech}}{P_e} 100 \tag{3.2.14}$$

where,

$$\eta_m = \text{motor efficiency [\%]}$$

3.2.2 Selection Criteria

Specific selection criteria were used to evaluated whether a motor–gearbox combination would satisfy the load case requirements. The selection procedure with conditional equations are described (Faulhaber, 2015). The motor was considered first, followed by the gearbox.

The first step was to calculate the required motor power using Equation (3.2.15). The rated mechanical power of possible motors for selection was then calculated using Equation (3.2.16). The motor power would need to satisfy the condition of Equation (3.2.17).

$$P_{g\_out\_max} = T_{g\_out\_max\_int} \; \omega_{g\_out\_max} \tag{3.2.15}$$

$$P_m^R = T_m^R \omega_m^R \tag{3.2.16}$$

$$1.5 \leq \frac{P_m^R}{P_{g\_out\_max}} \leq 2.5 \tag{3.2.17}$$

where,

$P_{g\_out\_max}$ = gearbox maximum mechanical output power [W]

$T_{g\_out\_max\_int}$ = gearbox maximum intermittent output torque [N.m]

$\omega_{g\_out\_max}$ = gearbox maximum output speed [rad/s]

P_m^R = motor rated mechanical power [W]

T_m^R = motor rated torque [N.m]

ω_m^R = motor rated speed [rad/s]

The width and height dimensions were then checked against the space requirements. The available voltage supply should have a nominal value greater than the rated voltage of the motor, using Equation (3.2.18).

$$V_{supply\_nom} \leq V_{m\_nom}^R \tag{3.2.18}$$

where,

V_{supply_nom} = nominal power supply voltage [V]

$V_{m\_nom}^R$ = motor rated nominal voltage [V]

The gearbox rated output torques should be higher than the required torques. This is checked using Equation (3.2.19) and (3.2.20) for the continuous and intermittent conditions, respectively.

$$T_{g\_out\_max\_cont}^{R} \geq T_{g\_out\_max\_cont} \tag{3.2.19}$$

$$T_{g\_out\_max\_int}^{R} \geq T_{g\_out\_max\_int} \tag{3.2.20}$$

where,

$T_{g\_out\_max\_cont}^{R}$ = rated gearbox maximum continuous output torque [N.m]

$T_{g\_out\_max\_cont}$ = gearbox maximum continuous output torque [N.m]

$T_{g\_out\_max\_int}^{R}$ = rated gearbox maximum intermittent output torque [N.m]

$T_{g\_out\_max\_int}$ = gearbox maximum intermittent output torque [N.m]

The gearbox speed ratio was then determined using Equation 3.2.21. The closest available gearbox ratio that satisfied the dimensional requirements was selected, represented by G_{g_select}.

$$G_g = \frac{\omega_{g\_in\_max}^{R}}{\omega_{g\_out\_max}} \tag{3.2.21}$$

where,

$\omega_{g\_in\_max}^{R}$ = rated gearbox maximum input speed [rad/s]

The maximum required gearbox input speed by the motor was then calculated, using Equation (3.2.22), and compared against the rated speed using Equation (3.2.23).

$$\omega_{g\_in\_max} = G_g \omega_{g\_out\_max} \tag{3.2.22}$$

$$\omega_{g\_in\_max}^{R} \geq \omega_{g\_in\_max} \tag{3.2.23}$$

where,

$\omega_{g\_in\_max}$ = gearbox maximum input speed [rad/s]

Considering the efficiency of the gearbox, the required torques to be produced by the motor were calculated using Equation (3.2.24) and (3.2.25).

$$T_{g\_in\_max\_cont} = \frac{T_{g\_out\_max\_cont}}{G_g \eta_g} \tag{3.2.24}$$

$$T_{g\_in\_max\_int} = \frac{T_{g\_out\_max\_int}}{G_g \eta_g} \tag{3.2.25}$$

where,

$T_{g\_in\_max\_cont}$ = gearbox maximum continuous input torque [N.m]

$T_{g\_in\_max\_int}$ = gearbox maximum intermittent input torque [N.m]

η_g = gearbox efficiency [%]

The maximum motor speed is equivalent to the maximum gearbox input speed, and the maximum motor torques are equivalent to the maximum gearbox input torques. These relationships are shown in Equation (3.2.26), (3.2.27) and (3.2.28).

$$\omega_{m\_max} = \omega_{g\_in\_max} \tag{3.2.26}$$

$$T_{m\_max} = T_{m\_int} = T_{g\_in\_max\_int} \tag{3.2.27}$$

$$T_{m\_cont} = T_{g\_in\_max\_cont} \tag{3.2.28}$$

where,

ω_{m_max} = motor maximum speed [rad/s]

T_{m_max} = motor maximum torque [N.m]

T_{m_int} = motor intermittent torque [N.m]

T_{m_cont} = motor continuous torque [N.m]

One addition made to the referred selection process was a condition on the required continuous torque. To minimise heat problems, the required continuous torque should be less than the rated continuous torque of the motor. In equation form

$$T_{m\_cont} \leq T_m^R \tag{3.2.29}$$

where,

T_m^R = rated motor torque [N.m]

Once the required torques and speeds of the motor via the gearbox were determined, further optimisation could be made to improve the motor operational life. This involved a comparison of the motors required maximum speed against the no load speed, and a comparison of the motor required maximum torque against the stall torque. These comparisons are represented in Equation (3.2.30) and (3.2.31).

$$\omega_{m\_max} \geq \frac{\omega_{m\_o}}{2} \tag{3.2.30}$$

$$T_{m\_max} \leq \frac{T_{m\_stall}}{2} \qquad (3.2.31)$$

where,

ω_{m_o} = motor no load speed [rad/s]

T_{m_stall} = motor stall torque [N.m]

If both conditions are not met then a motor with the next rated voltage up should be evaluated. If the torque condition is met but the speed condition is not, then a motor with the next lower rated voltage or with a smaller frame size should be evaluated. The radial and axial shaft loads on the gearbox should be determined to be compared against the rated bearing loads.

Additional selection factors considered were cost and weight. If a number of motor–gearbox combinations satisfied the requirements, then these were the final determining factors.

3.2.3 Motor Performance Requirements

Combining the requirements of each of the loading cases in section 2.3.7.2 and 2.3.7.1 and additional requirements discussed in section 3.2.2, a final list of motor requirements was made and listed in Table 3.1. The listed values use the maximum conditions from each case to ensure a successful selection. The supply voltage is estimated by assuming a battery voltage slightly larger than 6 V, for a 5 V circuit supply regulation, that can be controlled by pulse–width–modulation for nominal voltage control below 6 V.

Table 3.1: Overall Motor Requirements

Variable	Value
$T_{g\_out\_max\_cont}$ [mN.m]	150
$T_{g\_out\_max\_int}$ [mN.m]	203
$\omega_{g\_out\_max}$ [rpm]	30.4
$P_{g\_out\_max}$ [W]	0.646
V_{supply_nom} [V]	6.0
maximum dimensions [mm]	18.0 x 18.0 x 53.0

3.2.4 Motor Comparisons and Selection

The motors were the most critical components for mechanical performance. Motor–gearhead combination options from two high quality brands were evaluated; namely, Faulhaber and

Maxon. Load requirements were placed into the online drive selection programs to acquire possible combinations. Calculations were performed on the data of each combination (see appendix A) to ensure they satisfied the criteria previously described in section 3.2.2, using the motor requirements of Table 3.1 listed in the mechanics chapter. The results of the calculations can be found in Table 3.2, 3.3 and 3.4, showing the available data, calculated values and conditions, respectively. The titled combinations consist of specific motor and gearhead models as follows:

1. Combination 1: Faulhaber motor 1717_SR & gearhead 15A (152:1).

2. Combination 2: Faulhaber motor 1016M006G & gearhead 10/1 (1024:1).

3. Combination 3: Maxon motor A–max 16EB & gearhead GP 16 A (128:1).

Table 3.2: Motor–Gearbox Combinations Data

Variable	Combination 1	Combination 2	Combination 3
Cost per unit[1] [\$]	77.96	185.74	139.56
T_m^R [mN.m]	2.1	0.48	2.22
ω_m^R [rpm]	6540	5730	4530
$V_{m\_nom}^R$ [V]	6.0	6.0	6.0
$T_{g\_out\_max\_cont}^R$ [mN.m]	150	100	200
$T_{g\_out\_max\_int}^R$ [mN.m]	300	200	300
$\omega_{g\_in\_max}^R$ [rpm]	5000	5000	8000
η_g [%]	67	55	73
ω_{m_o} [rpm]	14000	18400	10100
T_{m_stall} [mN.m]	5.34	0.9	4.03
max. dimensions [mm]	17.0 x 17.0 x 50.9	10 x 10 x 45.1	16.0 x 16.0 x 59.85
$Mass$ [g]	24	17.5	48

1. Costs are estimates based on quotations and tax in South Africa

Comparing the satisfied conditions in Table 3.4, combination 1 satisfies all conditions except that of Equation (3.2.30). This condition is for lifetime optimisation, which means the combination will not operate as long as if the condition was satisfied. Additionally, the selected combination has the lowest cost.

Due to the cable–linkage system, the radial load on the gearbox shaft is equivalent to the cable tension. The maximum value of which is 81.2 N. Radial load ratings of the gearhead bearings were available in 3 (15A), 10 (15AC) and 15 N (15AK) options, which were all

Table 3.3: Motor–Gearbox Combinations Calculated Values

Variable	Combination 1	Combination 2	Combination 3
P_m^R [W]	1.44	0.288	1.05
$P_m^R/P_{g\_out\_max}$ [-]	2.23	0.446	1.63
G_g	164	164	263
G_{g_select}	152	1024	128
T_{m_cont} [mN.m]	1.47	0.266	1.60
ω_{m_max} [rpm]	4625	31159	3895
T_{m_max} [mN.m]	1.99	0.360	2.17

Table 3.4: Motor–Gearbox Combinations Conditional Checks

Condition	Combination 1	Combination 2	Combination 3
Equation (3.2.17)	Yes	No	Yes
Equation (3.2.18)	Yes	Yes	Yes
Equation (3.2.19)	Yes	No	Yes
Equation (3.2.20)	Yes	No	Yes
Equation (3.2.23)	Yes	No	Yes
Equation (3.2.29)	Yes	Yes	Yes
Equation (3.2.30)	No	Yes	No
Equation (3.2.31)	Yes	Yes	No
Dimensions	Yes	Yes	No

too low. To save on costs the 15A bearing options was used and bushes were placed on the gearbox shaft for additional radial support.

3.2.5 Characteristic Curve

Once the final motor–gearhead combination was selected, the current, efficiency, mechanical power and characterisitc curve was plotted in MATLAB, with labelled load points as shown in Figure 3.6, using the equations described in section 3.2.1. This gave a visual perspective of the motor operation. The label representations are as follows:

1. A — Load case 1 continuous torque.

2. B — Load case 1 intermittent torque.

3. C — Load case 2
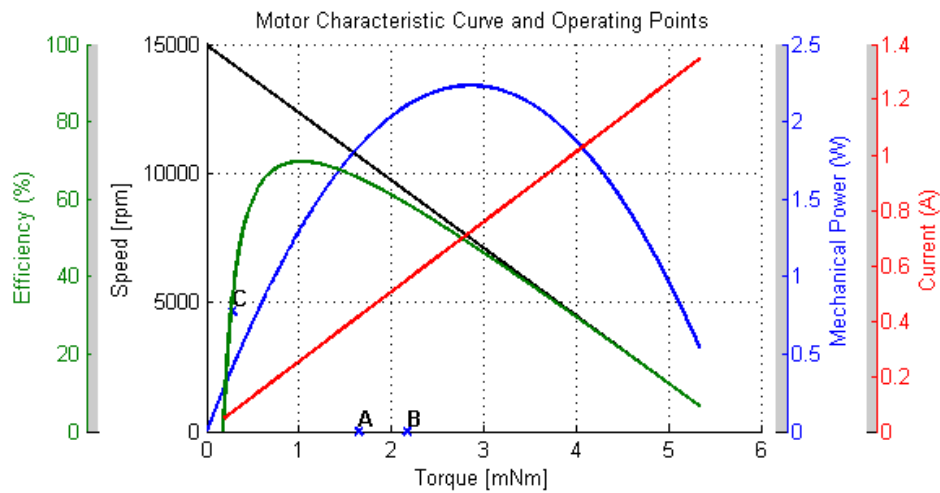
Figure 3.6: Selected Motor Characteristic Curve with Load Points

3.3 Microcontroller

The microcontroller was the most important electronics part because it was responsible for accepting user commands, monitoring measurements, and controlling the motors. A specific number and type of pins were needed to achieve this. Considered factors and a table of minimum requirements for the MCU were listed and used to assist with the selection process. Two options are compared here.

A number of factors were regarded when reviewing possible MCU options. Each are listed and briefly explained as follows:

- design & manufacturing time — circuit design, component selection and soldering times.

- cost

- peripherals — pin numbers, types, features, communication options.

- performance — instruction and data processing speed, and memory size.

- size — total dimensions.

- software support — free download and usage, example code, tutorials.

- ease of use — difficulty of programming setup process.

- availability — number of options, delivery time, available stock.

The first decision to be made was whether to use a protoyping (pre–fabricated) board or custom MCU circuit. The latter only requires pins to be soldered before usage, while for the former, a custom circuit has to be designed with many individual components before soldering. Peripherals and performance depend on the chip to be used, but a custom circuit can be contrived for specific requirements. Dimensional requirements are most satisfied by micro protoype boards, as they use minute surface mount packages that are soldered by machines. Generally pre–fabricated boards are more expensive, however, the advantages outweighed the costs for the MCU selection.

Minimum requirements for the MCU were used to filter out most initial options, and are for an MCU that would support basic functionality, as well as sensory and myoeletric control upgrades. The minimum MCU requirements are provided in Table 3.5. Twelve digital input/ouput (I/O) and six PWM pins are all connected to the six h–bridges. Two digital I/O pins could be used for future amputee haptic feedback signals, using two vibration motors. The analogue input channels are used for motor sensors (12 channels), battery voltage monitoring (1 channel), and for amplified EMG signals (2 channels). Additionally, temperature and vibration sensing would each use one channel (2 channels). The clock speed and data bus size relate to the performance, where the former determines the speed at which instructions are performed, and the latter affects the speed of data transfer. Mid–range values are given for the clock speed and data bus size.

Table 3.5: MCU Minimum Peripheral and Performance Requirements

Requirement	Value
Digital I/O Pins	14
PWM Channels	6
Analogue Input Channels	17
CPU Clock Speed [Mhz]	16
Data Bus [bits]	8

Figure 3.7 shows the Teensy 3.1 (SparkFun Electronics, n.d.) and Arduino Micro (Seeed Technology, n.d.) used for a final comparison before selection. Specifications for each were first compared to the minimum requirements, and are listed in Table 3.6.

With its ARM (Advanced Reduced Instruction Set Computing Machine or Advanced RISC Machine) based processor, the Teensy 3.1 outperforms the Arduino Micro in every way, other than the cost. Low power consumption is achieved with a 3.3 V operating voltage; the clock speed is almost five times larger, the data bus is four times larger, the dimensions are smaller, the memory components (FLASH, SRAM, EEPROM) are larger, and more pins are available.
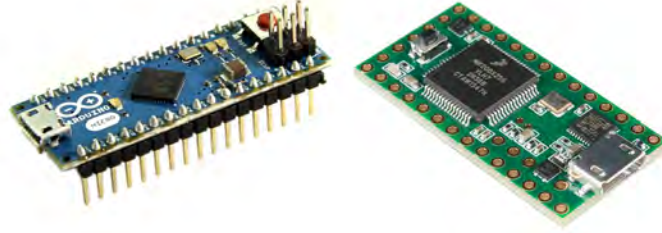
Figure 3.7: MCU Options: Arduino Micro (left), Teensy 3.1 (right)

Table 3.6: MCU Specifications Comparison

Board Name	Arduino Micro	Teensy 3.1
Cost[1] [$]	22.45	29.21
Microcontroller	ATmega32u4	MK20DX256, Cortex–M4
Operating Voltage [V]	5	3.3
Recommended Input Voltage [V]	7 – 12	3.4 – 5.5
Digital I/O Pins	20	34
PWM Channels	7	12
Analogue Input Channels	12	21
FLASH Memory [KB]	32	262
SRAM [KB]	2.5	64
EEPROM [KB]	1	2
CPU Clock Speed [Mhz]	16	72
Data Bus [Bits]	8	32
Length [mm]	48	35.6
Width [mm]	18	17.8

1. Costs are estimates based on quotations and tax in South Africa

Comparing both options to the minimum requirements of Table 3.5, the only problem is with the Arduino Micro, requiring five more analogue input channels. The Teensy 3.1 was then selected. All the minimum requirements are exceeded by the Teensy 3.1, giving it the ability to support all necessary future circuit upgrades/additions.

3.4   H–Bridges

H–bridges were used to control the average voltage applied to the motors. This is achieved used PWM signals from the MCU, enabling and disabling the h–bridge. A basic circuit

level operation is first described, followed by a component selection.

3.4.1 Operation

Figure 3.8 (Allegro MicroSystems, 2013) shows an example of h–bridge internal circuitry. A load supply voltage is applied over transistors with flyback diodes. The motor terminals are connected to points between the transistors. The directional flow of current through the motor can be controlled by switching on either the top left and bottom right transistor, or the top right and bottom left transistor. The purpose of the flyback diodes is to dissipate current spikes during switching to protect the circuitry.
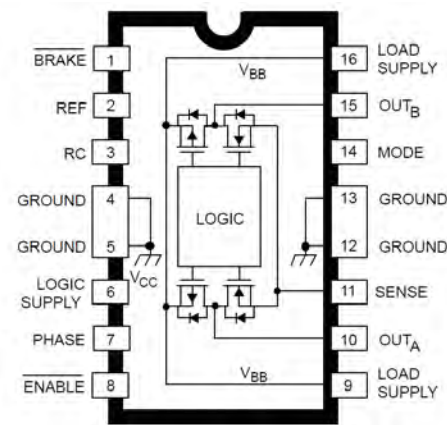
Figure 3.8: Example H–Bridge Circuit

The average voltage over the motor terminals is controlled by enabling and disabling the h–bridge with a PWM signal. A typical PWM signal is shown in Figure 3.9. The voltage switches up to the peak voltage for a pulse width duration for a repeated period. The duty cycle and effective average voltage can be determined with Equation (3.4.1) and (3.4.2), respectively (Cornerstone Robotics, 2015).
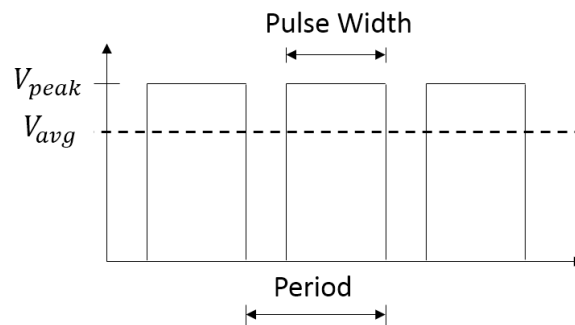
Figure 3.9: PWM Signal Waveform

$$D = \frac{t_{pw}}{t_p} 100\% \tag{3.4.1}$$

$$V_{avg} = DV_{peak} \tag{3.4.2}$$

where

D = PWM duty cycle [%]

t_{pw} = PWM pulse width time [s]

t_p = PWM period time [s]

V_{avg} = effective average PWM voltage [V]

V_{peak} = peak PWM voltage [V]

3.4.2 Component Selection

A comparison was made between the dual motor driver of Figure 3.10 (Pololu Corporation, n.d.) and the single motor driver of Figure 3.11 (RS Components, n.d.) for the final selection of the h–bridge. The former option is pre–fabricated and can simultaneously drive two motors, while the latter option is in a SOP (Small Outline Package) shape. The minimum performance requirements of the h–bridge were predominantly extracted from the motor selection calculations, and are listed in Table 3.7.

Figure 3.10: Pololu DRV8833 Dual Motor Driver

The peak intermittent current was determined by the peak voltage range over the motor terminals as a worst case condition. This occurs during PWM control, when the peak voltages is applied in one direction before changing to the opposite direction. The current is then (Movellan, 2010):

$$I_{max\_peak} = 2\frac{V_{peak}}{R_m} \tag{3.4.3}$$

where,

Figure 3.11: A4973SLBT Single Motor Driver

Table 3.7: Minimum H–Bridge Requirements

Requirement	Value
Peak Intermittent Current [A]	3.9
Maximum Continuous Current [A]	0.63
Maximum PWM Frequency [kHz]	> 25
Support Current Sensing Resistor	Yes

$$I_{max\_peak} = \text{absolute maximum peak motor current [A]}$$

The maximum PWM frequency was selected such that audible noise would be minimised, as the audible frequency range of humans is 64 Hz – 23 kHz (Louisiana State University, 2005). For torque estimation capabilities, discussed later in section 3.5, the h–bridge had to support the addition of a current sensing resistor.

Specifications of each option were extracted from their datasheets and listed in Table 3.8. This assisted with a comparison between the options and the minimum requirements. Both chips satisfy the continuous current, pwm frequency, and current sensing support. However, the peak current rating of 2 A for the DRV8833 falls below the 3.9 A requirement; the DRV8833 did not satisfy the minimum requirements, but the A4973 did.

A further comparison shows that two A4973SLBT are required to achieve the dual driver functionality of the DRV883, but this is still a lower cost option of approximately \$ 9.38 compared to \$ 12.28 and the equivalent dimensions are similar in width and length; even with some additional passive components required for operation. An major advantage of the A4973SLBT is that its height is less that half that of the DRV8833, which reduces the dimensions of the hand to house the circuit board.

Table 3.8: H–Bridge Specifications Comparison

Chip Name	DRV8833	A4973SLBT
Number of Driveable Motors	2	1
Cost[1] [\$]	12.28	4.69
Logic Supply Voltage [V]	n/a	$3 - 5.5$
3.3 V or 5 V Logic Voltage Operation	Yes	Yes
Load Supply Voltage [V]	$2.7 - 10.8$	$5 - 50$
Peak Intermittent Current [A]	2	6
Maximum Continuous Current [A]	1.5	1.5
Maximum PWM Frequency [kHz]	50	70
Support Current Sensing Resistor	Yes	Yes
Requires External Passive Components for Basic Operation	No	Yes
Length [mm]	20.3	10.3
Width [mm]	12.7	10.3
Height [mm]	6	2.65

1. Costs are estimates based on quotations and tax in South Africa

3.5 Torque

To assist the goal of grasp force control, measurements needed to be taken that could be computed into a value that related to, or represented, the forces applied by a finger on an object. Different ways of attaining this were investigated to find the most appropriate solution.

Most measurement methods could be categorised into direct and indirect strategies. A direct approach would be detecting the contact forces present on the surface of the finger, such as using pressure sensors placed at the points of interest. The joint torques can then be estimated using the jacobian matrix (Kargov *et al.*, 2004). An indirect method would be measuring the joint torques, and then estimate the surface forces.

Due to the cable linkage system within the finger, a surface force applied to any of the finger phalanges — in an orthoganal direction to the joint axes — will induce a component torque at the MCP joint. From this reasoning, the torque at the MCP joint can be considered an effective grip torque. The following methods are based on measuring this torque to represent the grip strength.

3.5.1 Concepts

Two possible ways of measuring the MCP torque are by detecting the motor curent or placing a torque sensor within the joint. (Zhao *et al.*, 2006) used a strain gauged based

sensor directly at the MCP joint of the finger. Current measurements can be transformed into motor torque values with Equation (3.2.4) or (3.2.5), followed by multiplications of the speed transmission ratios.

A current measurement approach was adopted to reduce the intricacy of placing sensors within the fingers, and to place the electronics onto one board for easy maintenance. Two common current measurement methods were compared at the circuit level for further optimisation. These are the high–side and low–side shunt resistor methods, which are low–cost, accurate, and compact (Lepkowski, 2003).

The proposed circuit for the high–side method is shown in Figure 3.12. The shunt resistor, R_s, is placed between the power source and the motor, M_1. The measurement circuitry acts as a differential amplifier consisting of individual op–amps with capacitors for filtering. The output voltage is clipped by a zener diode to protect the MCU. This circuit requires nine resistors, four capacitors, three op–amps, and one zener diode.
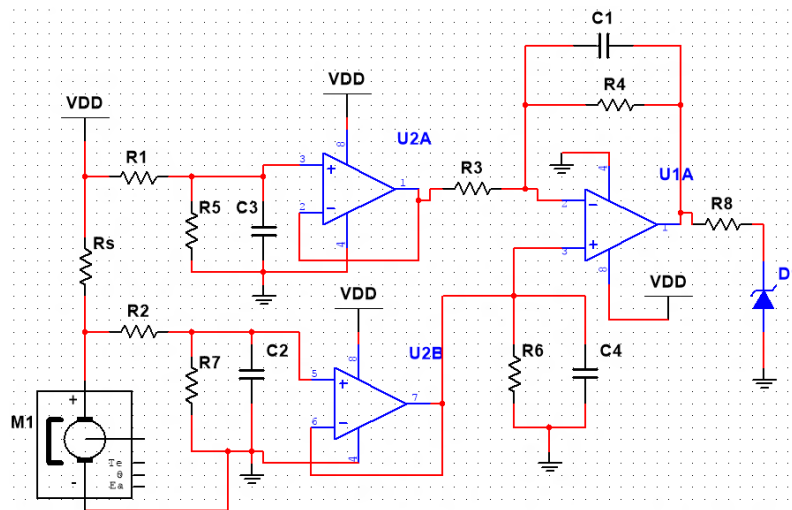
Figure 3.12: High–Side Current Sensing Circuit

The proposed circuit for the low–side method is shown in Figure 3.13. The shunt resistor, R_s, is placed between the motor and ground. One non–inverting op–amp amplifier is needed. The output voltage is clipped by a zener diode to protect the MCU. This circuit requires five resistors, two capacitors, one op–amp, and one zener diode.

3.5.2 Concept Selection

Lepkowski (2003) made a comparison between the two current measurement methods. These points were used to evaluate the attributes of the proposed circuits, which are summarised here for selection purposes. The high side attributes are as follows:

Advantages:

- Electromagnetic interference (EMI) is not affected.
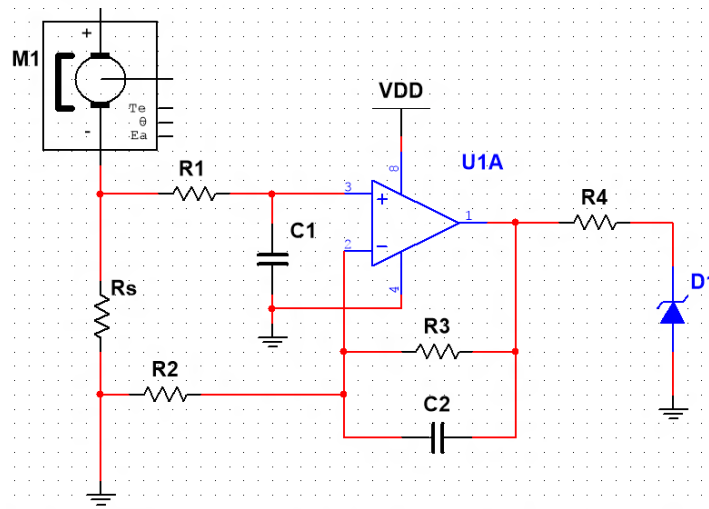
Figure 3.13: Low–Side Current Sensing Circuit

- High fault currents can be detected.

- An integrated IC differential amplifier could be used.

Disadvantages:

- Voltage biasing circuitry is required, adding to the complexity and number of components.

- Input impedances can be low and off balance.

- Integrated IC differential amplifiers are more expensive than using op–amps.

The low side attributes are as follows:
Advantages:

- The sensed voltage is referenced to ground, allowing the use of a lower voltage amplifier.

- Using a non–inverting amplifier gives a large input impedance.

Disadvantages:

- An offset voltage is created in the ground path that increases the likelyhood of EMI issues.

- High fault currents cannot be detected.

To save on costs and ensure compactness, the low side method was selected. Offset voltages due to EMI could be compensated for in software, and the capacitors would be selected to maximise the filtering characteristics.

3.5.3 Gain & Filtering

This section provides a summary of the methods, formulae and values used for determing the component values for the previously selected circuit of Figure 3.13. The first step was determining the resistor values with the amplifier gain.

To minimise the maximum voltage of the sense resistor, R_s, a value of 0.1 Ω was used. From here, the maximum swing voltage over R_s was determined with the selected current limit. Using the ratio of this value over the analogue reference voltage gave the amplifier dc gain, given by (Paradiso, 2011):

$$H_c = \frac{V_{o\_max\_swing}}{V_{s\_max\_swing}} \tag{3.5.1}$$

where,

$\quad H_c$ = current amplifier DC gain [V/V]

$\quad V_{o\_max\_swing}$ = maximum output voltage swing [V]

$\quad V_{s\_max\_swing}$ = maximum input voltage swing over R_s [V]

The gain for a non–inverting amplifier is given by the expression (Paradiso, 2011):

$$H_{non\_inv} = 1 + \frac{R_3}{R_2} \tag{3.5.2}$$

where,

$\quad H_{non\_inv}$ = gain for a non–inverting amplifier [V/V]

$\quad R_3, R_4$ = resistors of the circuit in Figure 3.13 [Ω]

A value of 220 Ω was selected for R_2 to minimise the required value of R_3 and the related bias current offsets. R_3 was determined by rearranging Equation (3.5.2) and substituting H_c and R_2. The closest standard resistor values were then selected.

The capacitors were used for filtering out high frequency noise in the measurement. Two individual first order filters exist in the design; R_1 and C_1 at the input create the first one, and the second is from R_3 and C_2. The cut–off frequency of these filters were designed to be as close as possible, such that any frequencies above this value will experience a second order filter attenuation at -40 dB/dec. This frequency was selected based on the maximum sample time to be used in conjunction with the Nyquist theorem, which implies (Baker, 1999):

$$f_{HC} \leq \frac{f_s}{2} \tag{3.5.3}$$

where,

f_{HC} = low–pass filter cut–off frequency [Hz]

f_s = sampling frequency [Hz]

The capacitor values could then be determined by the expression (Neamen, 2007):

$$C_{HC} = \frac{1}{2\pi R_{HC} f_{HC}} \qquad (3.5.4)$$

where,

C_{HC} = first order passive filter capacitance [F]

R_{HC} = first order passive filter resistance [Ω]

Again, the closest standard capacitor values were selected. A summary of the component and design values for the circuit can be seen in Table 3.9. An explanation on the selection of the zener diode and series connected resistor are discussed next in section 3.5.4.

Table 3.9: Current Sensing Circuit Component and Design Values

R_s [Ω]	R_1 [kΩ]	R_2 [Ω]	R_3 [kΩ]	C_1 [nF]	C_2 [nF]	f_{HC} [Hz]
0.1	6.8	220	6.8	47	47	500

The component package sizes were determined by the rated power for the resistors, and the rated voltage for the capacitors. Component packages were selected such that their rated values exceeded the predicted maximum power or voltage, as necessary.

3.5.4 Voltage Clipping

In order to protect the MCU from being damaged by high output voltages exceeding its voltage supply, a clipping circuit was added to the output of the op–amp. This includes a resistor in series with a zener diode, with the new output voltage at the cathode. This is shown separately in Figure 3.14.

This method is in the multiple power supply category, having a separate supply for the op–amp and the ADC (Analogue to Digital Converter). The op–amp supply is at least two volts greater than the ADC supply — the same supply for the motors. This is more convenient for op–amp selection, as most op–amps do not have a rail–to–rail output voltage range (Green, 1998).

Zener diodes are designed to operate with a reverse voltage. The current through the diode is minimal at voltages less than the rated breakdown value. The current in this region is known as the leakage current (Neamen, 2007). Here, the effective impedance is highest and was modelled as Z_z. This value creates slight distortions in the output signal
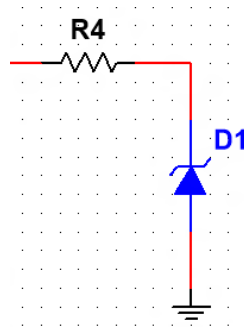
Figure 3.14: Current Clipping Circuit

due to loading effects. This was minimised by selecting a low series connected resistor value.

When the reverse voltage exceeds the breakdown voltage, the current increases dramatically (Neamen, 2007). The diode will clip the output voltage for values greater than the breakdown voltage. To stop the diode from overheating, a series connected resistor was selected to maintain the power dissipation below the maximum value. The selected component values can be found in Table 3.10.

Table 3.10: Voltage Clipping Component Values for Current Sensing

Variable	Description	Value
R_4 [Ω]	series connected resistor of Figure 3.14	27
Z_z [kΩ]	reverse bias impedance during leakage current	1.6
V_z [V]	reverse bias breakdown voltage	3.3

3.5.5 Simulation

Once the components were selected, the behaviour of the circuit was predicted with a simulation in Matlab. Important values were checked to ensure the behaviour was acceptable. These were later verified with measurements in section 5.1.1.

A SISO (single input single output) transfer function model of the circuit was derived, resulting in:

$$\frac{v_{oc}}{v_{ic}} = T_c(s) = \frac{Z_z}{R_4 + Z_z} \frac{sR_3C_2 + R_3/R_2 + 1}{(1 + sR_1C_1)(1 + sR_3C_2)} \tag{3.5.5}$$

where,

$T_c(s)$ = transfer function for current circuit [V/V]

v_{oc} = output voltage for current [V]

v_{ic} = input voltage over R_s [V]

Z_z = equivalent zener diode resistance

R_s, R_1, R_2, R_3, R_4 resistors of the circuit in Figure 3.13 [Ω]

C_1, C_2 capacitors of the circuit in Figure 3.13 [F]

The magnitude and phase of $T_c(s)$ was plotted over frequency in Matlab to create the bode diagram of Figure 3.15. This model assumes the op–amp behaves in an ideal manner; the current between the input pins is negligible, and their voltages are equal.
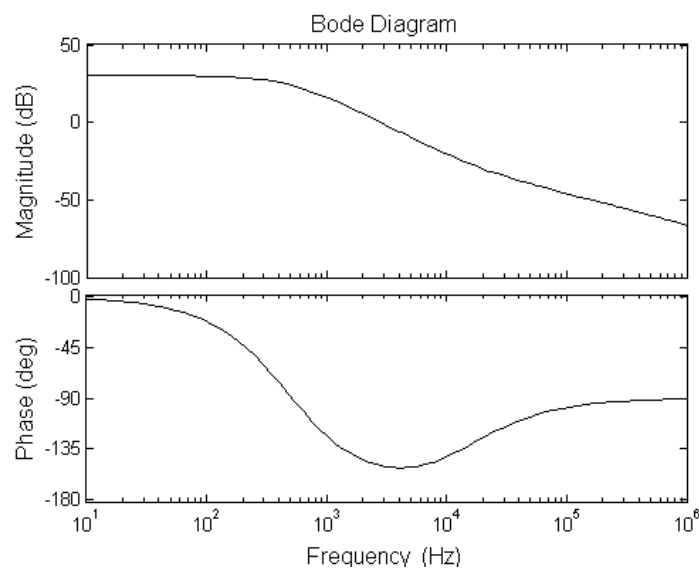
Figure 3.15: Current Circuit Bode Plot

The important values of this simulation include the DC gain, cut–off frequency, and the attenuation of an input signal with the PWM frequency. The DC gain is the gain for a non–oscillating input signal component. There is only one cut–off frequency for this circuit, the high cut–off frequency, which also represents the bandwidth of the filter. This is the frequency at which the output signal is -3 dB less than the DC gain. The current input waveform will have a frequency close to the PWM signal because the motor voltage is controlled with a PWM signal, and so the attenuation at this frequency, relative to the gain at the cut–off frequency, can be used to show how much of an error this will produce. This was determined using the equation:

$$B = 20 \log \frac{H_f}{H_c} \tag{3.5.6}$$

where,

B = attenuation at a specified frequency [dB]

H_f = gain at a specified frequency [V/V]

Manipulating Equation (3.5.6), the error percentage due to EMI with the pwm frequency is:

$$e_B = \frac{1}{10^{B/20}} 100 \tag{3.5.7}$$

where,

e_B = read error due to EMI with attenuation B [%]

Important characteristic values from the simulation were extracted and listed in Table 3.11 for later comparison with measurements.

Table 3.11: Current Circuit Simulation Values

Variable	Description	Value
H_c [V/V]	current amplifier DC gain	31.9
f_{HC} [Hz]	low–pass filter cut–off frequency [Hz]	320
f_{pwm} [Hz]	PWM frequency	46875
B_{pwm} [dB]	attenuation at PWM frequency	66.1
e_{B_pwm} [%]	read error due to EMI with the PWM frequency	0.049
f_{s_min} [Hz]	minimum sampling frequecny	640
t_{s_max} [ms]	maximum sampling time	1.56

3.6 Speed/Position

Commanding the hand to change to different grasp types requires moving each finger to specific positions. From there, the speed of closing and opening the fingers gives the user more functional control. A simple, cost–effective and reliable technique was needed to measure the speed and position of the fingers. Depending on whether the speed or position is directly measured, the unmeasured value can be determined numerically using either integration or differentiation, respectively. This section covers the concepts, selection, and circuit–level design to achieve these goals.

3.6.1 Concepts

Three main options were considered. The first was analogue or incremental encoders, the second was a flexure sensitive resistor, and the third was a sensorless method based on the motor back EMF.

Encoders are one of the most common technologies used to measure rotational position. Once mounted onto a rotating shaft, the embedded electronics communicate measured positional data in analogue or digital form. Incremental encoders are the most basic type, only monitoring a change in position. Absolute encoders maintain positional data after the power has been switched off (Bowman, 2009).

The following two concepts were considered in more detail as they required circuitry to be designed. The one is based on the flexure sensitive resistor used by van der Riet (2014). This sensor is lightweight, paper thin, and in a long rectangular shape that could be placed within and along the length of each finger. As the sensor is bent due to a change in finger position, the resistance changes. This relationship could be determined experimentally for software implementation.

A measurement circuit using the flex sensor can be seen in Figure 3.16. A changing analogue voltage across the sensors resistance (R_2) is created with a voltage divider, using resistance R_1. This value is buffered by the U2A op–amp before being amplified by the inverting amplifier. The voltage at the positive terminal of the U1A opamp is used to offset the output voltage. Capacitors are used for filtering. This offset voltage circuit would be required for every sensor.
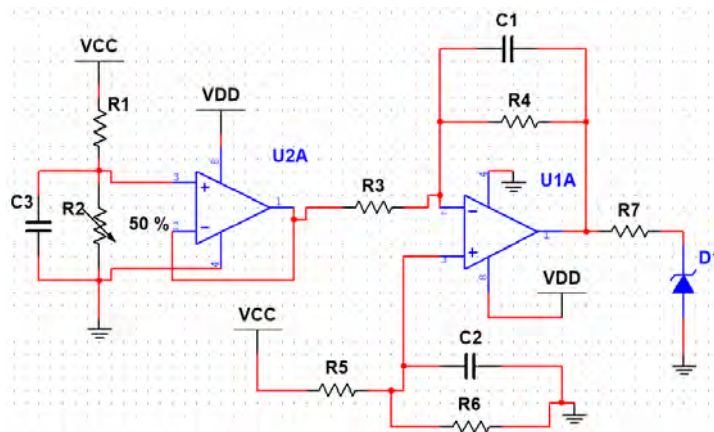
Figure 3.16: Flex Sensing Circuit

The back–EMF of a motor is directly related to its speed through the motor constant, as stated in Equation (3.2.3). This method is considered sensorless because it does not require mechanical coupling. The concept circuit is shown in Figure 3.17. This circuit was designed such that at zero speed the ouput voltage would be at the centre of the ouput voltage range. Depending on the direction of the motor rotation, the output voltage would either rise or lower.
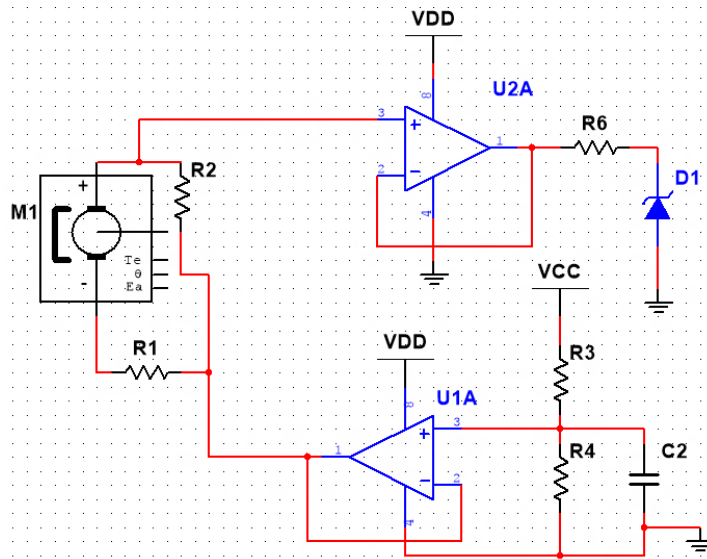
Figure 3.17: Back-EMF Sensing Circuit

The input to the U1A op-amp is used to set the output voltage centre value. Only one instance of this part of the circuit is required for all six motors. The resistors connected to the motor terminals attenuate the emf value and minimise the output currents of the U1A op-amp. Minimising these currents reduces any affects on the motor operation.

The U2A op-amp is used as a voltage follower, and does not use any filtering circuitry as the back-emf is a relatively constant voltage value for a fixed speed.

3.6.2 Concept Selection

Placing an encoder onto a motor shaft would use up space that could rather be used by a larger, and more powerful motor. Space at the MCP joints of the fingers was limited and could rather be used to strengthen the fingers.

The flexure based sensor has a non-linear relationship between resistance and flex. This would imply a non-linear relationship between resistance and rotational position. This relationship would need to be determined by taking actual positional measurements using a different method, and then finding the best fit function to the data. Each finger would have to be fitted with a sensor, requiring additional mechanical design. The flexure measurement circuitry will require 2 op-amps for every circuit.

The back-EMF was the selected concept for its sensorless application, simplicity, low number of components, and low-cost components. The circuit not only facilitates bidirectional speed measurement, but also physically separates the electronics from the mechanics.

3.6.3 Gain & Filtering

The only voltage gain ratio used in the circuit is that of the resistors in parallel with the motor, used to attenuate the EMF. This is because the maximum readable speed value of 5500 rpm produced an EMF of $\pm$ 2.28 V, and needed to fit into half the maximum

analogue value range of 1.65 V. A zero speed would be offset to produce a midway voltage of 1.65 V, allowing directional speed measurement; 3.0 V would imply a positive speed of 5500 rpm, and 0 V would imply a negative speed of -5500 rpm. The required gain was determined by:

$$H_e = \frac{V_{o\_max\_swing}}{2V_{emf\_max\_swing}} \qquad (3.6.1)$$

where,

$\qquad H_e$ = required voltage gain of the EMF voltage [V/V]

$\qquad V_{o\_max\_swing}$ = maximum output voltage swing [V]

$\qquad V_{emf\_max\_swing}$ = maximum EMF voltage swing [V]

The implemented gain is based on the voltage divider ratio given by:

$$H_{emf} = \frac{R_2}{R_1 + R_2} \qquad (3.6.2)$$

where,

$\qquad H_{emf}$ = EMF amplifier DC gain [V/V]

$\qquad R_1, R_2$ = Resistors of the circuit in Figure 3.17 [Ω]

These resistor values were selected to be in the kΩ range to minimise the affect the offset voltage would have on the motor operation.

The EMF op-amp output voltage was not filtered because the back-emf was a relatively constant value for a fixed speed. The capacitor labelled C_2 of the emf circuit was used for filtering the offset voltage value, which was selected using Equation (3.5.4) to give a cut–off frequency of 482 Hz. This cut-off frequency could be as low as possible because it would only maintain a more constant EMF offset voltage.

Using the described design procedure, the selected component and design values can be found in Table 3.12. The component package sizes were determined by the rated power for the resistors, and the rated voltage for the capacitors. Component packages were selected such that their rated values exceeded the predicted maximum power or voltage, as necessary.

3.6.4   Voltage Clipping

The voltage clipping circuit for emf measurement was exactly the same as the one for the current measurement circuit. The same value series resistor and zener diode were used. Refer to section 3.5.4 for component selection, and to section 5.1.1 for measurement details.

Table 3.12: EMF Circuit Component and Design Values

Variable	Description	Value
H_{emf} [V/V]	EMF amplifier DC gain	0.62
V_{emf_offset} [V]	EMF voltage offset	1.65
R_1 [kΩ]	Resistor of Figure 3.17	20
R_2 [kΩ]	Resistor of Figure 3.17	33
R_3 [kΩ]	Resistor of Figure 3.17	33
R_4 [kΩ]	Resistor of Figure 3.17	33
C_2 [nF]	Capacitor of Figure 3.17	22

3.7 Op-amp

The op-amps used in the measurement circuits were selected to be the same for convenience. The selection procedure is discussed here as it applies to the torque and speed measurement circuits. The main specifications considered for selection are described by Baker (2003). The selected op-amp was an LM358 by Unisonic Technologies. The specifications of this op-amp are used to show how it satisfied the requirements.

The first consideration was the output voltage range for the available supply voltages. The op-amps positive and negative power supply rails were connected to the motor supply voltage and ground rail, respectively. Large capacitors were placed between these supply rails at the motor h-bridges to minimise voltage spikes from the pwm switching. The maximum required output voltage was chosen to be 3.3 V, with a minimum positive supply rail of 6.0 V. An output voltage range beginning at the ground rail would be ideal, but realistically values less than 100 mV are more common. The 6.0 V supply was within the 3V – 32V range of the LM358. With this supply voltage, the maximum op-amp output would be about 4.0 V; larger than 3.3 V as required.

The GBWP (Gain Bandwidth Product) of an op-amp depends on the open-loop bandwidth and the open-loop gain and is defined as (Neamen, 2007):

$$GBWP = H_{ol} f_{BW\_ol} \tag{3.7.1}$$

where,

$GBWP =$ Gain bandwidth product [Hz]

$H_{ol} =$ Op-amp open-loop gain [V/V]

$f_{BW} =$ Bandwidth frequency [Hz]

This value should be at least one hundred times greater than the GBWP of the closed loop op-amp circuit Baker (2003). The LM358 GBWP of 3.16 MHz is close to 310 times greater than the closed loop GBWP of the current amplifier.

The slew rate of an op-amp is the maximum rate of change in output voltage per unit time (Neamen, 2007). This value will determine whether a filter will create signal distortions. To avoid signal distortion, the following condition should be satisfied (Baker, 2003):

$$\text{Slew Rate} \geq 2\pi V_{op\_out\_p-p} f_{HC} \tag{3.7.2}$$

where,

V_{out_p-p} = peak-to-peak op-amp output voltage [V]

f_{HC} = low-pass filter cut-off frequency [Hz]

Taking V_{out_p-p} = 3.3 V and f_{HC} = 320 Hz, the slew rate would need to be at least 6.6 kV/s. The slew rate of the LM358 was 1.7 MV/s, which is more than 1000 times larger than the requirement.

The ICMVR (input common mode voltage range) stimulates the range of the common voltage component between the voltages at the inverting and non-inverting terminals of the op-amp. For the current measurement circuit, the ICMVR needed to be 0– 90 mV. For the emf circuit, the ICMVR needed to be 0 – 1.65 V. The minimum ICMVR for the LM358 with a 6.0 V positive power rail was 0 – 4.0 V, which included the requirements. The input bias current describes the amount of current going into or out of the input pins of the op-amp (Baker, 2003). For the current measurement circuit, this bias current will flow through the feedback resistor and cause an offset voltage error in the output. The LM358 has a typical bias current of 45 nA, which would create an output offset voltage of 306 uV and an estimated read error contribution of 0.0093 %.

3.8   Battery

Batteries were needed to power the electronics of the hand, making it portably. Rechargeable batteries were a necessity because the hand would be used on a day-to-day basis. A number of rechargeable battery technologies are available and are briefly described here, with reasons for selection.

3.8.1   Selection

Commonly available rechargeable battery technologies include Nickel Cadmium (NiCd), Nickel-Metal Hydride (NiMH), Lead Acid, Lithium-Ion (Li-ion), and Lithium Ion Polymer (Li-Po). The most important battery characteristics for selection were high energy density and lightweight to minimise the additional load the amputee would have to carry, but still have sufficient energy to power the electronics. Li-ion and Li-Po technologies best

suited the desired characteristics (Buchmann, 2010). Li-ion was selected due to its easier availability and generally lower cost.

After selecting the technology, the voltage of the battery pack needed to be selected. The minimum input voltage to the electronics was taken as 6.0 V. Li-ion battery cells have a nominal voltage of 3.6 V. However the instantaneous voltage changes over the discharge cycle, starting at approximately 4.2 V and ending at 3.0 V (Simpson, n.d.). A two cell battery pack, with the cells in series, was selected to provide a voltage range of 6.0 – 8.4 V. Another consideration was the energy capacity. The worst case condition for capacity was considered as all six motors simultaneously pulling their maximum nominal current for an hour, and was used as the baseline requirement for capacity. This implied a total current draw of 2.78 A, and a capacity requirement of 2.78 A.h. The selected battery pack had a capacity of 2.6 A.h, which was only off by 6.5 % and so it was accepted.

The final check made was for the peak current. In this case, the worst case condition was considered as all six motors simultaneously drawing their maximum intermittent currents for a short time period. This resulted in a combined peak current of 3.56 A. The battery pack current was limited to 4.5 A by the embedded electronics, which gave almost a 1.0 A leeway.

3.8.2 Voltage Monitoring

For more precise motor voltage control, the battery voltage was monitored because it would change over time. This was done using a simple voltage divider circuit in Figure 3.18.
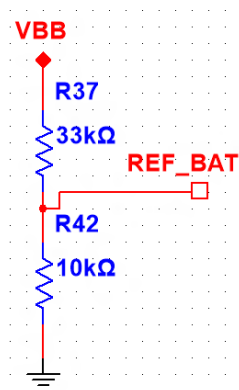
Figure 3.18: Battery Voltage Monitoring Circuit

The VBB power rail was connected directly to the battery, and the output REF_BAT was connected to the MCU. The resistor values were selected to convert the maximum battery voltage of 8.4 V below the analogue reference value of 3.3 V.

3.9 Circuit Fabrication

To achieve more realistic aesthetics, the fabricated circuit was designed to be embedded into the hand. The shape had to conform to the dimensions inside the top cover of the hand, maximising the space usage. The symbolic circuit schematics were made in NI Multisim, and the printed circuit board (PCB) was laid out in NI Ultiboard (See Figure C.1, **??**, **??** and **??** in Appendix C). The 3D model of the PCB is shown in Figure 3.19, and the final fabricated PCB is shown in Figure 3.20.
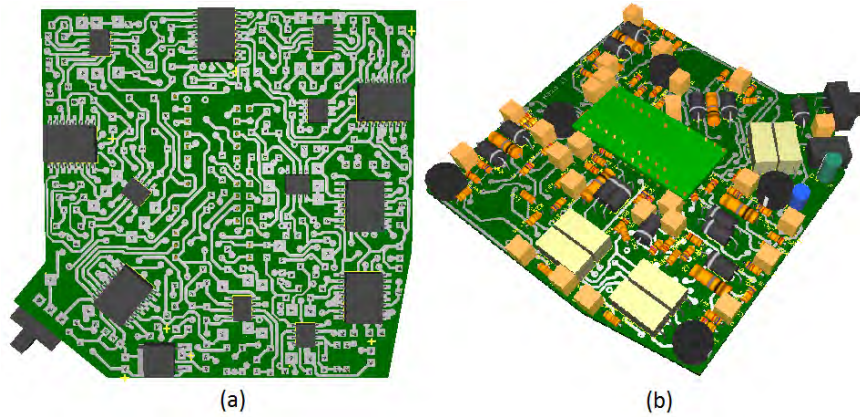
Figure 3.19: Final 3D Model of Electronics Board; (a) Bottom View (b) Isometric Top View
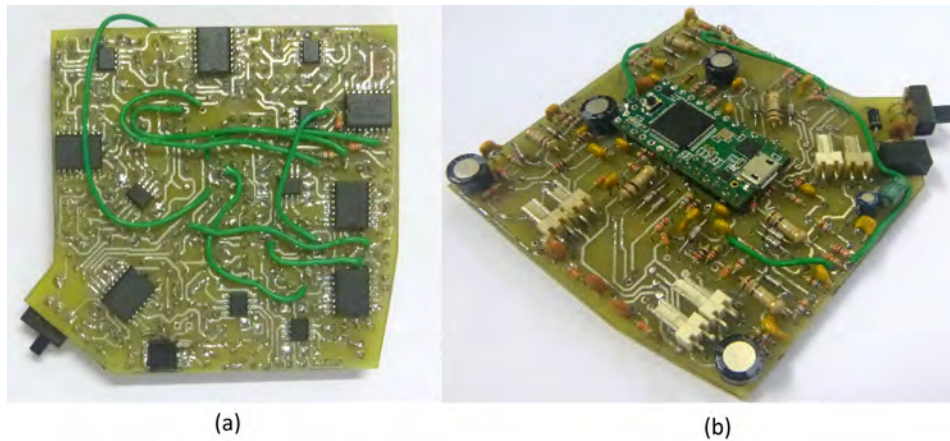
Figure 3.20: Final Physical Electronics Board; (a) Bottom View (b) Isometric Top View

All the components and tracks were manually placed, using vias to transfer between the two layers. This helped locate components into functional blocks such that the motor plugs, power plug and switch, and microcontroller were in convenient access locations. Not all connections were placed on the PCB, and so external wire connections were made to complete the left out connections. One additional external connection was made for

the ground because ground loop voltages were initially present, creating offset voltages in the current measurement circuitry.

The dimensions were critical for ensuring a good fit. The PCB boarder was created by extracting dimensions from the 3D model of the hand. Components were selected to keep their heights to a minimum, such that the thickness of the palm could be minimised.

Virtual dimensional checks were performed by placing the 3D model of the PCB into the 3D model of the hand, as shown in Figure 3.21. The surface mount op-amps and h-bridges assisted evenly separating the tracks between the two available layers. All the surface mount components were placed on one side, while all discrete components were placed on the other, including the Teensy 3.1. The hand was designed such that the left and right hand version would accept the same PCB design so that only one type of PCB was needed. For the right hand version, the PCB is flipped over, as was done in the physical model shown in Figure 3.22.
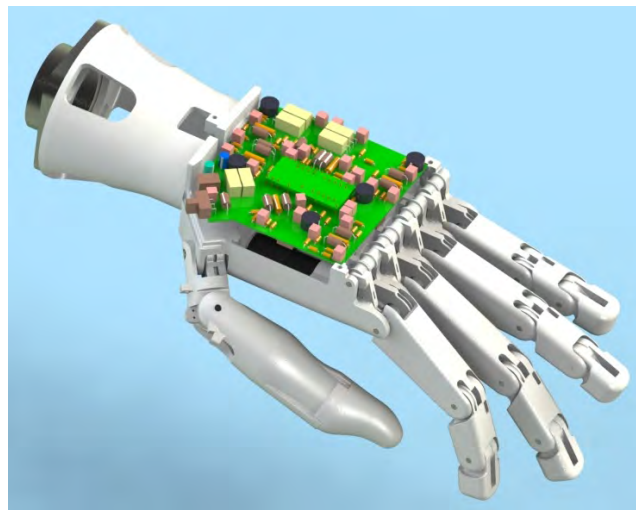
Figure 3.21: 3D Left Hand Model with Electronics
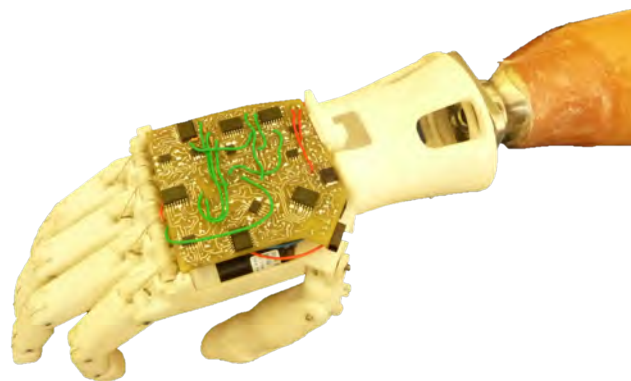
Figure 3.22: Physical Right Hand with Electronics

To accommodate future additions, pins on the Teensy 3.1 were left unused such that these could be connected to other components. These would include EMG signals from an amputee, and other sensory information such as temperature and vibration.

3.10   Chapter Summary

The electronics hardware architecture encompassed the strategy of how the components would be arranged, such that a control loop could be set up between the MCU and motors, power could be supplied, and future additions could be made. Six of the same motors were chosen using the load requirements and procedural selection criteria.

The Teensy 3.1 was chosen for MCU purposes, satisfying a number of performance requirements such as PWM channels and analogue input pins. The selected h–bridge is able to withstand the high current spikes and input supply voltage for PWM control.

Motor current and back–emf circuits were designed for torque and speed estimation, respectively, which could be determined by multiplying the measurements by specific motor constants. The op–amps of these circuits had characteristics and limitations that were taken into the consideration.

A custom PCB was designed and manufactured, holding all circuitry and only requiring the motors to be connected by individual plugs. This was powerable by a 7.2 V, 2.6 A.h Li-Ion battery, whose voltage was monitored by the MCU for better motor control.

4 SOFTWARE CONTROL SYSTEM

To give the hand functionality, each of the fingers needed to be controlled by their position, speed, and grip force. Control software was designed and programmed onto the MCU to achieve this. As the external amputee circuitry and control was out of the scope of this research, control commands were given by a Personal Computer (PC). The diagram of Figure 4.1 shows how the PC replaced the amputee.
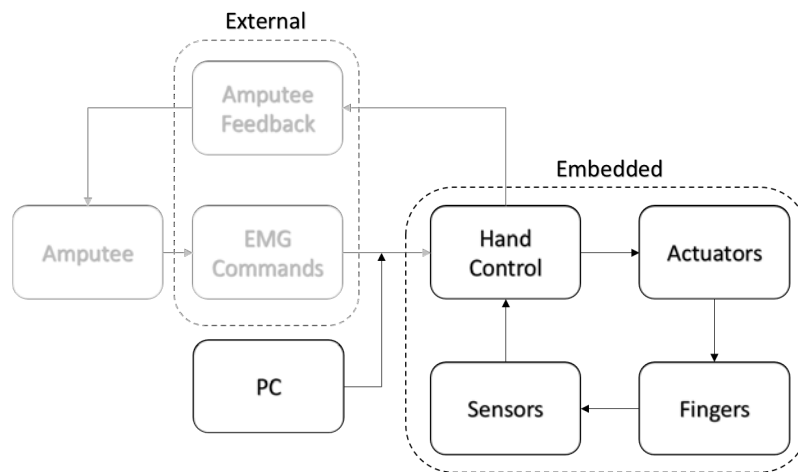
Figure 4.1: Overview of Hand Control via the PC

This chapter describes the details of how software was used to perform low level control (individual finger speed, force, and position), high level control (multiple fingers), and communication from the PC.

4.1 SOFTWARE ARCHITECTURE

The object orientated programming language of C++ was used in the arduino IDE environment to program the MCU. Classes were designed using a bottom–up approach. The hierarchical relationship between the classes is shown in Figure 4.2. Object instances were created such that there was one hand object, one battery object, six finger objects within the hand object, which each had a motor object. Each of these classes are described in further detail here.
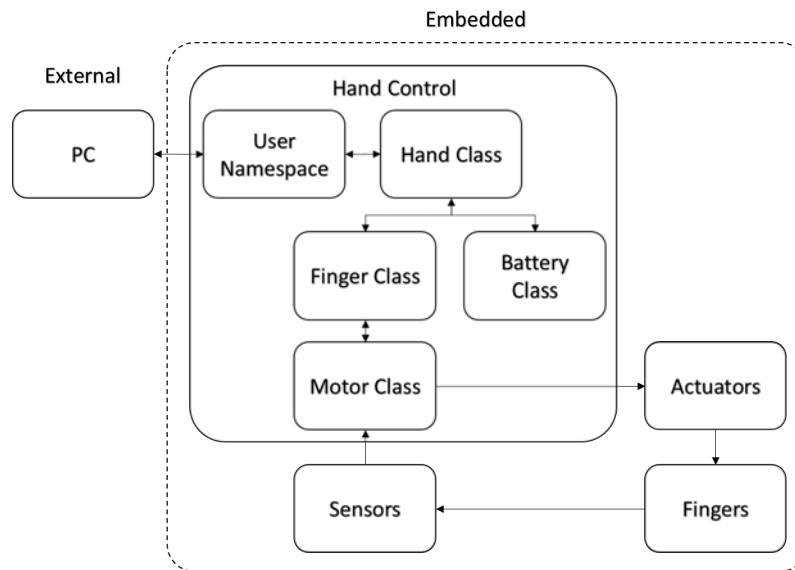
Figure 4.2: Software Class Information Flow Diagram

4.1.1 User Namespace

This namespace is a collection of variables and functions used to monitor the serial communications port for new commands from the PC. Commands were sent from the PC through a seven character long string, by using a Graphical User Interface (GUI) developed in visual studio. Further details of the GUI are described in section 4.2.

4.1.2 Hand Class

This class holds all six instances of the fingers, and a battery object. Each grasp position of the hand determines the starting position of each finger, and which fingers can be closed/opened during that grasp. All of these settings are defined within the Hand class.

4.1.3 Finger Class

The Finger class is responsible for the high level control of its motor. Proportional Integral Derivative (PID) torque and speed control, positional control, as well as closing and opening sequences using Finite State Machines (FSMs) are all encompassed within this class.

4.1.4 Motor Class

The measurement of instantaneous motor attributes, and the application of specific terminal voltages are handled by the Motor class. Measurements include current for torque estimation, and motor back–emf for speed estimation.

4.1.5 Battery Class

Battery voltage monitoring is performed using this class. This assisted with more precise motor voltage control.

4.1.6 Digital Filtering

A moving average algorithm using three array elements was implemented for the current and speed measurements. The low number of elements enabled fast responses. It assisted the hardware analogue filters in removing high frequency noise. This was important for the speed measurement because no analogue filter was present in the circuitry, only for the current measurement.

4.2 USER COMMAND EMULATION

User emulation was achieved by creating a custom GUI in the visual studio environment, based on visual basic programming, to be used from a computer. This software was useful while testing each hand function, and could be used for quality control and debugging processes in the future. The main functions of the GUI were split between individual finger and complete hand control. Each of these aspects are described without going to far into the control details, which are discussed later.

4.2.1 GUI Settings

The GUI during individual finger control is shown in Figure 4.3. Here the "Finger Control" tab is selected, which has a list of all the finger options to select from. Configurable settings include the selected finger, speed intensity, torque intensity, torque limit level, and the position the finger is set to close to.
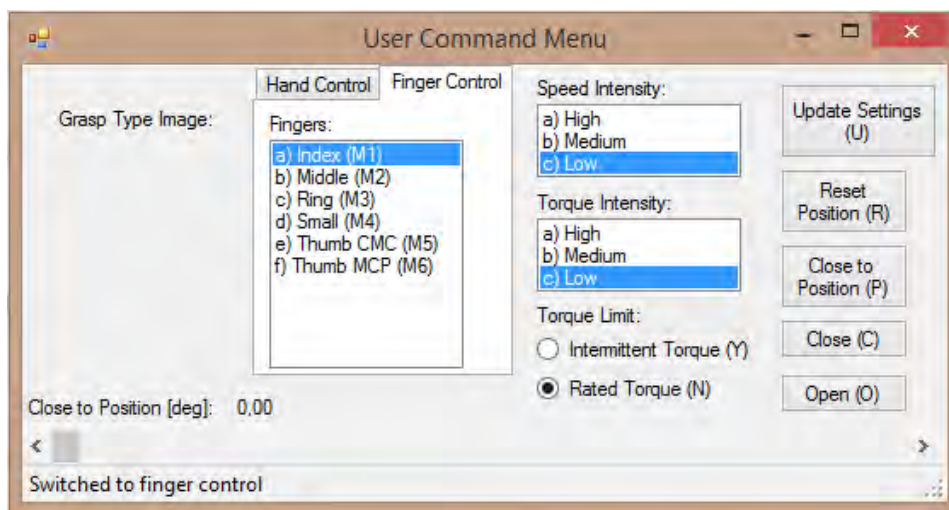
Figure 4.3: Individual Finger Control with the GUI

The "Update Settings" button is used to send the current selected settings to the MCU. The torque intensity sets the rate at which the torque changes during torque/force control. The maximum level that the torque reaches depends on whether the intermittent or rated limit are selected. The rated level is for continuous loading, while the intermittent level is for higher loading within a few seconds. The "Close to Position" can be changed by moving the position of the horizontal scroll bar that goes up to ninety degrees.

The GUI during hand control is shown in Figure 4.4, with the "Hand Control" tab selected and a list of available hand grasp types. These grasp types are the ten most important as described in section 2.1.3. When each grasp type is selected, the corresponding position is illustrated under the "Grasp Type Image" label.
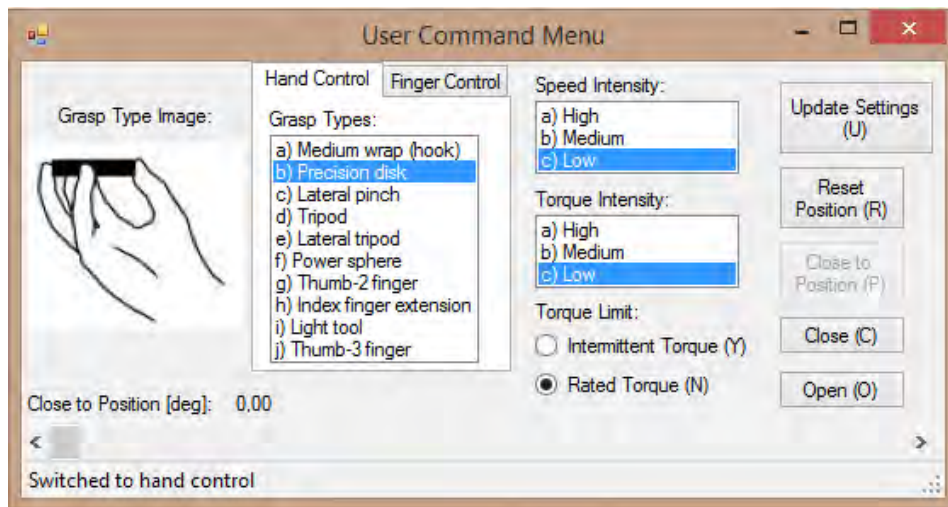
Figure 4.4: Hand Control with the GUI

4.2.2   Close Button

For finger control, this will command the selected finger to close with the desired settings. In hand control, specific fingers for the selected grasp will close.

4.2.3   Open Button

For finger control, this will command the selected finger to open with the desired settings. In hand control, specific fingers for the selected grasp will open.

4.2.4   Close to Position Button

This button is only available during finger control. Using the set position on the horizontal bar, the selected finger will close from it's zero position (completely open) through the set angle with the selected speed intensity.

4.2.5   Reset Position Button

In finger control, the selected finger will continue to open until it reaches its maximum opening position. This is detected by monitoring the motor current for a spike at the reset/zero position. During hand control, all of the fingers are opened to their reset/zero positions. The necessity for the reset is explained in section 4.5.

4.2.6   Update Settings Button

When in finger control this button would only update the selected settings, but in hand control is would update the settings, reset the fingers to their zero positions, and then move them into position for the selected grasp type.

4.2.7   Command Communication Protocol

The settings and commands from the GUI are sent to the MCU using a seven character string via the serial port. Each character is described by referring to its index.
Character at index:

- 0 – control type; 'F' or 'H' for finger or hand control.

- 1 – command type; 'C' for closing, 'O' for opening, 'S' for resting or no command, 'R' for reset, 'U' for update, 'P' for close to position.

- 2 – selected finger or grasp; 'a' to 'j' in hand control, or 'a' to 'f' in finger control.

- 3 – speed intensity; 'a', 'b', or 'c'.

- 4 – torque intensity; 'a', 'b', or 'c'.

- 5 – intermittent torque selection; 'Y' for yes, or 'N' for no.

- 6 – close to position value; ranges from character value zero to 127 (maps the close to positional value).

4.3   FINGER TORQUE AND SPEED CONTROLLER

The torque and speed of each motor were controlled with a Proportional Integral (PI) controller. These controllers could not be active simultaneously because both used the motor terminal voltage as their outputs. Each controller was activated during certain conditions. Torque control would be active while an object is touched, while speed control would be active while not in contact with an object.

Figure 4.5 shows the control diagram of the described arrangement. Switches S1 and S2 symbolise the active/inactive control of each controller depending on object contact. The set values are summed with the measured values to provide the errors that feed the
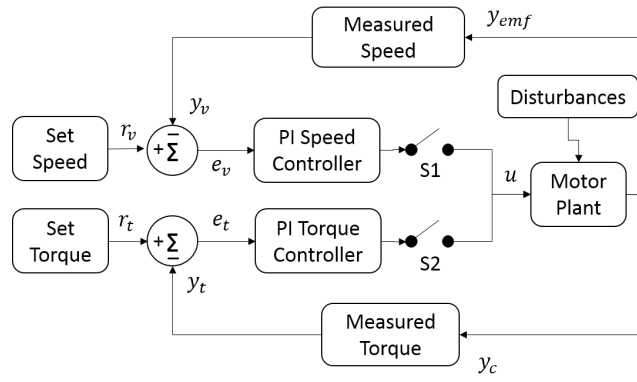
Figure 4.5: Torque and Speed Controllers

controllers. Depending on which switch is closed determines which control variable voltage drives the motor.

Each controller sets the motor terminal voltage using the following equations (Franklin *et al.*, 2010):

$$u_v = k_{pv}e_v + k_{iv}\beta_{ev} \tag{4.3.1}$$

$$u_t = k_{pt}e_t + k_{it}\beta_{et} \tag{4.3.2}$$

$$e_v = r_v - y_v \tag{4.3.3}$$

$$e_t = r_t - y_t \tag{4.3.4}$$

$$y_v = \frac{y_{emf}}{K_m} \tag{4.3.5}$$

$$y_t = K_m y_c \tag{4.3.6}$$

$$\beta_v = \beta_{ev}^n = \beta_{ev}^{n-1} + e_v \tag{4.3.7}$$

$$\beta_t = \beta_{et}^n = \beta_{et}^{n-1} + e_t \tag{4.3.8}$$

where,

u_v = speed control variable [V]

u_t = torque control variable [V]

k_{pv} = speed controller proportional constant [V/rpm]

k_{pt} = torque controller proportional constant [V/N.mm]

k_{iv} = speed controller integral constant [V/rpm]

k_{it} = torque controller integral constant [V/N.mm]

β_v = speed integral error [rpm]

β_t = torque integral error [N.mm]

e_v = speed error [rpm]

e_t = torque error [N.mm]

r_v = speed reference/setpoint [rpm]

r_t = torque reference/setpoint [N.mm]

y_v = speed process variable [rpm]

y_t = torque process variable [N.mm]

y_{emf} = back– emf process variable [V]

y_c = current process variable [A]

n = sample number [-]

A classical approach of determining the control parameters for each controller was adopted. The proportional constant was first increased to improve the response time. The integral constant was then increased until the steady state error was stable and minimal. This approach avoided the requirement of empirically determining the plant of the motor in combination with the finger mechanics, followed by theoretical controller design. Additionally saturation values of the applied motor voltage were used to limit the motor from exceeding the maximum speed and current. The integral error term was also limited to prevent unstable wind–up.

4.4   FINGER CLOSING & OPENING CONTROL

Closing and opening each finger was a complex sequence based on a Finite State Machine (FSM). This FSM monitored whether a close, open, or rest command was being given to the MCU and changed its state depending on these inputs and what state it was currently in. Each state would either be in a speed or torque control mode. Depending on the current state and command, set speed and torque values would change within a ramp profile. These profiles are first described followed by the FSM.

4.4.1   Velocity

The closing speed profile of each finger was in the trapezoidal form. Depending on the selected speed intensity setting, the profile values would change. Figure 4.6 shows the speed profile for a close command. The three available speed settings are shown to have different acceleration and speed limit values. The active region represents an active close command. The speed accelerates to its speed limit in this region. When a rest command is given, shown as the non-active region, the speed decelerates down to zero. ω_{MCP_high} was chosen to be the maximum value the motor was capable of, while the other two speeds were fractions of the former.

4.4.2   Grip Force

As previously mentioned, the grip force was represented by the torque. Similarly to the speed, the torque followed a trapezoidal profile. Figure 4.7 shows the torque profiles for
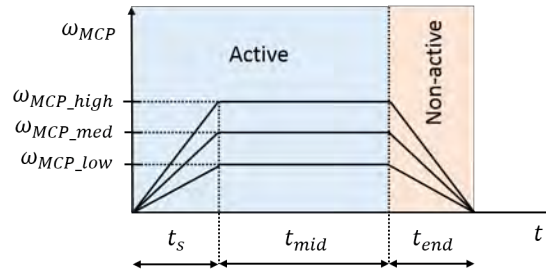
Figure 4.6: Speeds During an Active and Non-active Close Command

the three different torque intensity settings. While a closing command is active (closing region), the set torque increments at a different rate up to the maximum value (rated or intermittent value). When no command is given (resting region) the torque is held constant. This will allow an amputee to maintain the set grip force without having to use his/her muscles, reducing the possibility of fatigue. From this point, opening the hand reduces the applied torque at the same rate as closing. This will enable an amputee to incrementally set the grip force using only a close and open command.
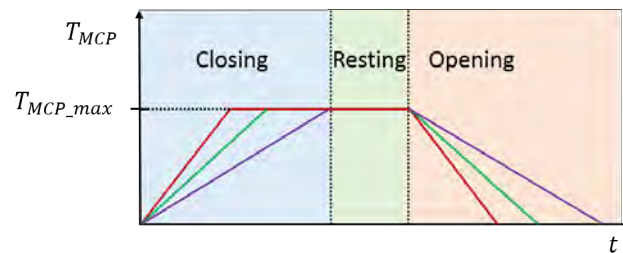
Figure 4.7: Closing, Resting, and Opening in Torque Control

4.4.3   Grip Force & Speed

The FSM for the closing and opening of each finger was responsible for coordinating the state of control and trapezoidal profiles. Three states were used and are shown in Figure 4.8 as "No Touch", "Object Touch", and "Reset Position Touch".

When in the "No Touch" state, speed control is active. During a close, if the torque passes the touch threshold, the state is changed to "Object Touch". Continuing with a close command in this state will continuously increment the torque until a rest command is given, or the maximum torque value is reached. A rest command maintains the set torque, but an open command will decrement the torque. The state will change back to the "No Touch" state if the torque is below the torque threshold or the speed surpasses the its touch threshold. This speed condition is to check whether the finger has slipped past the object and has begun moving again.

The state will move from the "No Touch" state to the "Reset Position Touch" state when the finger is opening and the torque exceeds the touch threshold. In this state the finger
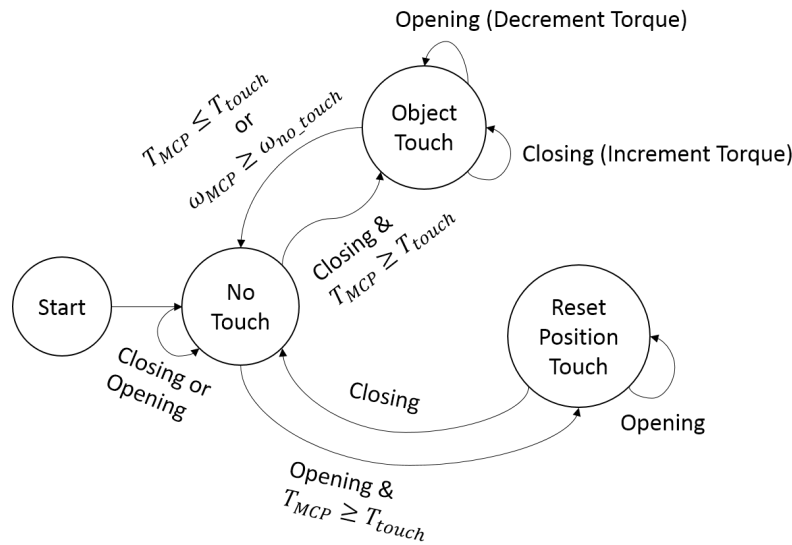
Figure 4.8: Finite State Machine for Finger Closing and Opening

will not attempt to open any further as it is in its zero position. Only a close command will change the state back to the "No Touch" state.

4.5 POSITION CONTROL

The theoretical position of the finger MCP joint can be calculated by integrating the speed. Practically there are a few problems that are sources of errors. Firstly, the back–emf measurement used to determine the speed has errors, which are more prominent at low speeds. Secondly, integrating the speed measurement will integrate the errors, creating a continuously increasing error over time.

A simple strategy was implemented that avoided the compounding error, but lost the continuous monitoring ability. With the finger starting at the zero position, the speed was set to follow a profile, as shown in Figure 4.9, that would move it to the specified close position. No continuously updated position variable was used. Each time a new close to position was set, the finger would need to be reset back to its zero position before performing the command.
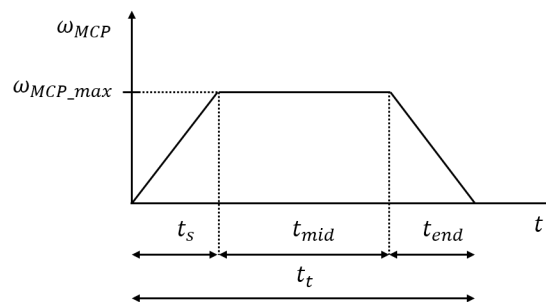
Figure 4.9: Speed Ramp to Close to a Position

The timing in each region of the used trapezoidal profile was important in reaching a specified position. The start and end times were selected to be the same for convenience, and their value was selected by minimising the accelerations such that the finger would still close to 110°within the specified close time of 1.0 s. This reduced the amount of required torque output of the motor, lowering the heat disipation. The middle region time depended on the maximum profile speed, start and end time using:

$$t_s = t_{end} = 0.18s \qquad (4.5.1)$$

$$t_{mid} = \frac{\theta_{MCP}}{\omega_{MCP\_max}} + t_s \qquad (4.5.2)$$

where,

t_s = start region time[s]

t_{mid} = middle region time [s]

t_{end} = end region time [s]

θ_{MCP} = close to position [rad]

ω_{MCP_max} = maximum rotational speed of MCP joint [rad/s]

4.6 CHAPTER SUMMARY

The future EMG control system was replaced by a computer communicating through a serial port to simulate commands by an amputee. The C++ object orientated language was used in arduino to create a number of hierarchical classes, representing different objects in the hand. A custom GUI was created using visual basic and had all possible settings for testing, including various torque and speed intensities, and positions to close to. A finite state machine was used to handle the state of the controller during closing and opening commands, which changed between speed and torque control depending on whether a finger was in contact with an object.

5   EXPERIMENTAL TESTING

The real performance of the hand in each main aspect was checked with measurements. The principal design of the electronics, the control software embedded in the MCU, and the functional usefulness of the hand to an amputee were all tested.

5.1   ELECTRONICS PERFORMANCE

Circuits were designed to measure the back-EMF and the current of each motor. An experimental set-up was made to measure the characteristics of these circuits in order to check their actual behaviour. These also reflected the real measurement limitations by these circuits, and were compared against the designed values to be aware of the errors. The experimental set-up used is shown in Figure 5.1. The equipment used included a signal generator, digital oscilloscope, power supply, cables and a test circuit. The test circuit was designed to test the measurement circuitry for one motor, which consisted of Dual In-line Package (DIP) component versions for convenient prototyping. These were connected up to a Teensy 3.1 for control.
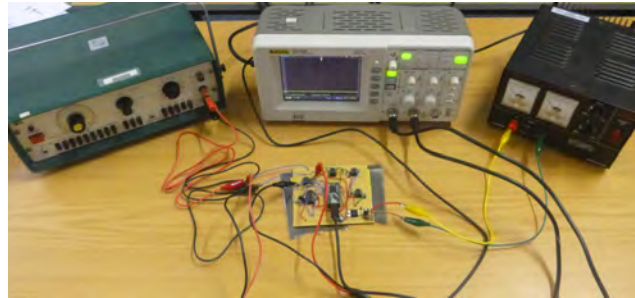
Figure 5.1: Experimental Set–up for Electronics Measurements; Function Generator (Top-left), Digital Oscilloscope (Top Middle), Power Supply (Top Right), Test Circuit (Bottom Middle)

5.1.1   Current Circuit

Three measurements were made for the current measurement circuit: DC gain, cut-off frequency and clipping. For the DC gain, an sinusoidal voltage with an offset value of 20 mV, a peak-to-peak amplitude value of 40 mV and a frequency of approximately 0.08 Hz was used as an input. This created an input varying between 0 V and 40 mV, within the designed range of 0 – 90 mV. The low frequency was used to create an almost DC value, as

well as a reference amplitude for determining the cut-off frequency. The measured output amplitude was 1.16 V peak-to-peak by the oscilloscope. Figure 5.2 shows the measured input and output waveforms. Dividing the output by the input, the DC gain was measured to be 29. Comparing the horizontal offset between the waveforms shows that they are in phase because it is zero. Additionally, the output impedance of the signal generator was not taken into account because it theoretically would not change the DC gain.
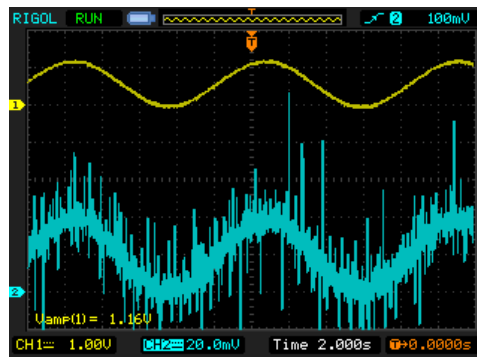
Figure 5.2: Current Circuit DC Gain Measurement; Input Waveform (Bottom), Output Waveform (Top)

The cut-off frequency measurement was done by increasing the input sine wave frequency, keeping all other settings the same as the DC measurement, until the output waveform amplitude was 0.707 times the DC value. This value would be affected by the output impedance of the signal generator because it would contribute to a low cut-off frequency. Its resistance was 800 Ω, 8.82 % of the resistor it was connected to in series, used to select the cut-off frequency. The measured cut-off frequency is shown in Figure 5.3 to be 260.4 Hz, but compensating for the error produced by the signal generator impedance, the actual measured cut-off frequency was 283.4 Hz.
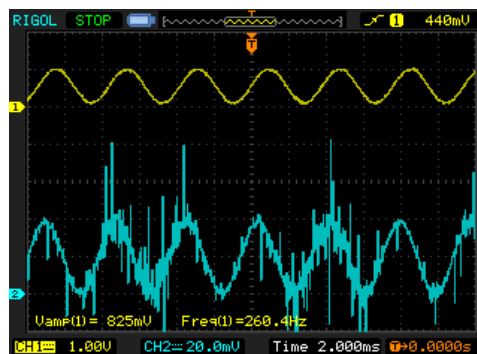
Figure 5.3: Current Circuit Cut-Off Frequency Measurement; Input Waveform (Bottom), Output Waveform (Top)

Voltage clipping was checked by increasing the input offset voltage until the maximum output voltage was limited. This was measured to be 3.45 V. All the values measured

are combined in Table 5.1 for review. The minimum sampling frequency is included by application of the Nyquist theorem, Equation (3.5.3), and the maximum sampling time is determined by inverting this frequency. From this value the applied sampling time was selected to be 1 ms, satisfying the restriction.

Table 5.1: Current Circuit Measured Values

Variable	Description	Value
H_c [V/V]	current amplifier DC gain	29
f_{HC} [Hz]	low-pass filter cut-off frequency	283.4
V_z [V]	Zener diode voltage (clipping)	3.45
f_{s_min} [Hz]	minimum sampling frequency	566.8
t_{s_max} [ms]	maximum sampling time	1.76

5.1.2 EMF Circuit

For the EMF measurement circuit, four different measurements were made: output offset voltage for zero input voltage, DC gain, motor PWM voltage frequency, and the measurement test procedure.

After connecting the input leads together to create a zero input voltage reading, the output offset voltage was measured to be 1.60 V. Connecting the input leads to the signal generator, and applying a flat DC input voltage of 620 mV (within the designed -2.2 – 2.2 V range), the output voltage was 2.00 V. Subtracting the 2.00 V by the 1.60 V offset and dividing by the input voltage of 0.620 V gave the DC gain of 0.65.

The speed of the motor depends on the back-EMF, and the back-EMF depends on the applied motor terminal voltage. The applied effective motor terminal voltage depends on the PWM frequency used. To ensure the motor terminal voltage is applied correctly, the PWM waveform was measured to verify correct duty cycle control. The PWM waveform measurement of Figure 5.4 is a result of a set duty cycle of 12.51 % using a frequency of 46875 Hz and a resolution of 10 bits. The measured waveform had a 12.6 % duty cycle, with a frequency of 46.73 kHz.

Measuring the motor EMF required a specific timing process. At this point the motor to be used was connected to the h-bridge. The PWM settings were maintained as previously mentioned. The procedure began by disabling the h-bridge. This initially created a current spike in the inductance of the motor, but after some time this voltage dissipated, leaving only the back-EMF voltage present. This effect can be seen in Figure 5.5. Here, the back-EMF voltage creates and output voltage of approximately 192 mV. This value could then
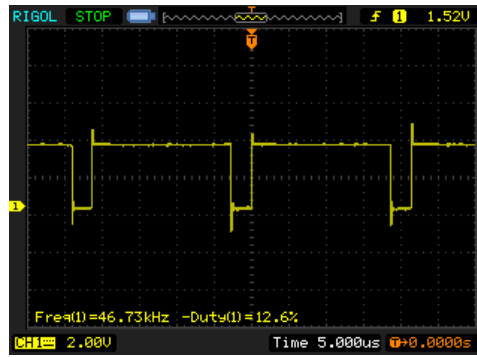
Figure 5.4: PWM Measurement

be used to estimate the speed. In software, the MCU waited for the back-EMF voltage to settle before taking the measurement.
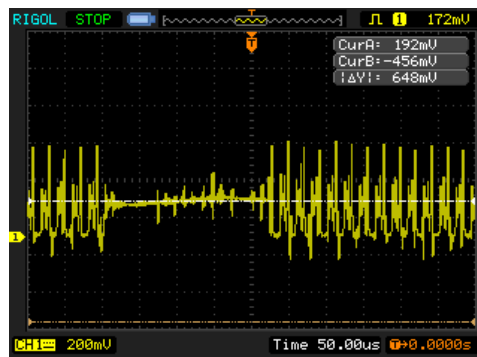
Figure 5.5: Speed Measurement Example from EMF Circuit

During the relatively constant back-EMF voltage, there are still voltage spikes present. This is because the circuit does not have any additional low-pass filter circuitry. Filtering could be a future improvement on this measurement. A summary of the important measurements made for the emf circuit are listed in Table 5.2.

Table 5.2: EMF Circuit Related Measurements

Variable	Description	Value
H_{emf} [V/V]	EMF amplifier DC gain	0.65
V_{emf_offset} [V]	EMF voltage offset	1.6
f_{PWM} [kHz]	PWM frequency	46.73

5.2 CONTROL PERFORMANCE

The operation of each aspect in the control software was verified through measurement. This not only ensured the logic was correct, but also the hardware was systematically behaving properly. This included speed, force, position, and the FSM handling switching between control modes. Each of the control tests was performed on the index finger once the hand was completely assembled.

5.2.1 Digital Filter

Although the current circuit had analogue filtering by the use of capacitors, the back–emf circuit did not. To further reduce noise injection, digital filtering was adopted by applying a standard moving average algorithm. This used the average of the last three samples. The smoothing effects are clearly shown in Figure 5.6, while maintaining a fast response.
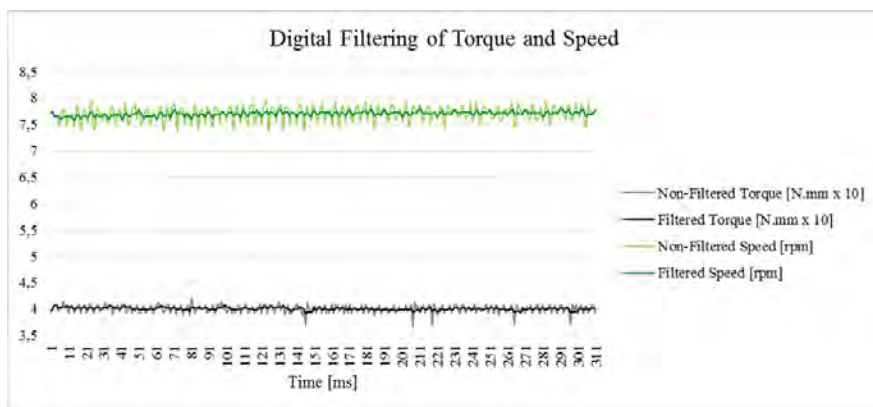
Figure 5.6: Effect of Digital Filtering on the Measurements

5.2.2 Speed Control

After the control parameters were selected as $k_{pv} = 0.945$ [V/rpm] and $k_{iv} = 0.01$ [V/rpm], the principal operation of the speed controller was observed by measuring a step response, shown in Figure 5.7. Initially the speed was zero before being stepped up to 10 rpm at the zero time mark. The measured speed attempts to follow the stepped setpoint, reaching 90 % of the final value at 28 ms (response time) and settling at 39 ms within an error range of ± 4 %. The measured speed shows no apparent overshoot because it does not exceed the setpoint before settling.

An additional safety feature built into the software was saturating the motor terminal voltage at certain limits. These prevented the current and speed exceeding the maximum allowable values, avoiding over-heating and ensuring longer motor life-time. While the maximum speed was not exceeded, the voltage was set to saturated at 2.6 V, but would change to 1.2 V when exceeded.
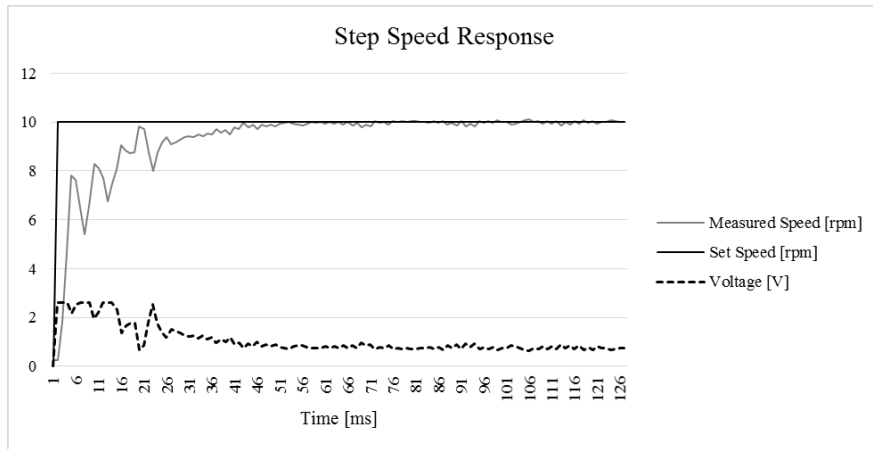
Figure 5.7: Testing the Speed Controller

Following the controller, the speed profile for the three intensity options was tested. Figure 5.8 illustrates the set and measured speeds for each profile. During the acceleration region errors of approximately 7 % were observed on average, showing a favourable tracking ability. This plot only shows the first half of the profiles because the second half has the speeds decelerating to zero at the same rate as the acceleration, with similar tracking.
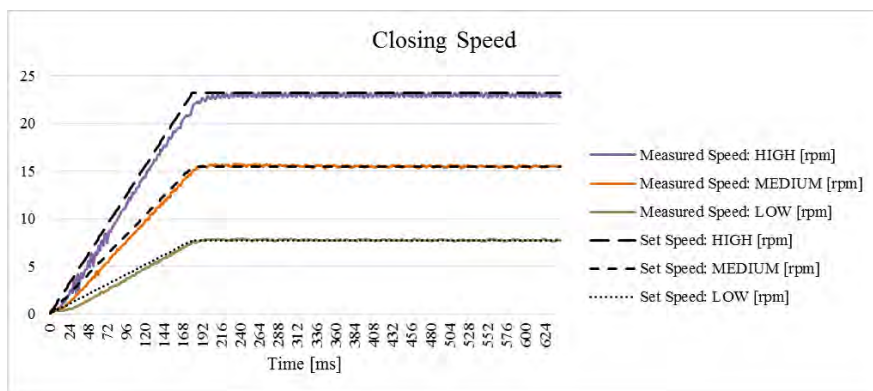
Figure 5.8: Testing the Closing Speed Profiles

5.2.3   Force Control

Control parameters of $k_{pt} = 0.009$ [V/N.mm] and $k_{it} = 0.0001$ [V/N.mm] were selected for the torque controller for force control. These values were more difficult to select in comparison to the speed controller; if the voltage responded too quickly it created current spikes that led to unstable oscillations in the measurements and control.

Figure 5.9 shows the step torque response for a setpoint value of 40 N.mm. The response time is 27.5 times larger than the speed controller, with a value of 770 ms. The settling time is 1106 ms to reach a steady $\pm$ 4 % error range. These larger time values are due

to the response depending mainly on integral action, smoothly increasing the voltage and current to avoid instabilities.
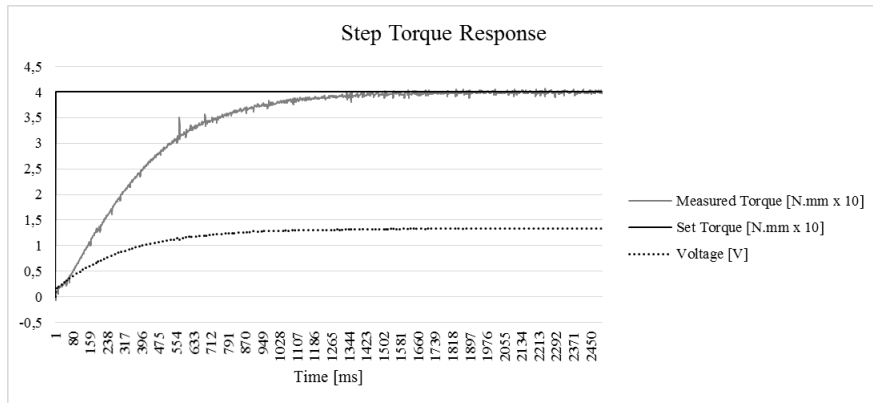
Figure 5.9: Testing the Torque Controller

The torque intensity high, medium, and low settings were tested by commanding the finger to close onto an object, followed by releasing the command at a time such that the final setpoint value was approximately the same for each setting; this is illustrated in Figure 5.10. The rate of change in torque is shown to be different for each setting at the start. The measured torques differ from one another in response times due to the different set profiles, but do not respond fast enough to track the set values with minimal error.

The measured torques differ from one another in an almost relative manner to the set profiles, but do not response fast enough to track the set values with minimal error.
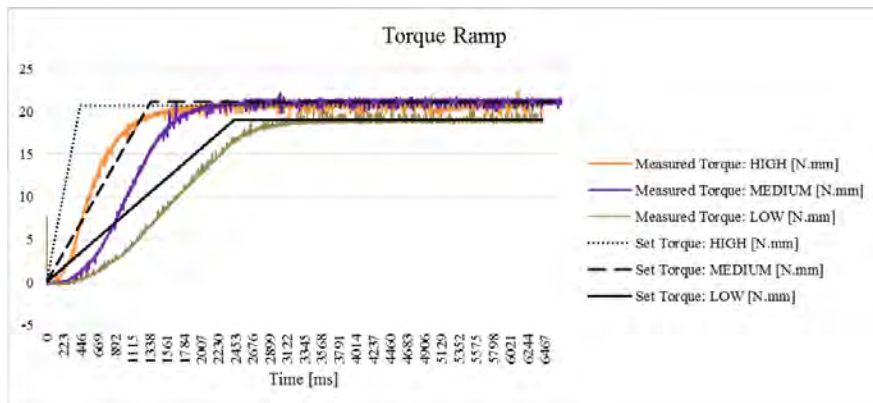
Figure 5.10: Testing the Closing Torque Profiles

5.2.4   Speed and Force Control Switching

The FSM controlling the switching between control modes was tested by commanding the index finger to close onto an object. Initially there was no contact and so speed control would be active. Figure 5.11 shows the speeds, torques, and voltage during the

time leading up to the contact point. Here the speed setting was set to the low intensity option. One important observation is that the FSM only begins to update and monitor the torque once the initial acceleration has complete. This is to avoid a false detection due to high current readings during acceleration.
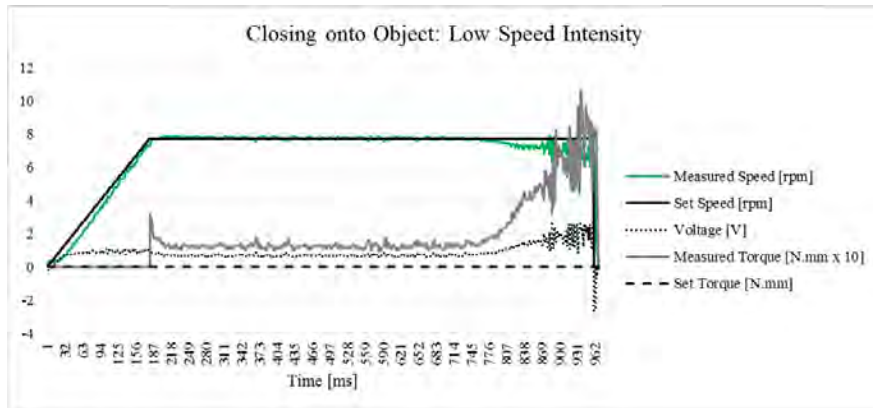
Figure 5.11: Testing Touch Detection while Closing

The torque begins to spike and the speed starts to decrease as soon as the finger touches the object. A touch torque threshold of 40 N.mm was used, and the condition needed to be true for 140 ms. Once the detection is flagged, the set torque and speed are set to zero. At this point the measurement continues onto Figure 5.12. Once the torque and speed reach their zero setpoint, the torque begins to increment while the close command is still active; the low intensity torque option was used. At a torque of approximately 20 N.mm, an open command is given and the torque begins to decrement. This value would then continue to zero before switching back to speed control and the finger beginning to open.
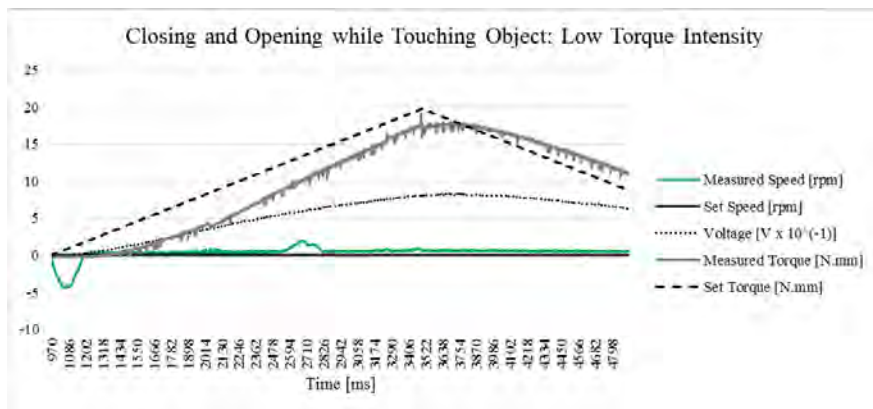
Figure 5.12: Testing Closing and Opening in Torque Control

5.2.5   Positional Control

The close to position command was tested by specifying a close position of 90 °; considered as a full close. The speed profiles were measured for each speed intensity option, and are shown in Figure 5.13. A protractor was used to verify the positional change, which showed all final errors to be less than 5 %.
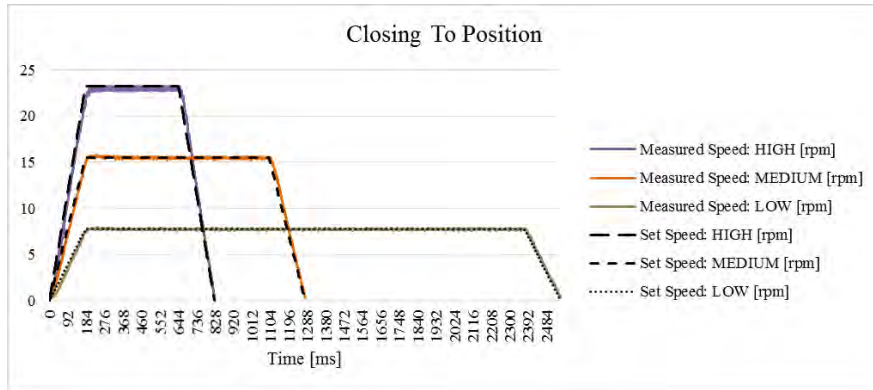
Figure 5.13: Speed Profiles when Closing to a Position

5.2.6   Finger Position Reset

The function of resetting a finger to its zero position was visually verified by commanding the fingers to open continuously. When the zero position was reached, the fingers stopped as predicted. The raw data of the operation would look something similar to that of the closing operation previously shown in Figure 5.12.

5.3   FUNCTIONAL PERFORMANCE

The control testing was focussed on an individual finger, but the hand functionality predominantly considered the ability of the hand as a whole. The results from this testing would be most important to potential amputees because they would want to know how useful it would be for them to use. Dexterity, compliancy, strength, speed, closing time, grasp selection time and mass were measured/tested.

5.3.1   Dexterity

The dexterity represents how well the hand can move its fingers into positions such that various grasps can be achieved. The top ten most frequently used grasps listed by Bullock *et al.* (2013) were used as a baseline for the taxonomy. These were described in section 2.1.3 as consisting of 80 % of the observed grasps in the conducted tests by Bullock *et al.* (2013).

The assembled hand did not have any glove or material placed onto it for grip testing, and so the plastic was the only surface available. The low friction coefficient of the plastic did not allow objects to be held well, but it was planned that material could be placed on the finger in the future to improve the grip ability.

The fingers were only moved into the different positions of the grasps, without the type of shaped object held. The tripod, precision disk, lateral tripod, medium wrap, lateral pinch, and power sphere grasp symbols and corresponding hand attempt are shown in Figure 5.14. Similar images for the thumb–3 finger, light tool, thumb–2 finger and index finger extension are shown in Figure 5.15. The hand grasp symbols were taken from Table 2.1
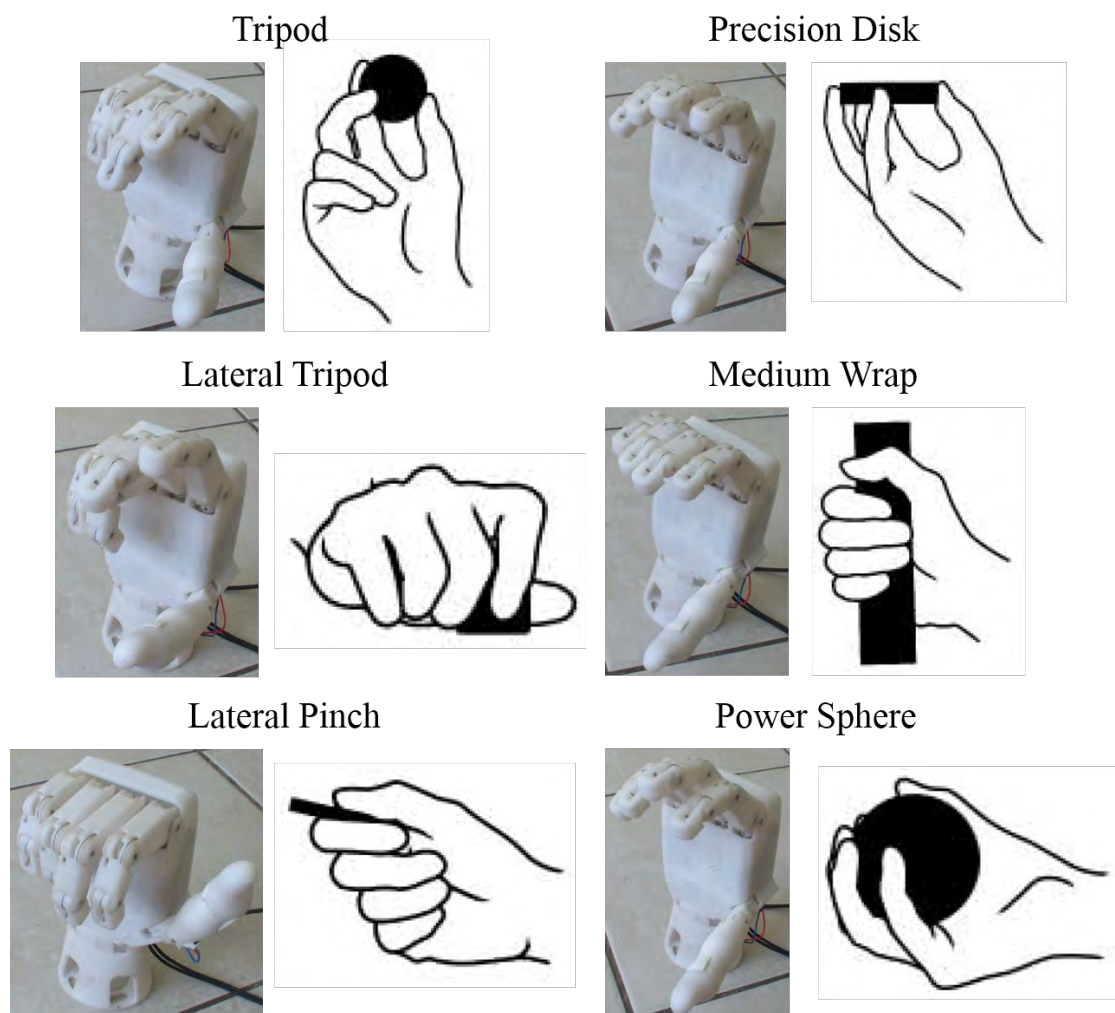
Figure 5.14: Six of the Ten Tested Grasps

The implemented hand grasps were positioned at their starting points, from where they would close onto the type of object to be grasped. This is the reasoning for the most obvious visual differences.

Thumb-3 Finger   Light Tool

Thumb-2 Finger   Index Finger Extension
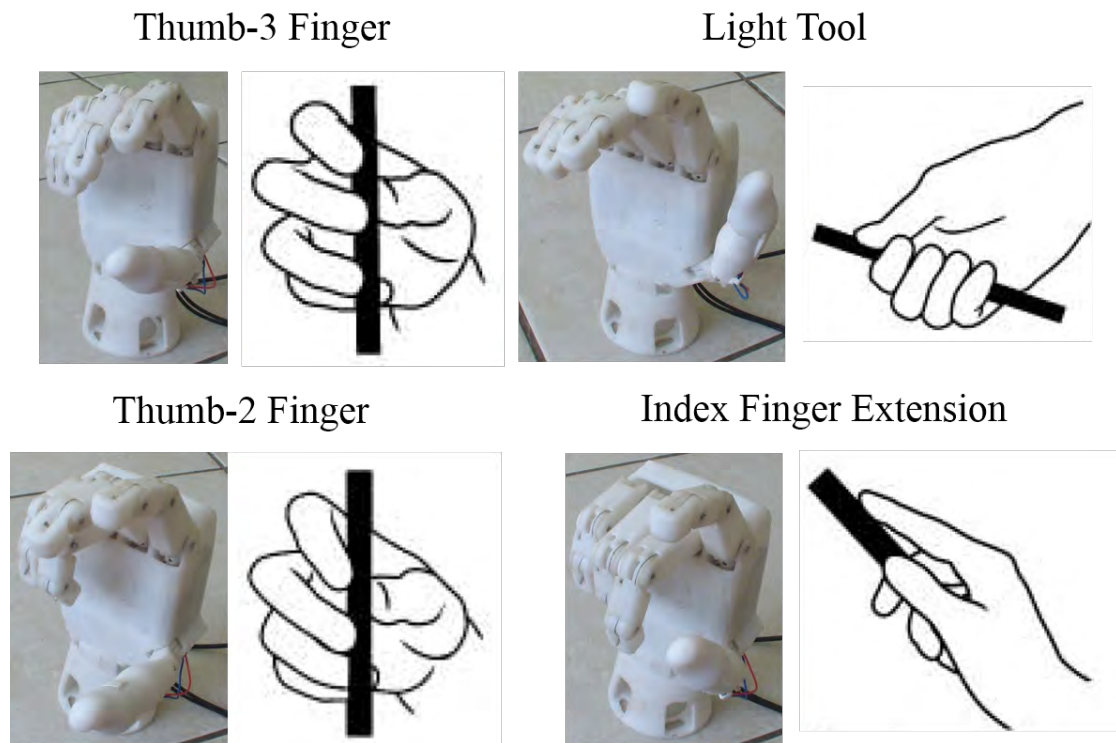
Figure 5.15: Four of the Ten Tested Grasps

On the assembled hand, each adjacent joint of a finger is linked, forcing it to move through a pre–set profile when the MCP joint is rotated. Fingers of the human hand do not have this restriction. This difference can be seen in the precision disk grasp. The small finger MCP joint of the real hand has been rotated, but the other joints are still in extension.

A final disparity is that the Touch Hand II fingers cannot abduct or adduct. Again, the precision disk grasp shows how the human fingers abduct to support the disk at equally spaced points around the edges of the disk. Other than these observed discrepancies, the Touch Hand II generally conforms to the desired grasps.

5.3.2 Compliancy

Compliancy describes the ability of the fingers to wrap around variously shaped objects. Three common household objects were used to check this; an apple, glasses case, and water bottle. The glasses case was grasped in two orientations to vary the finger contact points. Figure 5.16 shows the conducted tests.

The first pose of the grasp holding the glasses cases shows how the fingers are constrained by the linkage mechanism. Holding the apple showed how all three fingers bones of the middle and ring ringer could contact a round object. The thumb was not as successful with conforming to the objects shape. Only the MCP joint was available to the thumb when closing onto the object. The distal bone could not rotate for a more stable grasp.

The grasps show how the fingers generally wrapped around the objects such that they
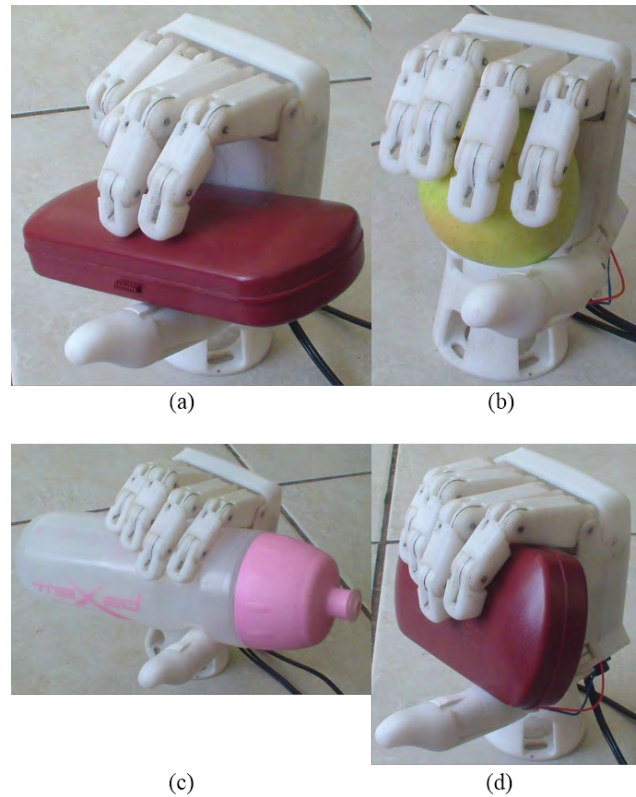
Figure 5.16: Grasping Objects; (a) glasses case pose 1, (b) apple, (c) water bottle, (d) glasses case pose 2

could be held in place. Although the motion profile of the fingers are theoretically fixed, the internal cables used for linkages had an elastic characteristic due to small bends and slack being present after the mechanical assembly. This assisted the fingers with altering their theoretical motion profile. When a finger bone came in contact with the object, the associated joint would first displace due to the wire elasticity before conforming to the linkage motion constraint. This was advantageous to its compliancy.

5.3.3 Finger Strength

Although the torque strength available to each finger was theoretically determined, the actual limit would vary due to friction external to the motor being neglected. The actual maximum output torque of each finger was tested by creating an external load as shown in Figure 5.17.

Here the hand is placed horizontally across a table, resting on the back side. A strap, attached to a water bottle, is fitted onto the index finger close to the MCP joint. The bottle is filled with water and a close command is given. The water quantity is altered until the finger shows only a small amount of movement at its maximum level in torque control. The rated and intermittent limits were tested individually. Using the estimated load force, lever arm distance of 22 mm, and the pulley ratio of 1.56, the load bearing torques supplied at the motor output shafts were calculated.

Figure 5.17: Finger Load Test (Top View)

Table 5.3: Finger Load Test Values: Useful Torque Supplied at Motor Output Shaft

Finger	Rated Torque [N.mm]	Intermittent Torque [N.mm]
Index	74	112
Middle	76	114
Ring	72	117
Small	78	111

5.3.4   Grip Strength

Two tests were performed to check the combinational finger grip strength of the hand. These included the hook (or medium wrap) grasp and the lateral (or lateral pinch)grasp. A similar set–up to the finger strength test was used.

The medium wrap load test was done similarly to the finger load test, except the strap was wrapped over the four fingers used in a hook grasp. The index, middle, ring, and small fingers evenly held the load in this grasp, resulting in the maximum load for the continuous and intermittent case being 4080 g (40.0 N) and 6175 g (60.6 N), respectively, at a lever arm distance of 11.5 mm.

The lateral pinch test was done by placing the strap of the connected bottle between the thumb tip and hand, using the lateral pinch grasp. This held 540 g (rated) and 817 g (intermittent).

5.3.5   Closing Time

The closing time of the hand was implicitly measured during the positional control testing of section 5.2.5. In Figure 5.13 the "HIGH" speed measurement is for a close position of 90°, which was considered a complete close. This was done within 826 ms, 174 ms faster than the goal of 1 s.

5.3.6   General Operation

The reliable operation of repeated functions was necessary to ensure commands did not have to be redone to produce the desired action. The motion of the action should also be similar for every repetition. In some instances this became a problem.

When changing between grasps, the fingers would all simultaneously reset to their zero positions before performing their individual close to position actions. Sometimes five of the six fingers would reset themselves, but one finger would not reset until the others had reached their zero positions. Similarly, when closing to position, there were times when one finger would only begin to close once the others had completed. There were cases similar to this every five to ten commands.

One likely cause is the susceptibility of the electronics to EMI. The current measurement circuit is based on a method that is known for its noise problems, as described in section 3.5.2, and the emf circuit does not have any passive analogue filtering. The operation reliability would improve if more EMI barriers were implemented. The high–side current measurement method could be used, and capacitors could be placed into the emf circuit.

5.3.7   Mass

The mass of the hand, including the electronics and the wrist was measured to be 486 g. This did not include the amputee socket.

5.3.8   Amputee Trial

Feedback from an amputee trying on the hand and gripping objects was possible once the hand was completed. A willing amputee, who lost both hands from an electrical accident, was able to fit the hand with the custom made socket, shown in Figure 5.18.

Figure 5.18: Amputee Trying on the Touch Hand II

The same amputee tested the first version of the hand, the Touch Hand I. He instantly noticed the difference in weight, being lighter in this version. He was happy to see that

the design was more aesthetically appealing and had a human–like form factor. One improvement that he would like was to give the fingers a rougher and softer surface to grip objects more reliably.

5.4 CHAPTER SUMMARY

Testing of the electronics, control system, and overall functioning of the hand was completed. A vero–board based circuit was specifically made for tests to be conducted, containing a single current and emf circuit connected to the MCU. Characteristics such as dc gain, cut–off frequency, offset voltage, and minimum sampling time were measured.

Control testing considered the step response timing, and ramp input tracking characteristics at first for the speed and torque controller. The speed controller had a 28 ms response time, settling to an error of ± 4 %. The torque controller had a 1106 ms response time, larger than the speed controller, avoiding current spikes and instabilities. Position control was successful by setting the speed profile such that a finger would close to a specific angle from the zero position.

During the functional testing, the hand was able to move to ten important grasp positions with close similarity. It was able to lift 4080 g and 6175 g for the rated and intermittent settings in the hook (medium wrap) grasp, respectively. The closing time was 826 ms and the total mass of the hand was 486 g.

6   RESULTS

After designing and testing, the hand was used for a number of comparisons to evaluate its performance and attributes. Design parameters, the Touch Hand I, and other commercial options were used in the comparisons. The measured design parameters were compared to theoretical estimations, while important overall characteristics were used for comparisons against other prosthetic hands.

6.1   COMPARISON TO PREDICTIONS

Knowing the measured values from the tests, comparisons could be made with the theoretical predictions and specifications. This was done for the current and emf circuits, finger and grip strengths, closing time, and mass of the hand. This helped determine how well the hand was designed.

6.1.1   Current Circuit

The current circuit measurements listed in Table 5.1 were combined with the predicted simulation values of Table 3.11 to create Table 6.1. Errors for each measurement were determined and included in the table, all of which are less than 13 %. The main source of these errors are the 5 % tolerance on the resistors and 15 % tolerance on the capacitors. Other sources include the op–amp bias current and offset voltage. Additionally a sampling time of 1 ms was used in the control software, conforming to the constraint of 1.76 ms by 43 %.

Table 6.1: Comparison of Current Circuit Characteristics

Variable	Simulated Value	Measured Value	Error [%]
H_c [V/V]	31.9	29	9.1
f_{HC} [Hz]	320	283.4	11.4
V_z [V]	3.3	3.45	4.5
f_{s_min} [Hz]	640	566.8	11.4
t_{s_max} [ms]	1.56	1.76	12.8

6.1.2 EMF Circuit

A comparison of the measured and design values related to the EMF circuit were compiled into Table 6.2 by combining values from Table 3.12 and 5.2. The PWM signal managed to align to the setting with a very low error because it was controlled by pulse timing on the MCU. The emf offset voltage error would be due to resistor tolerances, and similarly for the DC gain. These errors would contribute to decreasing the accuracy of the speed measurement.

Table 6.2: Comparison of EMF Circuit Related Values

Variable	Designed	Measured	Error [%]
H_{emf} [V/V]	0.62	0.65	4.8
V_{emf_offset} [V]	1.65	1.6	3.0
f_{PWM} [kHz]	46.875	46.73	0.31

6.1.3 Finger Strength

From Table 5.3, the measured motor torques have average rated and intermittent values of 75 N.mm and 113 N.mm, respectively. The motor torque requirements of Table 3.1 have a safety factor, S_L, embedded within their values. Reversing the application of this factor (2.5) through division, gives the uncompensated requirements of 60 N.mm (rated) and 81.2 N.mm (intermittent). Comparing these to the measurements shows they exceed the requirements by 15 N.mm (25 %) and 31.8 N.mm (39 %) for the rated and intermittent values, respectively.

6.1.4 Grip Strength

The hand grip strength test considering the hook (medium wrap) grasp was used for the design specifications on Table 1.2, given as 3.4 kg for the continuous case and 4.6 kg for the intermittent case. The measured values were 4080 g (rated) and 6175 g (intermittent), higher than the specifications by 20 % and 34 %, respectively.

6.1.5 Closing Time & Mass

The closing time and mass of the hand were straight forward comparisons, initially given as specifications in Table 1.2 to be 1.0 s and 500 g, respectively. The final measured values were 826 ms and 486 g, respectively. The actual closing time was a 17.4 % reduction of the goal, while the same can be said for the mass with a 2.8 % reduction.

6.2   TOUCH HAND I & II COMPARISON

A comparison was made between the Touch Hand I and II on their aesthetics, grip strength, closing time, and allowable loads. These comparisons assisted with evaluating the achieved objectives.

6.2.1   Aesthetics

An image of each hand version was brought together to produce Figure 6.1. The difference is clear, but is emphasized. The electronics of the Touch Hand I are exposed with multiple wires connected at various locations. The fingers have gaps in between them with cables and elastic bands showing. The overall shape is quite rectangular, and so are most of the individual components.

(a)   (b)
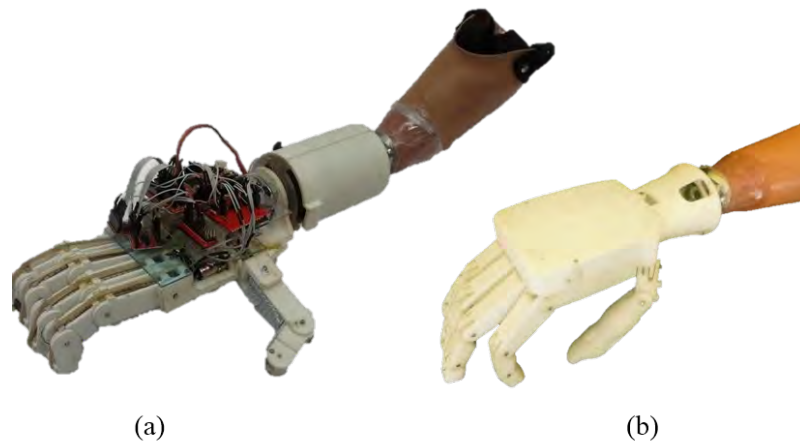
Figure 6.1: Touch Hand Visual Comparison; (a) version I, (b) version II

In comparison, the Touch Hand II has addressed all of these visually degrading sources. Not only are the electronics enclosed by a cover, the circuitry is designed neatly onto one PCB that can be easily removed by unplugging the motors. The fingers do not have any large spaces showing internal mechanisms and have different lengths, as a human hand does. The overall size is more compact and has a human–like form factor.

6.2.2   Grip Strength

Two grip strength values could be compared, that of the hook grip (medium wrap) and the lateral pinch. The bar graph of Figure 6.2 gives a visual comparison of the hook grip strengths. The rated and intermittent values for the Touch Hand I are the same because only one test was done for that version of the hand. The Touch Hand II is stronger with its rated and intermittent values by 105 % and 211 %, respectively.
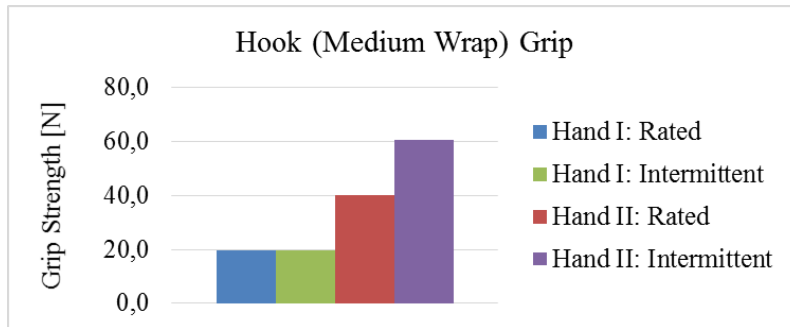
Figure 6.2: Hook Grip Strength Comparison

The bar graph of Figure 6.3 gives a similar comparison, but for the lateral pinch grip. Again, the first version of the hand only had one strength setting for this grip. The rated and intermittent values of the second version were greater by 43 % and 116 %, respectively.
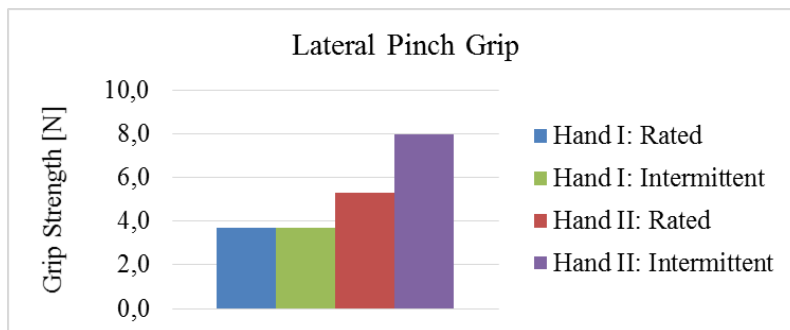
Figure 6.3: Lateral Pinch Grip Strength Comparison

6.2.3 Closing Time

The closing time was one of the major improvements on the first version, with the new value of 0.826 s giving a 58.7 % reduction of the 2.0 s for the first hand. This difference is emphasized by the graph of Figure 6.4.
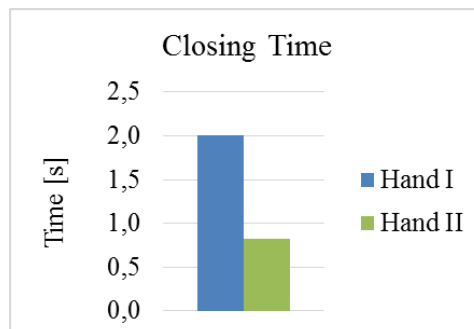
Figure 6.4: Closing Time Comparison

6.2.4 Mass

Although the new version used more power motors that were larger and heavier than the those used before, the combination of the compact shape, optimised usage of plastic, and PCB based circuitry resulted in a lower mass. Figure 6.5 shows that the difference is not substantial, yet still an improvement by a 10 % reduction.
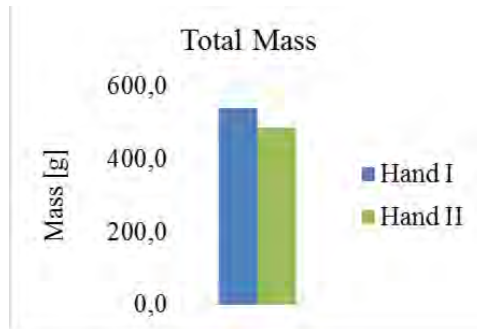
Figure 6.5: Closing Time Comparison

6.2.5 Allowable Loads

A FEA simulation was done on both versions of the hand, however only loading on the palm was considered for the first version. Finger loads were also accommodated for in the second hand. The bar graph of Figure 6.6 gives a summary of the loads and resulting safety factors for each hand. Not only does the new design hold a palm load 3.83 times larger than the first, it also has a higher safety factor.
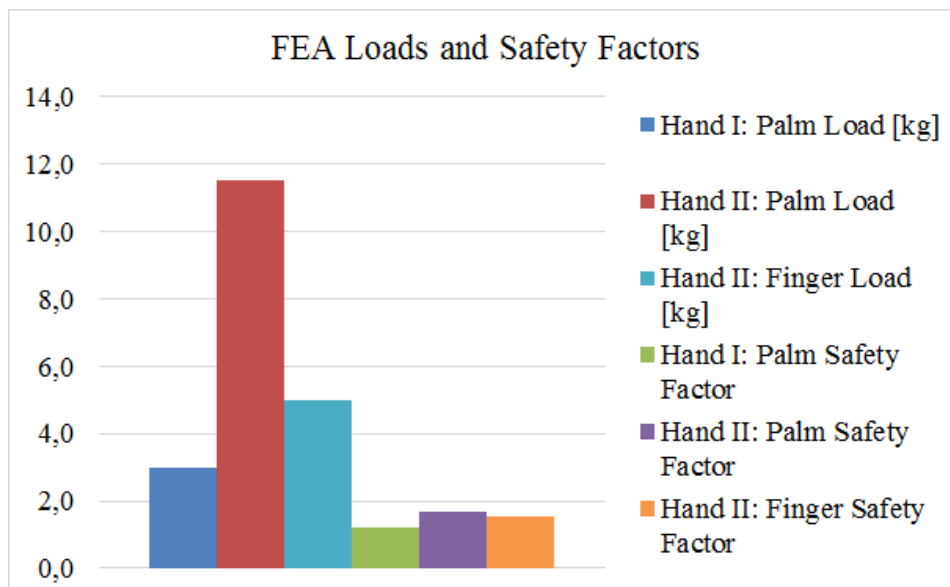
Figure 6.6: FEA Load Comparison

6.2.6 Costs

Unlike the Touch Hand I only having a materials cost estimation, the second version also took into account labour, and electricity; other direct costs were not included. Cost estimations were based on the assumption that the hand would be manufactured in South Africa.

Every used item name, quantity and cost was listed for the materials (See Table B.1 in Appendix B). For labour, the assembly/manufacturing tasks required to be done by a person were identified. Task times were estimated and pay rates were divided by skilled (R 250/hr) and unskilled (R 100/hr) required labour (See Table B.2 in Appendix B). The computer and 3–D printer were considered for direct electricity usage, based on a \$ 131.46 c/kWh cost (See Table B.3 in Appendix B).

All the costs were totalled and summarised into Table 6.3. van der Riet (2014) presented the total materials cost of the Touch Hand I as \$ 1000, which was equivalent to approximately R 10,000 at that time. From the summary, the Touch Hand II has saved R 2,150 on materials, a 21.5 % reduction.

Table 6.3: Summary of Estimated Direct Manufacturing Costs

Item	Cost
Materials	\$ 635.14 (R 7850.36)
Labour	\$ 606.39 (R 7495.00)
Electricity	\$ 2.07 (R 25.56)
Total	\$ 1243.60 (R 15370.91)

6.3 COMPARISON WITH COMMERCIAL OPTIONS

All the features of the considered commercial hands, previously listed in Table 1.1, were combined with those of the Touch Hand I (van der Riet, 2014) and II to produce Table 6.4. This was used to evaluate how well the new Touch Hand compared to other options available to an amputee. The best value of all the hands is highlighted in bold for each feature.

Table 6.4: Comparison Summary of the Touch Hand II against the Touch Hand I and Commercially Available Prostheses

Feature	i-limb Ultra Revolution (Touch Bionics, 2013a)	Michelangelo (Ottobock, 2014)	Bebionic3 (RSLSteeper, 2013b)	Touch Hand I	Touch Hand II
Power Grip Srength[1] (N)	136	70	**140.1**	19.5	60.6
Lateral (Lateral Pinch) Grip Strength[2] (N)	35	**60**	26.5	3.7	8.0
Hook (Medium Wrap) Grip Load (Passive)[3] (kg)	**90**	n/a	45	8	6.175
Finger Hook Load[4] (kg)	**32**	n/a	25	n/a	1.54
Closing Time (s) - Power Grip	1.2	n/a	1.0	2.0	**0.826**
Grip Patterns	**24**	7	14	19+	Depends on control (10 were tested)
Control	2 MES channels	2 MES channels	2 MES channels	2 MES channels	Myoelectric control to be added (Currently via PC)
Weight with Wrist (g)	515	600	698	540	**486**
Cost ($) (van der Riet, 2014)	40,000	75,000	35,000	1,000 (materials)	**1,244** (direct manufacturing costs)

1. Thumb opposing other four fingers, closing into the palm; 2. Thumb closes onto the side of the index finger; 3. Partially closed power grip position; 4. Partially closed individual finger.

As previously mentioned, the strength of the new Touch Hand has improved in comparison to the first version, however the strength values are still not on par with the commercial options. The passive hook grip load of the Touch Hand I is higher than the second version because the latter hand did not use self–locking mechanisms for the fingers. The control of the Touch Hand II was performed via a PC, but the electronics were designed to support the addition of myoelectric control.

Three features of the Touch Hand II out perform the other hands. That is the closing time, weight, and cost. It is the only one with a closing time less than 1.0 s, with a value of 0.826 s it is 0.174 s faster than the Bebionic 3. Similarly with the weight, it is 29 g less than the i-limb Ultra Revolution, the only hand below 500 g. The Touch Hand II cost is highlighted because its materials cost is $ 174 less than the first version, and the direct manufacturing cost is less than other commercial retail prices. A more comprehensive cost breakdown that includes manufacturing, profit, and a retail price would be needed to make a more realistic cost comparison. At this point the manufacturing cost show potential for a retail price lower than the other commercial options.

Additionally the Touch Hand II has aesthetics that are comparable to the commercial hands. Its colour can be changed by using a different colour plastic filament during printing. It does not have a realistic glove to slide on at this point, like the commercial hands, but this can be added.

6.4 CHAPTER SUMMARY

Measured values were compared to predictions and desired specifications to verify whether they were satisfactory. Errors in the range of 0.31 – 12.8 % were determined for the current and emf circuitry by making comparisons to design values, and were mainly due to component tolerances, op–amp bias currents and offset voltages. Grip strength tests resulted in values 20 to 30% higher than the desired specifications. The closing time was 826 ms, a 17.4 % reduction compared to the 1.0 s goal. The total mass was 486 g, 14 g less than the desired specification of 500 g. Although errors were detected, the specifications were still satisfied.

The Touch Hand II outperformed the first version of the hand with every comparison; aesthetics, grip strength, closing time, mass, allowable loads, and cost. When compared to commercial options, much improvement on the grip strength is needed, but the closing time, weight, and cost were the best features out of all the hands.

7   DISCUSSION

After a lengthy concept, detailed design, and testing process, the initial objectives for this research needed to be re–considered to evaluate whether they had been achieved. The objectives are re–iterated before providing references to detailed content to support the evaluation.

7.1   EVALUATION OF OBJECTIVES

The objectives aimed to answer the question, "Can further improvements be made on the Touch Hand I to create a low cost alternative to commercially available prosthetic hands?", and were listed as follows:

1. improving aesthetics; by creating a compact mechanical hand design with self-contained electronics with a human form-factor.

2. a left and right hand design should be manufacturable with one electronic board design that is interchangeable between the two.

3. the electronics should be able to support future sensory and control upgrades/additions; specifically temperature and vibration sensing, two vibration motors for haptic feed-back, and two channel myoelectric control.

4. implementing intuitive grip force, speed, and hand grasp selection control through simulated amputee commands from a computer.

5. improved functional performance; by reducing the hand closing time, increasing the maximum gripping force, decreasing the mass, and increasing the maximum allowable loads.

6. maintaining the materials cost below $ (US) 1000 (R 12 225,25).

Each of these are referred to the work accomplished in order to prove that they were achieved.

7.1.1   Objective 1

The aesthetic improvement was considered in section 6.2.1, showing that the hand had a clean look with enclosed electronics. All internal mechanical mechanisms could not be seen

externally. Just like a human hand, each finger had different dimensions. The dimensions of the hand were compared against human data from the ANSUR database in section 2.3.6.2, showing that the Touch Hand II had values in the $90 - 100^{th}$ range of males. This means the dimensions fit within the data range, having a human form–factor, but ideally they would sit closer to the 50th percentile values.

7.1.2 Objective 2

This objective was addressed in the mechanical and electronic design chapters. Section 2.3.6.9 explained how the left hand model of Figure 2.26 was created before mirroring necessary parts to create a right hand model. The mirrored parts were used to create a physical assembly of the right hand in Figure 2.40. Just as the electronics board could fit into the left hand model of Figure 3.19, the manufactured PCB could fit into the physically assembled right hand of Figure 3.22.

7.1.3 Objective 3

During the selection process of the microcontroller in section 3.3, the basic functionality of the hand and future upgrades were considered. The minimum requirements of Table 3.5 assumed the temperature and vibration sensing to each use one analogue input channel, the two channel EMG control to use two analogue inputs, and the haptic feedback motors to each use one digital I/O pin. The selected MCU, Teensy 3.1, exceeded these pin requirements by having an additional 20 digital I/O pins and 4 analogue input channels. With the additionally available pins, the upgrades can be more flexible in design and pin usage.

7.1.4 Objective 4

A detailed description of the developed GUI for user command emulation was covered in section 4.2. Grip force could be controlled by the length of time the close button was pressed, while the hand was in contact with an object. The torque intensity setting would change this timing. The speed intensity setting allowed selective speed control. Not only could one of the ten hand grasps be selected, individual fingers could also be selected. All of the commands send from GUI to the MCU followed a protocol. When EMG control is applied, a function could be created that would decode the myoelectric signals into commands following the same protocol used by the GUI.

7.1.5 Objective 5

A detailed comparison was made between the Touch Hand I and II in section 6.2. The grip strength showed an increase of 105 % and 211 % for the rated and intermittent cases, respectively. The closing time also showed an improvement with a 58.7 % reduction, resulting from a closing time of 0.826 s compared to 2.0 s. The allowable loads have

increased by more than 3.83 times, with a maximum value of 11.5 kg and a safety factor of 1.7.

7.1.6   Objective 6

The costs of the new hand were discussed in section 6.2.6. The materials totalled to $ 635.14, saving $ 364.86 from the maximum value of $ 1000. Labour and electricity costs were also included, and can be used for future comparisons and estimations.

7.2   CHAPTER SUMMARY

The research objectives were re–iterated for evaluation. Specific references to previous chapter sections were used to show what had been done to achieve each objective. All objectives were reached satisfactorily.

8   CONCLUSION

Transradial amputees considering purchasing a commercial myoelectric prosthetic hand have to overcome a major cost barrier. Popular commercial hands are available in the $ (US) 30, 000 to $ (US) 50, 000 price range, and this is excluding the custom socket and rehabilitation costs. The Touch Hand I was the first attempt at producing a functionally equivalent, but lower cost, alternative to the commercial prosthetic hands. The latest effort is the Touch Hand II, which aimed to improve on the first iteration in almost every way. These improvements were set as the objectives for this research.

A number of commercially available myoelectric prosthetic hands were reviewed, including recent technological advancements, to evaluate the ideal feature performance of the new hand. Problems with the first Touch Hand were identified to form a list of objectives. The anatomy of the human hand was used to understand its functionality and to attain inspiration for the internal mechanisms. A grasp taxonomy was considered in an attempt to simplify the most common and useful grasps that could be performed by a prosthetic hand. The final form factor was human–like, having dimensions in the $90 - 100^{th}$ range of males in the ANSUR anthropometric database. The design enclosed all internal mechanisms and electronics for aesthetic appeal. The maximum external loads on the hand were used in FEA simulations, which showed the palm could hold 11.5 kg with a 1.7 safety factor. 3D plastic printing technology assisted with rapid prototyping, fast design changes, lower material mass, and reduced cost. A kinematic analysis of the finger joints showed realistic motion profiles. A detailed motor selection processed was carried out in order to ensure that the hand would have an improved grip strength, closing time, and weight. In the hook grasp the hand held 4080 g (rated load) and 6175 g (intermittent load). The closing time was 0.826 s and the mass was 486 g.

A custom PCB was designed and manufactured to fit inside the cover of the hand. A hardware architecture was used that had an MCU to handle the position, speed, and torque control of six brushed dc motors. This was based on sensorless methods that reduced sensor costs. The back–emf of the motors was used for speed and position estimation. A low side h–bridge ground resistor was used in conjunction with an op–amp based amplifier for current and torque estimation. An MCU was selected that enabled future additions for myoelectric control, and sensory feedback. Although errors were present, they were below 15 %, and were considered satisfactory.

The command control of the hand was done from a Visual Basic based GUI on a PC, connected through serial communication. This enabled testing all the grasp types and

individual finger functions. By using a finite state machine, a complex close action could be performed that switched between speed and grip force control depending on whether the fingers were in contact with an object. Position control was achieved by controlling the speed profile, and required a zero position reset for each new grasp change. Speed intensity options change the maximum speed of the fingers, while torque intensities change how fast the grip force would change during an open or close command. C++ was used on the MCU to create an upgradeable software architecture, such that myolelectric control and sensors could easily be added. A user command protocol was developed such that commands from decoded EMG signals could easily be given to the hand.

The Touch Hand II was compared against the first version and other commercial prostheses to evaluate the objectives, of which all were satisfied. The shape and form was more realistic, and visually appealing. A left and right hand model could be manufactured, with a one interchangeable PCB design. Sensory and myoelectric control upgrades are possible. The graphical user interface was used to emulate an amputee, which showed the intuitive use of close, open, and grasp selection commands. Relative to the first design iteration, the grip strength increased by 211 % for the intermittent loading option, the closing time decreases by 58.7 % with a value of 0.826 s, the mass decrease by 10 %, and the materials cost reduced by 36.5 % with a value of $ 635.14. The closing time, mass, and cost were three attributes that were better than all the considered hands.

Although this design version made large improvements on the first, the grip strength was still weak in comparison to the commercial hands, with one of the measures being 13.7 % of the lowest commercial hand value. With a drastic cost reduction, and better closing time and mass values, an increase in grip strength closer to the commercial level would make the Touch Hand II an equivalent low cost option.

Future work would consist of focusing more effort on achieving a higher grip strength, while maintaining similar performance measures. A cosmetic glove would further improve the aesthetic appeal of the hand. Errors of the measurements produced by the PCB circuitry could be improved by investigating alternative methods, such as using a high–side current measurement method instead of the low–side to reduce ground noise problems. The finger drives could use self–locking mechanisms, such as with worm–gears, for high passive loading and to reduce power consumption. A darker shade of plastic could be used for the main hand components to minimise dirt marks. To test the hands full potential, myoelectric control and sensory feedback should be integrated and tested by an amputee.

BIBLIOGRAPHY

2 Brothers Hobby, LLC (nd). Brushed dc motor anatomy. Available at: `http://2bfly.com/assets/DC-Motor-Anatomy-sm.png`, [2015, April 27].

Adee, S. (2008). Dean kamen's "luke arm" prosthesis readies for clinical trials. *IEEE Spectrum*. Available online: `http://spectrum.ieee.org/biomedical/bionics/dean-kamens-luke-arm-prosthesis-readies-for-clinical-trials`.

Allegro MicroSystems (2013). A4973 full-bridge pwm motor driver. Available at: `www.allegromicro.com/~/Media/Files/Datasheets/A4973-Datasheet.ashx`, [2015, May 12].

American Society for Surgery of the Hand (2006*a*). Hand movement. Available online: `http://rochesterhandcenter.com/education/images/conditions/Movement1.jpg`, [2014, November 21].

American Society for Surgery of the Hand (2006*b*). Thumb movement. Available online: `http://rochesterhandcenter.com/education/images/conditions/Movement2.jpg`, [2014, November 21].

Andrianesis, K. and Tzes, A. (2008). Design of an anthropomorphic prosthetic hand driven by shape memory alloy actuators. In: *Proceedings of the 2nd Biennial IEEE/RAS-EMBS International Conference on Biomedical Robotics and Biomechatronics*. IEEE, Scottsdale, AZ, USA.

Baker, B.C. (1999). Anti-aliasing, analog filters for data acquisition systems. Available at: `ww1.microchip.com/downloads/en/AppNotes/00699b.pdf`, [2014, December 3].

Baker, B.C. (2003). Select the right operational amplifier for your filtering circuits. Available at: `ww1.microchip.com/downloads/en/DeviceDoc/adn003.pdf`, [2014, December 4].

Bates, S.J., Laurencin, C.T. and Chang, J. (2013 April). Flexor tendon anatomy. *Medscape*. Available online at: `http://emedicine.medscape.com/article/1245236-overview`.

Belter, J.T. and Dollar, A.M. (2011). Performance characteristics of anthropomorphic prosthetic hands. In: *Rehabilitation Robotics (ICORR), 2011 IEEE International Conference on*, vol. 29, pp. 1–7. IEEE.

Bowman, C. (2009). Rotary encoder selection: A step by step guide. Available at: `http://www.trelectronic.com/Training/Rotary%20Encoder%20Selection%20Guide.pdf`, [2014, November 8].

Buchmann, I. (2010). What's the best battery. Available at: `http://batteryuniversity.com/learn/article/whats_the_best_battery`, [2015, May 26].

Bullock, I.M., Zheng, J.Z., Rosa, S., Guertler, C. and Dollar, A.M. (2013). Grasp frequency and usage in daily household and machine shop tasks. *Haptics, IEEE Transactions on*, vol. 6, no. 3, pp. 296–308.

Carozza, M.C., Suppo, C., Sebastiani, F., Massa, B., Vecchi, F., Lazzarini, R., Cutkosky, M.R. and Dario, P. (2004). The spring hand: Development of a self-adaptive prosthesis for restoring natural grasping. *Autonomous Robots*, vol. 16, pp. 125–141.

Chapman, S.J. (2005). *Electric Machinery Fundamentals*. 4th edn. McGraw-Hill, New York.

Cornerstone Robotics (2015). Pulse width modulation (pwm). Available at: `http://www.cornerstonerobotics.org/curriculum/lessons_year2/erii21_motor_control_pwm.pdf`, [2015, May 12].

Cutkosky, M.R. (1989 June). On grasp choice, grasp models, and the design of hands for manufacturing tasks. *IEEE TRANSCATIONS ON ROBOTICS AND AUTOMATION*, vol. 5, no. 3, pp. 269–279.

Dalley, S.A., Wiste, T.E., Withrow, T.J. and Goldfarb, M. (2009 June). Design of a multifunctional anthropomorphic prosthetic hand with extrinsic actuation. *IEEE/ASME TRANSACTIONS ON MECHATRONICS*.

Doshi, R., Yeh, C. and LeBlanc, M. (1998). The design and development of a gloveless endoskeletal prosthetic hand. *Journal of rehabilitation research and development*, vol. 35, pp. 388–395.

eOrthopod (nd). Hand anatomy: A patient's guide to hand anatomy. Available at: `http://www.eorthopod.com/content/hand-anatomy`, [2014, September 21].

Faulhaber (2015). Drive systems. Available at: `http://www.micromo.com/ecatalog/index.html#/0`, [2015, April 28].

Feix, T., Pawlik, R., Schmiedmayer, H.-B., Romero, J. and Kragic, D. (2009). A comprehensive grasp taxonomy. In: *Robotics, Science and Systems: Workshop on Understanding the Human Hand for Advancing Robotic Manipulation*, pp. 2–3.

Franklin, G.F., Powell, J.D. and Naeini, A.E. (2010). *Feedback Control of Dynamic Systems*. Sixth edn. Pearson, Upper Saddle River, New Jersey, 07458.

Gaiser, I.N., Pylatiuk, C., Schulz, S., Kargov, A., Oberle, R. and Werner, T. (2009). The fluidhand iii: A multifunctional prosthetic hand. *JPO: Journal of Prosthetics and Orthotics*, vol. 21, no. 2, pp. 91–96.

Green, S. (1998). Adc input buffer and protection techniques. Available at: `www.cirrus.com/en/pubs/appNote/an20.pdf`, [2014, December 1].

Guizzo, E. (2014). Dean kamen's "luke arm" prosthesis receives fda approval. *IEEE Spectrum*. Available online: `http://spectrum.ieee.org/automaton/biomedical/bionics/dean-kamen-luke-arm-prosthesis-receives-fda-approval`.

Helms, T. (2011). Typical brushed motor in cross-section. Available at: `https://experimentalev.files.wordpress.com/2011/03/dc-motor-parts-6.jpg?w=300\&h=217`, [2015, April 27].

Jazar, R.N. (2010). *Theory of Applied Robotics*. 2nd edn. Springer, New York.

Jiang, N., Dosen, S., Müller, K. and Farina, D. (2012). Myoelectric control of artificial limbs - is there a need to change focus? *IEEE Signal Processing Magazine*. Available online: `http://lifesciences.ieee.org/images/pdf/092012-myoelectric.pdf`.

Kamikawa, Y. and Maeno, T. (2008). Underactuated five-finger prosthetic hand inspired by grasping force distribution of humans. In: *Intelligent Robots and Systems, 2008. IROS 2008. IEEE/RSJ International Conference on*, pp. 717–722. IEEE.

Kargov, A., Pylatiuk, C., Martin, J., Schulz, S. and Döderlein, L. (2004). A comparison of the grip force distribution in natural hands and in prosthetic hands. *Disability & Rehabilitation*, vol. 26, no. 12, pp. 705–711.

Kargov, A., Pylatiuk, C., Oberle, R., Klosek, H., Werner, T., Roessler, W. and Schulz, S. (2007). Development of a multifunctional cosmetic prosthetic hand. In: *Rehabilitation Robotics, 2007. ICORR 2007. IEEE 10th International Conference on*, pp. 550–553. IEEE.

Kurichi, J.E., Bates, B.E. and Stineman, M.G. (2010). Amputation. *International Encyclopedia of Rehabilitation*. Available online: `http://cirrie.buffalo.edu/encyclopedia/en/article/251/`.

Kyberd, P.J., Light, C., Chappell, P.H., Nightingale, J.M., Whatley, D. and Evans, M. (2001 April). The design of anthropomorphic prosthetic hands: A study of the southampton hand. *Robotica*, vol. 19, no. 6, pp. 593–600 doi:10.1017/ S0263574701003538.

Kyberd, P.J., Wartenberg, C., Sandsjö, L., Jönsson, S., Gow, D., Frid, J., Almström, C. and Sperling, L. (2007). Survey of upper-extremity prosthesis users in sweden and the united kingdom. *JPO Journal of Prosthetics and Orthotics*, vol. 19, no. 2.

Laursen, L. (2014). Amputee successfully feels prosthetic grip strength via arm electrodes. *IEEE Spectrum*. Available online: `http://spectrum.ieee.org/tech-talk/biomedical/bionics/sensitive-prosthetic-hand-gets-a-grip`.

Lepkowski, J. (2003). Motor control sensor feedback circuits. Available at: `http://ww1.microchip.com/downloads/en/AppNotes/00894a.pdf`, [2014, December 3].

Light, C. and Chappell, P. (2000). Development of a lightweight and adaptable multiple-axis hand prosthesis. *Medical engineering & physics*, vol. 22, no. 10, pp. 679–684.

Lippert, L.S. (2011). *Clinical Kinesiology and Anatomy*. 5th edn. F. A. Davis Company, 1915 Arch Street, Philadelphia, PA, USA.

Louisiana State University (2005). How well do dogs and other animals hear? Available at: `http://www.lsu.edu/deafness/HearingRange.html`, [2015, May 14].

Micera, S., Carpaneto, J. and Raspopovic, S. (2010). Control of hand prostheses using peripheral information. *IEEE Reviews in Biomedical Engineering*, vol. 3.

MMG (2001*a*). Hand anatomy, central slip. Available online: `http://www.eorthopod.com/content/hand-anatomy`, [2014, November 20].

MMG (2001*b*). Hand anatomy, extensor hood. Available online: `http://www.eorthopod.com/content/hand-anatomy`, [2014, November 20].

MMG (2003). Hand anatomy, hand bones. Available online: `http://www.eorthopod.com/content/hand-anatomy`, [2014, November 20].

Movellan, J.R. (2010 March). Dc motors. Available at: `mplab.ucsd.edu/tutorials/dc.pdf`, [2014, September 8].

Napier, J.R. (1956 November). The prehensile movements of the human hand. *The Bone & Joint Journal*, vol. 38 B, no. 4, pp. 902–913.

Neamen, D.A. (2007). *Microelectronics: Circuit Analysis and Design*. 3rd edn. McGraw-Hill, 1221 Avenues of the Americas, New York, NY 10020.

Norton, K.M. (2007). A brief history of prosthetics. *inMotion*, vol. 17, no. 7. Available online: `http://www.amputee-coalition.org/inmotion/nov_dec_07/history_prosthetics.html`.

Ottobock (2014). *Michelangelo Technician Product Brochure*. Duderstadt, Germany.

Paradiso, J. (2011). Mas.836: How to bias an op-amp. (Massachusetts Institute of Technology: MIT OpenCourseWare), Available at: `http://ocw.mit.edu/courses/media-arts-and-sciences/mas-836-sensor-technologies-for-interactive-environments-spring-2011/readings/MITMAS_836S11_read02_bias.pdf`, [2014, December 1].

Pasluosta, C.F., Tims, H. and Chiu, A.W.L. (2009 May). Slippage sensory feedback and nonlinear force control system for a low-cost prosthetic hand. *NWPII, American Journal of Biomedical Sciences*. ISSN 1937-9080.

Pololu Corporation (nd). Drv8833 dual motor driver carrier. Available at: `https://www.pololu.com/picture/view/0J3864`, [2015, May 11].

RS Components (nd). Allegro microsystems a4973slbtr-t full bridge motor driver, 16-pin soic w. Available at: `http://img-europe.electrocomponents.com/largeimages/F7532046-01.jpg`, [2015, May 11].

RSLSteeper (2013*a*). bebionic3 precision open grip. Available online: `http://www.wired.com/images_blogs/wiredscience/2012/11/bebionic3-PRECISION-OPEN.jpg`, [2014, September 15].

RSLSteeper (2013*b*). *bebionic3 Technical Information Manual, issue 3*. Leeds, LS10 1BL, UK.

Schulz, S., Pylatiuk, C., Reischl, M., Martin, J., Mikut, R. and Bretthauer, G. (2005). A hydraulically driven multifunctional prosthetic hand. *Robotica*, vol. 23, no. 03, pp. 293–299.

Seeed Technology (nd). Arduino micro. Available at: `http://www.seeedstudio.com/depot/images/product/Arduino%20Micro.jpg`, [2015, May 11].

Simpson, C. (nd). Characteristics of rechargeable batteries. Available at: `www.ti.com/lit/an/snva533/snva533.pdf`, [2015, January 4].

SparkFun Electronics (nd). Teensy 3.1. Available at: `https://cdn.sparkfun.com//assets/parts/9/3/3/8/12646-01a.jpg`, [2015, May 11].

Takeda, H., Tsujiuchi, N., Koizumi, T., Kan, H., Hirano, M. and Nakamura, Y. (2009). Development of prosthetic arm with pneumatic prosthetic hand and tendon-driven wrist. In: *Engineering in Medicine and Biology Society, 2009. EMBC 2009. Annual International Conference of the IEEE*, pp. 5048–5051. IEEE.

Taylor, C.L. and Schwarz, R.J. (1955). The anatomy and mechanics of the human hand. *Digital Resource Foundation for the Orhtotics & Prosthetics Community*, vol. 2, no. 2, pp. 22–35.

The Open Design Lab at Penn State (2014*a*). Background. Available at: `http://openlab.psu.edu/tools/explorer.php`, [2015, April 23].

The Open Design Lab at Penn State (2014*b*). Design tools: Ansur database calculator. Available at: `http://www.openlab.psu.edu/tools/calculators/AnsurDimensionSelect.php`, [2014, October 23].

Tocci, P. (2014). Life hand 2 testing. Available online: `http://spectrum.ieee.org/img/PatriziaTocciLifeHand-2braspopovic7HR-1391613576769.jpg`, [2014, November 15].

Touch Bionics (2013*a*). *i-limb Ultra Revolution Clinical Manual, issue 1.* Mansfield, MA 02048, USA.

Touch Bionics (2013*b*). *i-limb Ultra Revolution Datasheet, issue 2.* Mansfield, MA 02048, USA.

Touch Bionics (2013*c*). *i-limb Ultra Revolution User Manual, issue 1.* Mansfield, MA 02048, USA.

Turpen (nd*a*). Membranous portion of the flexor tendon sheath. [Image]. Available online at: `http://img.medscape.com/pi/emed/ckb/clinical_procedures/1230552-1245236-1572tn.jpg`.

Turpen (nd*b*). Retinacular portion of the flexor tendon sheath (pulley system). [Image]. Available online at: `http://img.medscape.com/pi/emed/ckb/clinical_procedures/1230552-1245236-1571tn.jpg`.

Uchino, K. (1997 October). Piezoelectric ultrasonic motors: overview. *Smart Materials and Structures*, vol. 7, pp. 273–285.

van der Riet, D. (2014). *A Modular Prosthetic Arm with Haptic Interfacing for Transradial/Transhumeral Amputees.* Master's thesis, Mechanical Engineering, Mechatronics and Robotics Research Group, Bio-Engineering Unit, University of KwaZulu-Natal, Durban, South Africa.

Wang, K. (1996). The use of titanium for medical applications in the usa. *Materials Science and Engineering: A*, vol. 213, no. 1, pp. 134–137.

Xu, Z., Todorov, E., Dellon, B. and Matsuoka, Y. (2011). Design and analysis of an artificial finger joint for anthropomorphic robotic hands. In: *Robotics and Automation (ICRA), 2011 IEEE International Conference on*, pp. 5096–5102. IEEE.

Zhao, D., Jiang, L., Huang, H., Jin, M., Cai, H. and Liu, H. (2006). Development of a multi-dof anthropomorphic prosthetic hand. In: *Robotics and Biomimetics, 2006. ROBIO'06. IEEE International Conference on*, pp. 878–883. IEEE.

Zollo, L., Roccella, S., Guglielmelli, E., Carrozza, M.C. and Dario, P. (2007 August). Biomechatronic design and control of an anthropomorphic artificial hand for prosthetic and robotic applications. *IEEE/ASME TRANSACTIONS ON MECHATRONICS*, vol. 12, no. 4, pp. 418–429.

Appendices

A   MOTOR AND GEARBOX DATASHEETS

FAULHABER

DC-Micromotors
Precious Metal Commutation

2,2 mNm

For combination with
Gearheads:
15/10, 15A, 16/7, 16A, 17/1
Encoders:
IE2-1024, IE2-16, IEH2-4096

Series 1717 ... SR

Values at 22°C and nominal voltage		1717 T	003 SR	006 SR	012 SR	018 SR	024 SR	
1	Nominal voltage	U_N		3	6	12	18	24	V
2	Terminal resistance	R		1,07	4,3	17,1	50,1	68,8	Ω
3	Output power	$P_{2nom.}$		1,97	1,96	1,97	1,5	1,96	W
4	Efficiency, max.	$\eta_{max.}$		69	69	70	68	70	%
5	No-load speed	n_0		14 000	14 000	14 000	12 300	14 000	rpm
6	No-load current, typ. (with shaft ø 1,5 mm)	I_0		0,091	0,046	0,023	0,013	0,011	A
7	Stall torque	M_H		5,37	5,34	5,38	4,66	5,36	mNm
8	Friction torque	M_R		0,18	0,18	0,18	0,18	0,17	mNm
9	Speed constant	k_n		4 820	2 410	1 210	709	602	rpm/V
10	Back-EMF constant	k_E		0,207	0,414	0,829	1,41	1,66	mV/rpm
11	Torque constant	k_M		1,98	3,96	7,92	13,5	15,9	mNm/A
12	Current constant	k_I		0,505	0,253	0,126	0,074	0,063	A/mNm
13	Slope of n-M curve	$\Delta n/\Delta M$		2 610	2 620	2 600	2 640	2 610	rpm/mNm
14	Rotor inductance	L		17	65	260	760	1 040	µH
15	Mechanical time constant	τ_m		16	16	16	16	16	ms
16	Rotor inertia	J		0,59	0,58	0,59	0,58	0,59	gcm²
17	Angular acceleration	$\alpha_{max.}$		92	92	92	80	92	·10³rad/s²
18	Thermal resistance	R_{th1} / R_{th2}	4,5 / 27						K/W
19	Thermal time constant	τ_{w1} / τ_{w2}	2 / 210						s
20	Operating temperature range:								
	– motor		-30 ... +85 (optional version -55 ... +125)						°C
	– winding, max. permissible		+125						°C
21	Shaft bearings		sintered bearings		ball bearings		ball bearings, preloaded		
22	Shaft load max.:		(standard)		(optional version)		(optional version)		
	– with shaft diameter		1,5		1,5		1,5		mm
	– radial at 3 000 rpm (3 mm from bearing)		1,2		5		5		N
	– axial at 3 000 rpm		0,2		0,5		0,5		N
	– axial at standstill		20		10		10		N
23	Shaft play								
	– radial	≤	0,03		0,015		0,015		mm
	– axial	≤	0,2		0,2		0		mm
24	Housing material		steel, black coated						
25	Mass		18						g
26	Direction of rotation		clockwise, viewed from the front face						
27	Speed up to	$n_{max.}$	16 000						rpm
28	Number of pole pairs		1						
29	Magnet material		NdFeB						

Rated values for continuous operation								
30	Rated torque	M_N		1,2	2,1	2,1	2,1	2,2	mNm
31	Rated current (thermal limit)	I_N		0,7	0,63	0,32	0,19	0,16	A
32	Rated speed	n_N		10 790	6 540	6 570	4 570	6 540	rpm

Note: Rated values are calculated with nominal voltage and at a 22°C ambient temperature. The R_{th2} value has been reduced by 0%.

Note:

The diagram indicates the recommended speed in relation to the available torque at the output shaft for a given ambient temperature of 22°C.

The diagram shows the motor in a completely insulated as well as thermally coupled condition (R th 2 50% reduced).

The nominal voltage (U_N) curve shows the operating point at nominal voltage in the insulated and thermally coupled condition. Any points of operation above the curve at nominal voltage will require a higher operating voltage. Any points below the nominal voltage curve will require less voltage.

Recommended operation areas (example: nominal voltage 24V)

For notes on technical data and lifetime performance
refer to "Technical Information".
Edition 2014   Page 1/2

© DR. FRITZ FAULHABER GMBH & CO. KG
Specifications subject to change without notice.

Figure A.1: Faulhaber 1717_SR Motor Datasheet

FAULHABER

Planetary Gearheads

0,25 Nm

For combination with
DC-Micromotors
Stepper Motors

Series 15A

	15A	15AC	15AK
Housing material	plastic	plastic	plastic
Geartrain material	plastic	plastic	plastic
Recommended max. input speed for:			
– continuous operation	5 000 rpm	5 000 rpm	5 000 rpm
Backlash, at no-load	≤ 4 °	≤ 4 °	≤ 4 °
Bearings on output shaft	sintered bearings	ceramic bearings	ball bearings
Shaft load, max.:			
– radial (5 mm from mounting face)	≤ 3 N	≤ 10 N	≤ 15 N
– axial	≤ 1 N	≤ 2 N	≤ 5 N
Shaft press fit force, max.	≤ 10 N	≤ 10 N	≤ 10 N
Shaft play			
– radial (5 mm from mounting face)	≤ 0,06 mm	≤ 0,08 mm	≤ 0,09 mm
– axial	≤ 0,25 mm	≤ 0,25 mm	≤ 0,25 mm
Operating temperature range	- 30 ... + 65 °C	- 20 ... + 85 °C	- 30 ... + 85 °C

Specifications									
Number of gear stages		1	2	3	3	4	5	5	6
Continuous torque	mNm	50	100	100	150	200	200	250	250
Intermittent torque	mNm	100	200	200	300	400	400	400	400
Mass without motor, ca.	g	4	5	5	5	6	6	6	7
Efficiency, max.	%	87	78	68	67	62	55	52	49
Direction of rotation, drive to output		=	=	=	=	=	=	=	=
Reduction ratio [1]	Code B [2]		14:1	52:1		249:1	896:1		3 225:1
(rounded)			19:1	69:1					
	Code A [2]	5,33:1	28:1	102:1	152:1	369:1	1 327:1	2 913:1	4 778:1
						546:1	1 966:1	4 315:1	7 078:1
						809:1			10 486:1
									15 534:1
									23 014:1
L2 [mm] = length without motor [3]		14,1	17,7	21,3	21,3	24,9	28,5	28,5	32,1
L1 [mm] = length with motor 1516A/B...SR		29,9	33,5	37,1	37,1	40,7	44,3	44,3	47,9
1524A/B...SR		37,9	41,5	45,1	45,1	48,7	52,3	52,3	55,9
1624A/B...S		37,9	41,5	45,1	45,1	48,7	52,3	52,3	55,9
1717A/B...SR		31,1	34,7	38,3	38,3	41,9	45,5	45,5	49,1
1724A/B...SR		38,1	41,7	45,3	45,3	48,9	52,5	52,5	56,1
AM1524...-70		30,5	34,1	37,7	37,7	41,3	44,9	44,9	48,5

[1] The reduction ratios are rounded, the exact values are available on request or at www.faulhaber.com.
[2] Example of ordering information: 1516 **B** 012 SR + 15A 19:1, not for AM1524.
[3] L2 + 0,7 mm, in combination with 1516A/B...SR and 1524A/B...SR.

Note: These gearheads are available only with motors mounted.
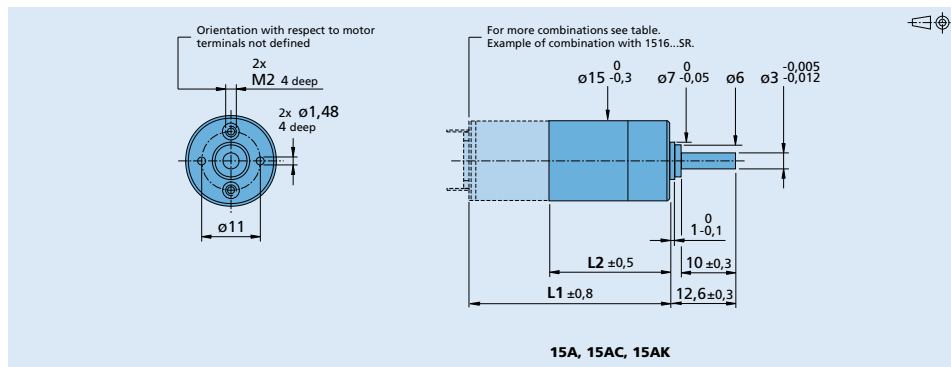
Orientation with respect to motor
terminals not defined

2x
M2 4 deep

2x ø1,48
4 deep

ø11

For more combinations see table.
Example of combination with 1516...SR.

ø15 $^{0}_{-0,3}$ ø7 $^{0}_{-0,05}$ ø6   ø3 $^{-0,005}_{-0,012}$

1 $^{0}_{-0,1}$

L2 ±0,5   10 ±0,3

L1 ±0,8   12,6 ±0,3

15A, 15AC, 15AK

For notes on technical data and lifetime performance
refer to "Technical Information".
Edition 2014

© DR. FRITZ FAULHABER GMBH & CO. KG
Specifications subject to change without notice.

Figure A.2: Faulhaber 15A Gearhead Datasheet

FAULHABER

DC-Micromotors
Precious Metal Commutation

0,5 mNm

1,4 W

Series 1016 ... G

Values at 22°C and nominal voltage		1016 N		003 G	006 G	012 G	
1	Nominal voltage	U_N		3	6	12	V
2	Terminal resistance	R		8,7	19,3	95	Ω
3	Output power	$P_{2nom.}$		0,24	0,44	0,36	W
4	Efficiency, max.	$\eta_{max.}$		63	68	68	%
5	No-load speed	n_0		14 200	18 400	16 500	min^{-1}
6	No-load current, typ. (with shaft ø 0,8 mm)	I_0		0,015	0,01	0,004	A
7	Stall torque	M_H		0,64	0,9	0,82	mNm
8	Friction torque	M_R		0,03	0,03	0,03	mNm
9	Speed constant	k_n		4 948	3 173	1 419	min^{-1}/V
10	Back-EMF constant	k_E		0,202	0,315	0,705	mV/min^{-1}
11	Torque constant	k_M		1,93	3,01	6,73	mNm/A
12	Current constant	k_I		0,518	0,332	0,149	A/mNm
13	Slope of n-M curve	$\Delta n/\Delta M$		22 304	20 342	20 029	min^{-1}/mNm
14	Rotor inductance	L		28	60	310	µH
15	Mechanical time constant	τ_m		9	12,8	10	ms
16	Rotor inertia	J		0,04	0,06	0,05	gcm²
17	Angular acceleration	$\alpha_{max.}$		159	151	165	·10³rad/s²
18	Thermal resistance	R_{th1} / R_{th2}	26 / 56				K/W
19	Thermal time constant	τ_{w1} / τ_{w2}	3,1 / 260				s
20	Operating temperature range:						
	– motor		-30 ... +85 (optional version -30 ... +125)				°C
	– winding, max. permissible		+85 (optional version +125)				°C
21	Shaft bearings		sintered bearings				
22	Shaft load max.:						
	– with shaft diameter		0,8				mm
	– radial at 3 000 min^{-1} (1,5 mm from bearing)		0,5				N
	– axial at 3 000 min^{-1}		0,1				N
	– axial at standstill		20				N
23	Shaft play						
	– radial	≤	0,03				mm
	– axial	≤	0,2				mm
24	Housing material		steel, nickel plated				
25	Mass		6,5				g
26	Direction of rotation		clockwise, viewed from the front face				
27	Speed up to	$n_{max.}$	22 000				min^{-1}
28	Number of pole pairs		1				
29	Magnet material		SmCo				

Rated values for continuous operation							
30	Rated torque	M_N		0,43	0,48	0,5	mNm
31	Rated current (thermal limit)	I_N		0,24	0,17	0,08	A
32	Rated speed	n_N		2 500	5 730	3 750	min^{-1}

Note: Rated values are calculated with nominal voltage and at a 22°C ambient temperature. The R_{th2} value has been reduced by 0%.

Note:

The diagram indicates the recommended speed in relation to the available torque at the output shaft for a given ambient temperature of 22°C.

The diagram shows the motor in a completely insulated as well as thermally coupled condition (R_{th2} 50% reduced).

The nominal voltage (U_N) curve shows the operating point at nominal voltage in the insulated and thermally coupled condition. Any points of operation above the curve at nominal voltage will require a higher operating voltage. Any points below the nominal voltage curve will require less voltage.

Recommended operation areas (example: nominal voltage 12V)
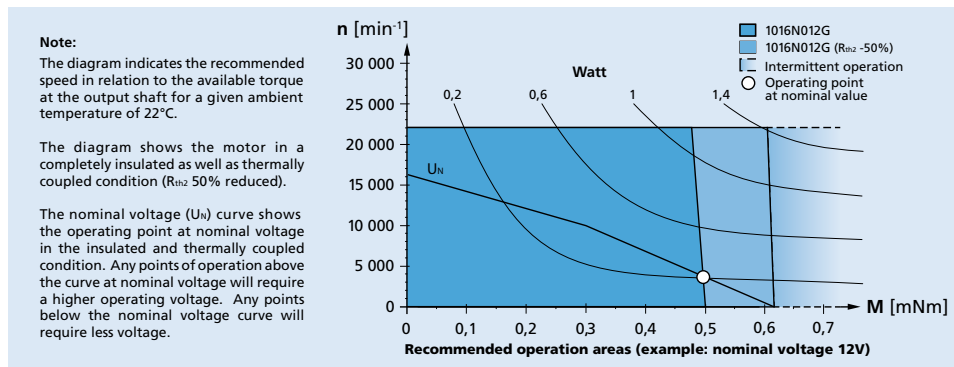
Figure A.3: Faulhaber 1016G Motor Datasheet

FAULHABER

Planetary Gearheads   0,1 Nm

For combination with
DC-Micromotors
Brushless DC-Motors
Stepper Motors

Series 10/1

		10/1	10/1K
Housing material		metal	metal
Geartrain material		steel	steel
Recommended max. input speed for:			
– continuous operation		5 000 rpm	5 000 rpm
Backlash, at no-load		≤ 3 °	≤ 3 °
Bearings on output shaft		sintered bearings	ball bearings, preloaded
Shaft load, max.:			
– radial (5 mm from mounting face)		≤ 1 N	≤ 7 N
– axial		≤ 2 N	≤ 5 N
Shaft press fit force, max.		≤ 10 N	≤ 5 N
Shaft play			
– radial (5 mm from mounting face)		≤ 0,06 mm	≤ 0,04 mm
– axial		≤ 0,1 mm	= 0 mm
Operating temperature range		- 30 ... + 100 °C	- 30 ... + 100 °C

Specifications

		1	2	3	4	5	6
Number of gear stages		1	2	3	4	5	6
Continuous torque	mNm	5	15	54	100	100	100
Intermittent torque	mNm	200	200	200	200	200	200
Mass without motor, ca.	g	6	7	8	10	11	13
Efficiency, max.	%	90	80	70	60	55	48
Direction of rotation, drive to output		=	=	=	=	=	=
Reduction ratio (exact)		4:1	16:1	64:1	256:1	1 024:1	4 096:1
L2 [mm] = length without motor		9,7	12,8	15,9	19,0	22,1	25,2
L1 [mm] = length with motor 0816M...SR		25,6	28,7	31,8	34,9	38,0	41,1
1016M...G		25,4	28,5	31,6	34,7	37,8	40,9
1024M...S		33,4	36,5	39,6	42,7	45,8	48,9
1219M...G		28,4	31,5	34,6	37,7	40,8	43,9
1224M...SR		33,9	37,0	40,1	43,2	46,3	49,4
0824M...B		33,8	36,9	40,0	43,1	46,2	49,3
1028M...B		37,8	40,9	44,0	47,1	50,2	53,3
1218M...B		27,7	30,8	33,9	37,0	40,1	43,2
1226M...B		35,7	38,8	41,9	45,0	48,1	51,2
ADM1220S...-55		27,1	30,2	33,3	36,4	39,5	42,6
AM0820...-10		23,5	26,6	29,7	32,8	35,9	39,0
AM1020...-08		25,6	28,7	31,8	34,9	38,0	41,1
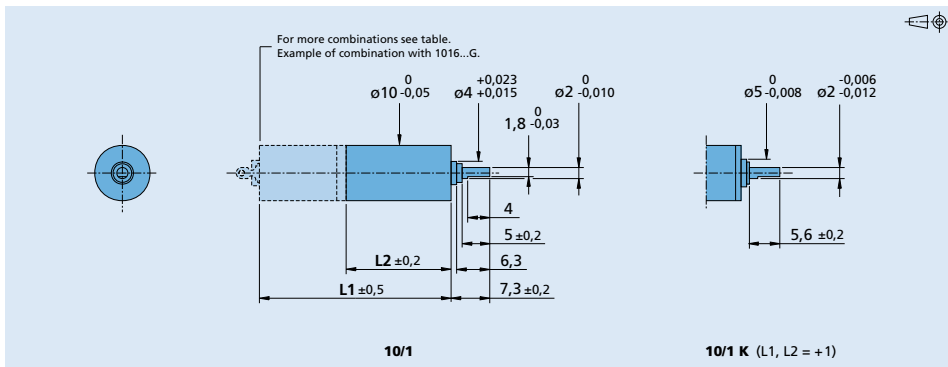
For more combinations see table.
Example of combination with 1016...G.

10/1   **10/1 K** (L1, L2 = +1)

Figure A.4: Faulhaber 10/1 Gearhead Datasheet

A-max 16 ∅16 mm, Precious Metal Brushes CLL, 2 Watt
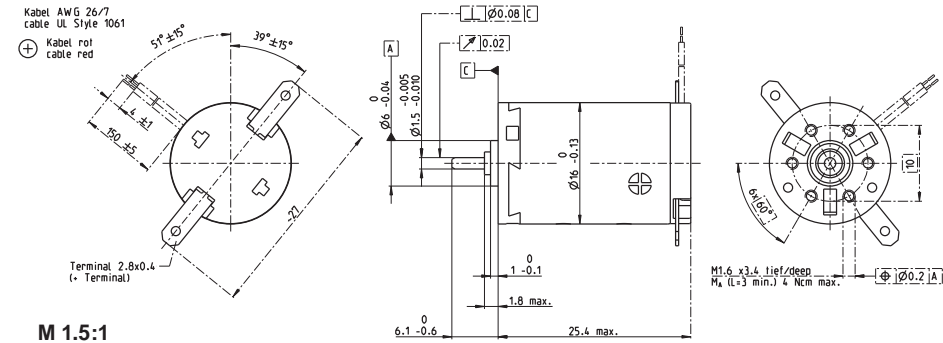
M 1.5:1

maxon *A*-max

■ Stock program
□ Standard program
▨ Special program (on request)

Part Numbers

		110041	**110042**	110043	110044	**110045**	110046	110047	110048	110049	110050
with terminals		110041	110042	110043	110044	110045	110046	110047	110048	110049	110050
with cables		139820	352815	134844	231379	220514	304672	352823	352816	260678	352817

Motor Data

Values at nominal voltage

1	Nominal voltage	V	1.5	3	6	9	12	15	18	21	24	30
2	No load speed	rpm	10800	12300	10100	12300	12300	13200	14100	13700	13800	11400
3	No load current	mA	61.4	38.1	13.9	12.7	9.54	8.57	7.99	6.53	5.83	3.37
4	Nominal speed	rpm	9360	8810	4530	6700	6660	7590	8480	8040	8120	5480
5	Nominal torque (max. continuous torque)	mNm	0.712	1.3	2.22	2.19	2.17	2.17	2.15	2.14	2.11	2.08
6	Nominal current (max. continuous current)	A	0.6	0.6	0.408	0.327	0.243	0.209	0.185	0.153	0.134	0.0864
7	Stall torque	mNm	4.79	4.51	4.03	4.82	4.77	5.16	5.44	5.22	5.12	4.04
8	Starting current	A	3.66	1.97	0.723	0.702	0.52	0.482	0.453	0.362	0.315	0.164
9	Max. efficiency	%	77	75	75	76	76	76	76	76	76	74

Characteristics

10	Terminal resistance	Ω	0.41	1.52	8.3	12.8	23.1	31.1	39.7	57.9	76.2	183
11	Terminal inductance	mH	0.017	0.0519	0.306	0.467	0.831	1.13	1.42	2.05	2.61	6.01
12	Torque constant	mNm/A	1.31	2.29	5.57	6.88	9.17	10.7	12	14.4	16.3	24.7
13	Speed constant	rpm/V	7290	4170	1720	1390	1040	893	795	663	587	387
14	Speed / torque gradient	rpm/mNm	2280	2770	2560	2590	2620	2600	2630	2670	2750	2880
15	Mechanical time constant	ms	25.3	23.8	23.3	23.3	23.3	23.4	23.5	23.4	23.5	23.9
16	Rotor inertia	gcm²	1.06	0.82	0.868	0.859	0.849	0.859	0.852	0.838	0.816	0.793

Specifications

Thermal data
17 Thermal resistance housing-ambient 29.8 K/W
18 Thermal resistance winding-housing 5.5 K/W
19 Thermal time constant winding 3.55 s
20 Thermal time constant motor 165 s
21 Ambient temperature -30…+65°C
22 Max. permissible winding temperature +85°C

Mechanical data (sleeve bearings)
23 Max. permissible speed 19000 rpm
24 Axial play 0.05 - 0.15 mm
25 Radial play 0.012 mm
26 Max. axial load (dynamic) 0.8 N
27 Max. force for press fits (static) 35 N
28 Max. radial load, 5 mm from flange 1.4 N

Mechanical data (ball bearings)
23 Max. permissible speed 19000 rpm
24 Axial play 0.05 - 0.15 mm
25 Radial play 0.025 mm
26 Max. axial load (dynamic) 2.2 N
27 Max. force for press fits (static) 30 N
28 Max. radial load, 5 mm from flange 7.8 N

Other specifications
29 Number of pole pairs 1
30 Number of commutator segments 7
31 Weight of motor 21 g
CLL = Capacitor Long Life

Values listed in the table are nominal.
Explanation of the figures on page 79.

Option
Ball bearings in place of sleeve bearings
Without CLL

Operating Range

Comments

Continuous operation
In observation of above listed thermal resistance (lines 17 and 18) the maximum permissible winding temperature will be reached during continuous operation at 25°C ambient.
= Thermal limit.

Short term operation
The motor may be briefly overloaded (recurring).

—— Assigned power rating

maxon Modular System   Overview on page 20−25

Spur Gearhead
∅16 mm
0.01 - 0.1 Nm
Page 250−253
Planetary Gearhead
∅16 mm
0.1 - 0.6 Nm
Page 254/255
Spindle Drive
∅16 mm
Page 296−298

Recommended Electronics:
ESCON 36/2 DC   Page 342
ESCON Module 50/5   343
ESCON 50/5   344
Notes   22

April 2014 edition / subject to change

maxon DC motor   121

Figure A.5: Maxon A-max 16 EB Motor Datasheet

Planetary Gearhead GP 16 A ∅16 mm, 0.1–0.3 Nm

maxon gear
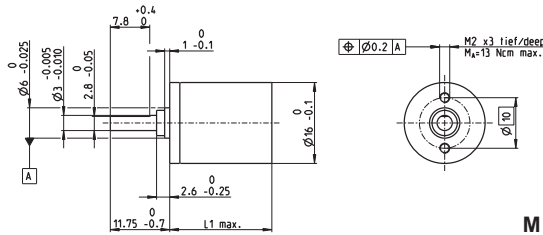
M 1:1

Technical Data

Planetary Gearhead	straight teeth
Output shaft	stainless steel, hardened
Bearing at output	sleeve bearing
Radial play, 6 mm from flange	max. 0.06 mm
Axial play	0.02–0.10 mm
Max. permissible axial load	8 N
Max. permissible force for press fits	100 N
Sense of rotation, drive to output	=
Recommended input speed	< 8000 rpm
Recommended temperature range	-30…+100°C
Extended range as option	-40…+100°C
Number of stages	1 2 3 4 5
Max. radial load, 6 mm from flange	8 N 12 N 16 N 20 N 20 N

- Stock program
- Standard program
- Special program (on request)

Part Numbers / Gearhead Data

		110321	110322	110323	118186	110324	134782	110325	134785
1	Reduction	4.4 : 1	19 : 1	84 : 1	157 : 1	370 : 1	690 : 1	1621 : 1	3027 : 1
2	Reduction absolute	$^{57}/_{13}$	$^{3249}/_{169}$	$^{185193}/_{2197}$	$^{19683}/_{125}$	$^{10556001}/_{28561}$	$^{1121931}/_{1625}$	$^{601692057}/_{371293}$	$^{63950067}/_{21125}$
3	Max. motor shaft diameter (mm)	2	2	2	1.5	2	2	2	2
Part Numbers		118184	134777	134778		134780	118187	134783	134786
1	Reduction	5.4 : 1	24 : 1	104 : 1		455 : 1	850 : 1	1996 : 1	3728 : 1
2	Reduction absolute	$^{27}/_{5}$	$^{1539}/_{65}$	$^{87723}/_{845}$		$^{5000211}/_{10985}$	$^{531441}/_{625}$	$^{285012027}/_{142805}$	$^{30292137}/_{8125}$
3	Max. motor shaft diameter (mm)	1.5	2	2		2	1.5	2	2
Part Numbers			118185	134779		134781		134784	118188
1	Reduction		29 : 1	128 : 1		561 : 1		2458 : 1	4592 : 1
2	Reduction absolute		$^{729}/_{25}$	$^{41553}/_{325}$		$^{2368521}/_{4225}$		$^{135005697}/_{54925}$	$^{14348907}/_{3125}$
3	Max. motor shaft diameter (mm)		1.5	2		2		2	1.5
4	Number of stages	1	2	3	3	4	4	5	5
5	Max. continuous torque (Nm)	0.10	0.15	0.20	0.20	0.25	0.25	0.30	0.30
6	Intermittently permissible torque at gear output (Nm)	0.150	0.225	0.300	0.300	0.375	0.375	0.450	0.450
7	Max. efficiency (%)	90	81	73	73	65	65	59	59
8	Weight (g)	20	23	27	27	31	31	35	35
9	Average backlash no load (°)	1.4	1.6	2.0	2.0	2.4	2.4	3.0	3.0
10	Mass inertia (gcm²)	0.07	0.05	0.05	0.04	0.05	0.05	0.05	0.05
11	Gearhead length L1 (mm)	15.5	19.1	22.7	22.7	26.3	26.3	29.9	29.9

overall length   overall length

maxon Modular System

Overall length [mm] = Motor length + gearhead length + (sensor/brake) + assembly parts

+ Motor	Page	+ Sensor/Brake	Page								
RE 16, 2 W	102			37.9	41.5	45.1	45.1	48.7	48.7	52.3	52.3
RE 16, 2 W	102	MR	315/317	43.6	47.2	50.8	50.8	54.4	54.4	58.0	58.0
RE 16, 3.2 W	103/104			56.0	59.6	63.2	63.2	66.8	66.8	70.4	70.4
RE 16, 3.2 W	104	MR	315/317	61.0	64.6	68.2	68.2	71.8	71.8	75.4	75.4
RE 16, 3.2 W	104	MEnc 13	334	62.1	65.7	69.3	69.3	72.9	72.9	76.5	76.5
RE 16, 4.5 W	105/106			59.0	62.6	66.2	66.2	69.8	69.8	73.4	73.4
RE 16, 4.5 W	106	MR	315/317	64.0	67.6	71.2	71.2	74.8	74.8	78.4	78.4
RE 16, 4.5 W	106	MEnc 13	334	65.2	68.8	72.4	72.4	76.0	76.0	79.6	79.6
A-max 16	121-124			41.0	44.6	48.2	48.2	51.8	51.8	55.4	55.4
A-max 16	122/124	MR	315/317	46.0	49.6	53.2	53.2	56.8	56.8	60.4	60.4
A-max 16	122/124	MEnc 13	334	49.1	52.7	56.3	56.3	59.9	59.9	63.5	63.5
RE-max 17	151-154			41.0	44.6	48.2	48.2	51.8	51.8	55.4	55.4
RE-max 17	152/154	MR	315/317	46.0	49.6	53.2	53.2	56.8	56.8	60.4	60.4
EC 16, 30 W	178			55.6	59.2	62.8	62.8	66.4	66.4	70.0	70.0
EC 16, 30 W	178	MR	318	66.3	69.9	73.5	73.5	77.1	77.1	80.7	80.7
EC-max 16, 5 W	199			39.6	43.2	46.8	46.8	50.4	50.4	54.0	54.0
EC-max 16, 5 W	199	MR	318	46.9	50.5	54.1	54.1	57.7	57.7	61.3	61.3
EC-max 16, 2-wire	200			49.1	52.7	56.3	56.3	59.9	59.9	63.5	63.5

Option Ball Bearing
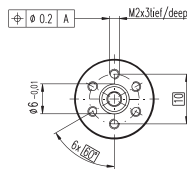
Part Numbers

4.4 : 1	138333		455 : 1	138343
5.4 : 1	138334		561 : 1	138344
19 : 1	138335		690 : 1	138345
24 : 1	138336		850 : 1	138346
29 : 1	138337		1621 : 1	138347
84 : 1	138338		1996 : 1	138348
104 : 1	138339		2458 : 1	138349
128 : 1	138340		3027 : 1	138350
157 : 1	138341		3728 : 1	138351
370 : 1	138342		4592 : 1	138352

Technical Data

Planetary Gearhead	straight teeth
Output shaft	stainless steel, hardened
Bearing at output	preloaded ball bearings
Radial play, 6 mm from flange	max. 0.08 mm
Axial play at axial load < 4 N	0 mm
> 4 N	max. 0.05 mm
Max. permissible axial load	8 N
Max. permissible force for press fits	25 N
Sense of rotation, drive to output	=
Recommended input speed	< 8000 rpm
Recommended temperature range	-15…+100°C
Extended range as option	-40…+100°C
Number of stages	1 2 3 4 5
Max. radial load, 6 mm from flange	10 N 15 N 20 N 20 N 20 N
Gearhead values according to sleeve bearing version	

Figure A.6: Maxon GP 16A Gearhead Datasheet

B COST ESTIMATIONS

The following tables show the costs taken into consideration when estimating the direct manufacturing cost of the Touch Hand II. These included the materials, labour, and electricity. All values here are shown in the Rand currency except for the summary of Table B.4, which includes US Dollars.

Table B.1: Materials Costs

Item Name	Cost per item/m	No. of items	Cost
Mechanical			
ABS plastic	R 250,00	1	R 250,00
M3 threaded rod	R 10,00	1	R 10,00
Brass rod	R 19,20	1	R 19,20
Cable	R 1,00	5	R 5,00
M3 Copper Washers	R 0,67	30	R 20,10
Super Glue	R 50,00	1	R 50,00
M3x3 Grub Screws	R 1,00	6	R 6,00
M2 nuts	R 0,15	15	R 2,25
M2x12 cheese head screw	R 0,50	2	R 1,00
M2x5 cheese head screw	R 0,21	12	R 2,52
M2x8 cheese head screw	R 0,71	1	R 0,71
		mechanical total	R 366,78
Electronic			
Motors	R 965,50	6	R 5 793,00
CAP_ELECTROLIT, 100nF	R 0,30	1	R 0,30
DC Jack, K37212	R 1,50	1	R 1,50
CAP_ELECTROLIT, 10µF	R 0,70	1	R 0,70
Switch (Power), B143	R 1,00	1	R 1,00
Regulators, MC7805	R 4,00	1	R 4,00
Diode 1n4001	R 0,20	1	R 0,20
ZENER, 1N5226B	R 0,35	12	R 4,20
RESISTOR, 33kΩ	R 0,20	15	R 3,00
RESISTOR, 10kΩ	R 0,20	1	R 0,20
RESISTOR, 20kΩ	R 0,25	6	R 1,50
CAPACITOR M/L, 22nF	R 0,35	7	R 2,45
RESISTOR, 27Ω	R 0,25	12	R 3,00
RESISTOR, 6.8kΩ	R 0,25	19	R 4,75
Op-amp, LM358(UTC)	R 1,00	7	R 7,00
CAPACITOR, 680pF 10%	R 0,20	6	R 1,20
CAP_ELECTROLIT, 47µF	R 1,00	6	R 6,00
Drivers, A4973SLB	R 29,38	6	R 176,28
Headers, 2500-02RT	R 0,18	7	R 1,26
RESISTOR, 0.1Ω 5%	R 1,00	6	R 6,00
RESISTOR, 220Ω 5%	R 0,20	3	R 0,60
CAPACITOR, 47nF	R 0,35	12	R 4,20
RESISTOR, 220Ω 5%	R 0,25	3	R 0,75
Teensy, Teensy 3.1	R 425,00	1	R 425,00
PCB board material	R 20,00	1	R 20,00
Header SIL R/A 40W	R 5,10	1	R 5,10
Header SIL STR 40 W	R 4,00	1	R 4,00
Wick Desolder 1.9 mm	R 33,00	1	R 33,00
Twin Flex Black/Black (Power Cable)	R 3,95	1	R 3,95
Hous Sil F/Lock 2W (Motor Plug Housing)	R 0,10	7	R 0,70
Terminals 2510 T Loose	R 0,20	25	R 5,00
Socket DC In-line R/A (Power Cable Attached Socket)	R 4,50	1	R 4,50
Wire M/S 0.34 O=1.6 BLUE	R 2,50	2	R 5,00
Wire M/S 0.2 O=1.6 ORANGE	R 1,35	2	R 2,70
Sleeve heat-shrink 1.5mm BK	R 2,50	1	R 2,50
Solder	R 30,00	1	R 30,00
		electronics subtotal	R 6 564,54
		electronics tax	R 919,04
		electronics total	R 7 483,58
		Materials Total	R 7 850,36

Table B.2: Labour Costs

LABOUR			Time/item [hrs/item]	# items	Time [hrs]	Cost/hour	Cost/item	Total
Mechanical								
3d printing								
	Fingers							
		setup	0,17					
		material removal	1,67					
		filing	1,75					
		total	3,58	4,00	14,33	R 100,00	R 358,33	R 1 433,33
	Palm							
		setup	0,17					
		material removal	1,00					
		filing	1,00					
		total	2,17	1,00	2,17	R 100,00	R 216,67	R 216,67
	Thumb							
		setup	0,17					
		material removal	0,50					
		filing	0,25					
		total	0,92	1,00	0,92	R 100,00	R 91,67	R 91,67
Joint rods			0,08	16,00	1,33	R 100,00	R 8,33	R 133,33
Bushes			0,17	33,00	5,50	R 250,00	R 41,67	R 1 375,00
Assembly								
	finger							
		Cable feeding	0,50					
		Cable Tying	0,50					
		Bushes, washers, rods	0,33					
		total	1,33	4,00	5,33	R 100,00	R 133,33	R 533,33
	thumb							
		Cable feeding	0,67					
		Cable Tying	0,50					
		Bushes, washers, rods	0,50					
		Motor placement	0,17					
		Pulley Placement	0,13					
		total	1,97	4,00	7,87	R 100,00	R 196,67	R 786,67
	palm							
		Cable feeding	0,75					
		Cable Tying	0,50					
		Bushes, washers, rods	0,50					
		Motor placement	0,42					
		Pulley Placement	0,50					
		total	2,67	4,00	10,67	R 100,00	R 266,67	R 1 066,67
							Mechanical Total	**R 5 636,67**
Electronics								
PCB manufacture								R 200,00
Circuit								
	Teensy 3.1		1,00	1	1,00	R 100,00	R 100,00	R 100,00
	Current Sensing		0,75	6	4,50	R 100,00	R 75,00	R 450,00
	Back-emf Sensing		0,75	6	4,50	R 100,00	R 75,00	R 450,00
	Motor Driver		0,75	6	4,50	R 100,00	R 75,00	R 450,00
	Power Circuit		0,75	1	0,75	R 100,00	R 75,00	R 75,00
Wiring								
	Motor plugs and wires		0,17	6	1,00	R 100,00	R 16,67	R 100,00
	Power cable and battery		0,33	1	0,33	R 100,00	R 33,33	R 33,33
							Electronics Total	**R 1 858,33**
							Labour Total	**R 7 495,00**

Table B.3: Electricity Costs

Electricity			Time/Item [hrs/item]	# items	Time Used [hrs]	Power [W]	kWh Used	Electricity Cost [c/kWh]	Cost
PC			16	1	16	500	8	131,46	R 10,52
3d printer									
	finger								
		proximal phalangeal	3						
		middle phalangeal	2						
		distal phalangeal	1						
		total	6	4	24	220	5,28	131,46	R 6,94
	thumb								
		proximal phalangeal	2						
		middle phalangeal	5						
		total	7	1	7	220	1,54	131,46	R 2,02
	palm								
		bottom	13						
		top	8						
		total	21	1	21	220	4,62	131,46	R 6,07
								total	R 25,56

Table B.4: Summary of Costs

| Manufacturing Costs		
Materials	R 7 850,36	$ 635,14
Labour	R 7 495,00	$ 606,39
Electricity	R 25,56	$ 2,07
Total	R 15 370,91	$ 1 243,60

C   ELECTRONIC SCHEMATICS
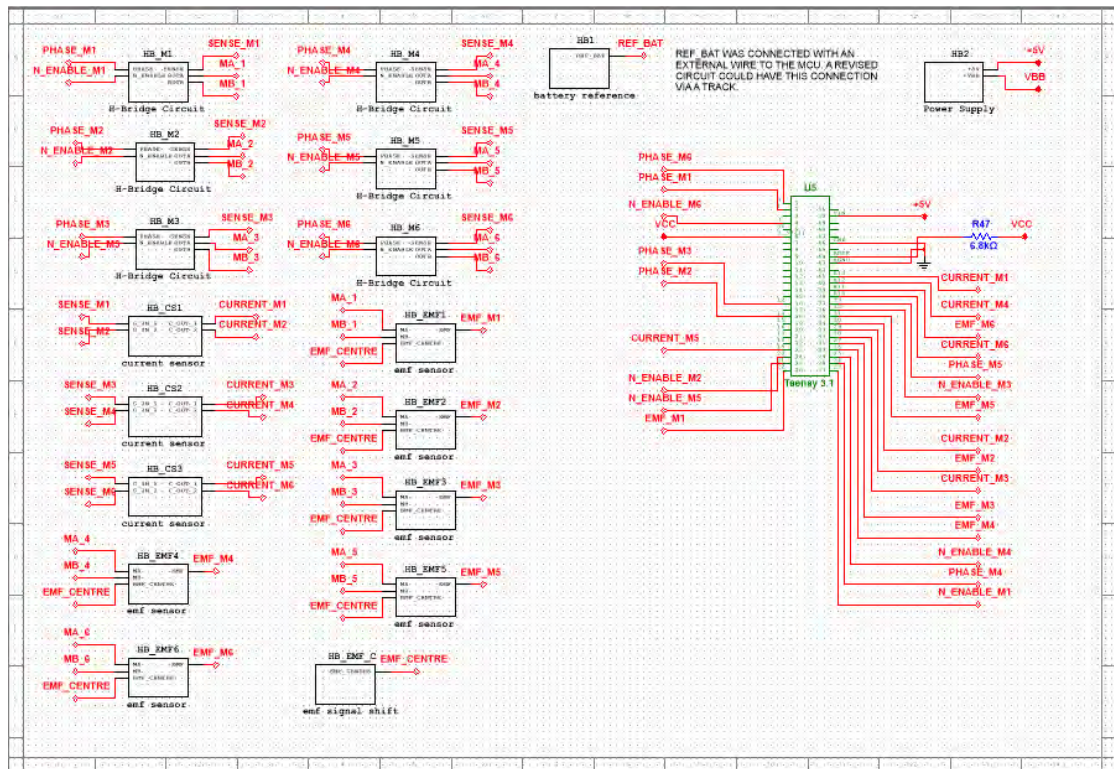
Figure C.1: Symbolic Circuit Diagram with Hierarchical Blocks